Master's thesis

NTNU
Norwegian University of Science and Technology
Faculty of Natural Sciences
Department of Physics

Edevard Brekke Hvide

Effects of Nanostructured SU-8 Surfaces on Neurons and Neural Networks in Vitro

Master's thesis in Nanotechnology
Supervisor: Prof. Pawel Sikorski
Co-supervisor: PhD(c) Nicolai Winter-Hjelm
June 2021

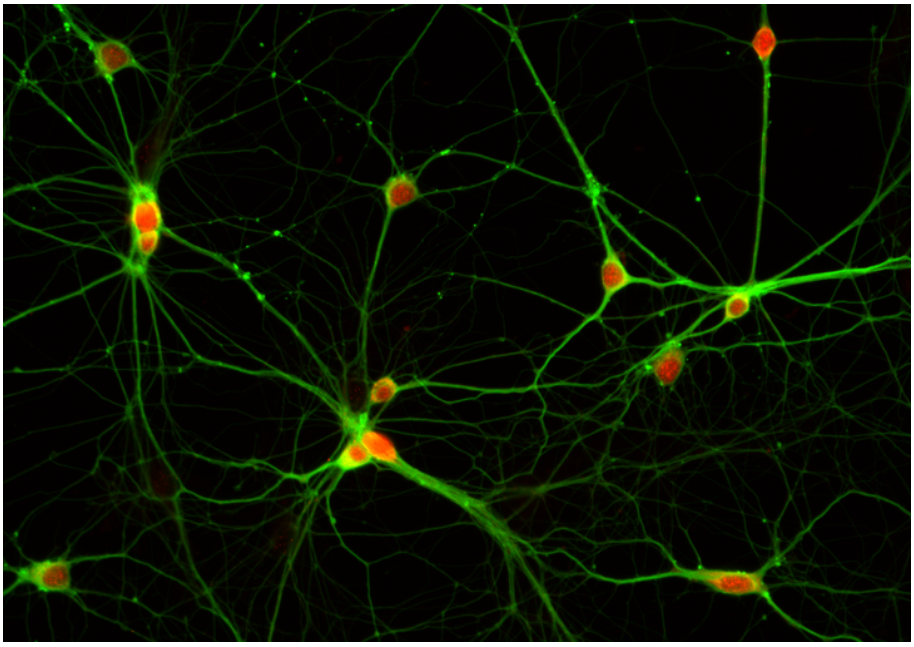

NTNU
Norwegian University of
Science and Technology

Edevard Brekke Hvide

Effects of Nanostructured SU-8 Surfaces on Neurons and Neural Networks in Vitro

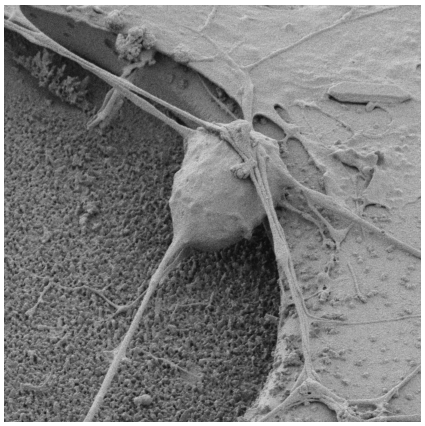

Master's thesis in Nanotechnology
Supervisor: Prof. Pawel Sikorski
Co-supervisor: PhD(c) Nicolai Winter-Hjelm
June 2021

Norwegian University of Science and Technology
Faculty of Natural Sciences
Department of Physics

NTNU
Kunnskap for en bedre verden

Preface

This Master's thesis is submitted in partial fulfilment of the requirements for the degree *Master of Science in Nanotechnology* at the Norwegian University of Science and Technology (NTNU). The work presented was conducted during the spring of 2021 at the department of physics, as part of the *TFY4905 - Nanotechnology, Master's Project*. Experimental work was carried out in the cleanroom of NTNU NanoLab and cell laboratory at the department of Neuromedicine and Movement Science. Unless otherwise stated, all figures are made by the author. Minor parts of the Theory and Materials and Techniques section in this thesis are adapted from the author's Specialization project, which was carried out fall 2020.

Acknowledgements

I would like to extend a big thank you to supervisor Prof. Pawel Sikorski, for giving me the opportunity to conduct this project in his department, and also for the helpful guidance throughout. I would also like to thank Yanna and Axel Sandvig for opportunity to conduct my experiments at the Institute of Neuromedicine and Movement Science. Furthermore, a huge thank you is due to my co-supervisor, Nicolai Winter-Hjelm. Your help has been immensely appreciated. I also hugely appreciate the help from those that gave me training for the various instruments and laboratory work. Thank you to Jakob Vinje, Nicholas Christiansen and Lars Schiro, for great help in your respective expertise areas. I always thought these acknowledgement sections were very pretentious and superfluous, but I now realize that these kinds of projects depend so much on the 'experts' willingness to give a helping hand, and for that, a genuine acknowledgement is due.

Abstract

Nanotopographical growth surfaces have in recent years emerged as a promising strategy to increase topological complexity of biological neural networks cultured on in vitro research platforms. Such platforms can be used for more realistic study of neural network communication and computation, and can aid the development of strategies to improve the therapeutic efficacy in treating central nervous system (CNS) disease and injury. However, little is currently known about the effects of nanotopography on cell viability, morphology, and neural network features. In this work, the effect of nanostructured SU-8 growth surfaces on neuronal cells and neural network features was investigated. A nanostructured SU-8 growth surface was hypothesised to provide a quasi-biomimetic nanoenvironment, and thus promote more relevant behaviours than in traditional planar surface in vitro models.

An array of surfaces with varying surface roughness, from 0-150 nm, were cultured with neuronal cells, in order to screen for the optimal nanotopography with regards to cell viability. To investigate the neuron and neural network behaviour, analysis were conducted employing phase contrast microscope, immunocytochemistry (ICC), scanning electron microscopy (SEM) and a neural network in silico model, on surfaces with roughness from 0-6.8 nm.

It was found that there was an upper limit to roughness, with regards to cell viability, of $S_a = 6.8$ nm. For S_a below 6.8 nm, cell viability was insignificantly different compared to planar controls. It was furthermore found that nanostructured SU-8 growth surfaces may promote more tridmensional soma morphologies, as observed from shape analysis from SEM images, thought to be due to an increase in potential adhesion sites for the cell. The total neurite area per neuron was found to be positively correlated with increased surface roughness, from 0-6.8 nm, analysed by ICC. This was speculated to be due to nanoscale features providing stronger anchorage points for filopodia, affecting growth cone dynamics. However, this did not translate into changes in network topology, as measured by an in silico network simulation model. This was thought to be due to surfaces

with S_a = 1.3-6.8 nm not providing sufficient surface roughness to promote substantial changes in neural migration dynamics. Ultimately, SU-8 nanotopography was implemented into a dual chamber microfluidic chip, coupled with microelectrode arrays, and extracellular recording of a cell culture was conducted. From this, it was found that nanostructured SU-8 growth surfaces may enhance network communication efficiency, detected as more localized network bursts in electrophysiological recordings. This was speculated to be due to the differential behaviours found in cell morphology and neurite outgrowth, acting together to contribute to the increased communication network efficiency, more pertinent to network dynamics seen in the brain.

This research indicates that nanostructured SU-8 provides a viable growth surface, and has the capacity to influence neuron behaviour on several scales. The novelty of implementing nanostructured SU-8 growth in microfluidic platforms, integrated with microelectrode arrays, allows for continual monitoring of the cultures with common light microscopy, combined with the possibility of advanced electrophysiology recordings. Further work still remains to be done in order to fully utilize the opportunities of the current platform, and further directions have been proposed

Sammendrag

Nanotopografiske vekstflater har de siste årene blitt anvendt som en lovende strategi for å øke topologisk kompleksitet av biologiske nevrale nettverk dyrket på in vitro forskningsplattformer. Slike plattformer kan brukes til mer realistiske studier av nevrale nettverk, både i fungerende og syke hjerner, og kan hjelpe å utvikle strategier for å forbedre den terapeutiske effekten ved behandling av hjernesykdom. Imidlertid er lite kjent om effekten av nanotopografi på cellelevedyktighet, morfologi og nevrale nettverksfunksjoner. I dette arbeidet ble effekten av nanostrukturerte SU-8 vekstflater på nevronale celler og nevrale nettverksfunksjoner undersøkt. Den underliggende hypotesen var at nanostrukturert SU-8 ville virke som et kvasi-biomimetisk nanomiljø, som etterligner strukturer som er viktige for nevral celleatferd in vivo. Dette var så tenkt at ville fremme mer relevant celleatferd enn i tradisjonelle flate in vitro-modeller.

En rekke overflater med varierende overflateruhet, fra 0-150 nm, ble dyrket med nevrale celler for å undersøke optimal nanotopografi med hensyn til cellelevedyktighet. For å undersøke nevroncellenes og de nevrale nettverkenes adferd, ble det gjort analyse ved bruk av fasekontrastmikroskop, immuncytokjemi (ICC), skanningelektronmikroskopi (SEM) og en i siliko-modell, på overflater med grovhet fra 0-6.8 nm.

Resultatene viste at det er en øvre grense for ruhet, med hensyn til celleviabilitet, på $S_a = 6.8$ nm. For S_a under 6.8 nm var cellelevedyktigheten ikke påvirket i betydelig grad sammenlignet med flate kontroller. Det ble videre funnet at nanostrukturerte SU-8 vekstflater kan fremme mer tredimensjonale soma-morfologier, funnet ved formanalyse fra SEM-bilder, antatt å være på grunn av en økning i potensielle adhesjonssteder for cellen. Den totale nevrittarealet per nevron ble funnet til å være korrelert positivt med økt overflateruhet, fra 0-6,8 nm, analysert av ICC. Dette oversatte seg imidlertid ikke til endringer i nettverkstopologi, målt ved en in silico nettverkssimuleringsmodell. Dette ble antatt å skyldes at overflatene ($S_a = 1.3$-6.8 nm) ikke ga tilstrekkelig overflateruhet til å fremme vesentlige endringer i nevral migrasjonsdynamikk. Til slutt ble SU-8 nanotopografi implementert i en mikrofluidbrikke med to kammer, kombinert med

MEA, og det ble gjennomført ekstracellulær opptak av nevrale nettverk. Fra dette ble det funnet at nanostrukturerte SU-8 vekstflater med $S_a = 4.7$ nm kan forbedre nettverkseffektiviteten. Dette var begrunnet av funnet at nanostrukturerte overflater induserte mer lokaliserte nettverk-*bursts* i de elektrofysiologiske opptakene.

Dette arbeidet indikerer at nanostrukturert SU-8 kan gi en levedyktig vekstflate, og har kapasitet til å påvirke nevronal atferd på flere skalaer. Den nyskapende kombinasjonen av å implementere nanostrukturert SU-8 vekstflater i mikrofluidplattformer, integrert med mikroelektroder, gir mulighet for kontinuerlig overvåking av kulturene med vanlig lysmikroskopi, kombinert med muligheten for avanserte elektrofysiologiske opptak. Ytterligere arbeid gjenstår for å utnytte mulighetene til forskningsplatformen brukt i dette arbeidet fullt ut. Anbefalinger for videre arbeid ble gitt på slutten av oppgaven.

Contents

Figures

Tables

Chapter 1

Introduction

The nervous system is perhaps the most complex machinery known to man. However, with this immense complexity, comes a risk of damage and severe malfunctions. This is further exacerbated by the central nervous system's (CNS) limited ability to self-repair after damage, leading to injuries often causing detrimental permanent functional deficits and disability. A recent analysis reports that 16,5% of deaths in the world are due to neurological disorders, and is the leading cause of years lived with disability [1]. Furthermore, traumatic brain injuries and spinal cord injuries affect millions across the world each year. Often not treatable, this leaves victims with a grave prognosis [2].

Great efforts have been directed in order to elucidate the inner workings of the CNS, and how and why it malfunctions. For decades in neuroscience research, the golden standard has been conductance of experiments with animals. Although many of these animals offer disease manifestations and phenotypes similar to those in humans, recent studies suggest that the underlying molecular mechanisms, and thus also more large-scale mechanisms, can differ greatly from humans. This is becoming evident in an increasing number of animal models, and has been hypothesised to be the reason why many drugs fail to show efficacy when advanced from in vivo animal studies to human clinical trials [3]. In vitro model systems have therefore emerged as a complimentary approach in recent years, enabling high experimental control, high throughput and less ethical complications. However, traditional in vitro growth surfaces provide neurons with a planar and uniform microenvironment, which starkly contrasts the complex tridimensional topography of the brain, and fails to recapitulate relevant neuronal behaviours seen in the brain [4].

1.1 Problem and Significance of Study

These shortcomings have sparked efforts directed at developing more advanced in vitro models to study the CNS. A myriad of approaches have been investigated in attempts to develop a platform for better recapitulating of the brain, however, the verdict is still out for what the optimal strategy for increasing complexity and at the same time increasing pertinence and keeping experimental control is. Nanotopographical surfaces has in recent years emerged as a strategy that provides neuronal cells with a quasi biomimetic environment that attempts to more closely mimic what neurons experience in in vivo conditions. However, there is still much uncertainty around the effect of nanostructured surfaces on the behaviour of neuronal cells, with regards to basic features such as cell viability, morphology and neural network properties.

The lack of attention is of significance because further advancements in the understanding of nanostructured surfaces may allow better models of the CNS in vitro to be made, obtaining more relevant preclinical in vitro models. This can be used for more realistic study of neural network communication and computation, in both functioning and malfunctioning CNS, and can aid the development of strategies to improve the therapeutic efficacy in treating CNS disease and injury.

1.2 Aim and Objectives of Study

In this research, the effects of a nanostructured SU-8 epoxy growth surfaces on neurons and neural networks was investigated. The underlying hypothesis was that such surfaces would act as a quasi-biomimetic environment, providing nanostructures that promote cell behaviour more closely mimicking that of neuronal cells behaviour in vivo, compared to planar controls. To study this, four research questions were formulated:

- Can nanostructured SU-8 growth surfaces contribute to improved neuronal cell viability?
- How do nanostructured SU-8 growth surfaces influence neuronal morphology?
- Do nanostructured SU-8 growth surfaces affect neural network topology? Can nanostructured SU-8 growth surfaces contribute to increased neural network communication efficiency?

In order to answer these question, corresponding research objectives were formulated:

- Validate and develop preparation protocols for scanning electron microscopy (SEM) and immunocytochemistry (ICC) of neuronal cells. This includes fixation, dehydration and coating protocols. SEM will be applied to study fundamental characteristics of neurons, such as morphology and interactions with the topography surface. ICC will be employed to study the neuronal network, investigating the effect of SU-8 nanotopography on neurite outgrowth and neurite mesh properties.
- Culture cells on a range of nanostructured SU-8 epoxy growth surfaces, from 0 nm to 150 nm, resembling that of the structural components found in vivo, to screen for optimal value of nanotopography with respect to cell viability and cell behaviour.
- Apply computational Waxman model for investigation of neural network topology features as a function of roughness of SU-8 nanostructured growth surface.
- Test SU-8 nanotopography surfaces integrated into two-chamber microfluidic MEA coupled chips, and investigate how nanotopographies influences neural network communication maturation and efficiency, from spiking and network bursts analysis.

The current project is part of an overarching project, with the aim of fabricating and testing of a dual-chamber microfluidic research platform, with integrated microelectrode arrays on nanostructured SU-8 epoxy growth surfaces. Together, this will provide a powerful tool for studying communication and computation in in vitro neural networks. Ultimately, this platform can potentially contribute to further advances within in vitro modelling of CNS function, malfunction and repair, with increased clinical relevance and experimental control.

All fabrication mentioned in this thesis was carried out by fellow MSc student Leik Isdal.

Chapter 2

Theory and Background

This following chapter will establish the essential background for reading this thesis: Firstly an introduction to the relevant fundamentals of neurobiology will be given, followed by a short introduction to neuronal behaviour in vitro. Then, a brief literature review on the previous research conducted in this field will be presented. Lastly, the theoretical framework of the instruments and techniques employed will be presented. This will serve as a basis for understanding the experiments conducted and the data acquired, analysed and discussed in Results.

2.1 An Introduction to Neurobiology

The brain is immensely complex, and since the beginning of humanity, one of the biggest puzzles has been understanding how it functions. Neurobiology can be said to be the field of study that addresses this: seeking to understand how the brain and nervous system functions. Despite being on everyone's mind, it was not before the last century that impacting breakthroughs in understanding it were made. In the initial era of modern neuroscience, breakthroughs were dependent on studying CNS function after it had been detrimentally and locally impaired by exterior forces [5]. Today, neuroscience has evolved to be a tremendously multi-faceted study, combining knowledge from widely distinct disciplines such as molecular biology, material sciences, mathematics, biophysics and computer science. The current project is a very exciting example of how these disciplines can been orchestrated to give rise to cutting edge research. The vast interdisciplinary nature of this project project makes it a challenge to narrow

the scope of the background theory to the fine balance between under-explaining and over-explaining. Thus, in order to keep the text relevant to the research questions posed, an overarching point of focus will be how neurons sense and interact with its surrounding environment in vivo, as this is important to understand the phenomena which was sought out to mimic in this study.

2.1.1 The Nervous System

The nervous system is the machinery that permits living organisms to sense, process and act on its surroundings, and together this gives rise to the feeling of consciousness. The nervous system consists of two main parts: The central- and peripheral nervous system. The central nervous system (CNS) consists of the brain and spinal cord, and is connected to the body via the peripheral nervous system (PNS). The basic unit of the nervous system is the nerve cell, or neuron, and about 100 billion of these assemble to construct the human brain. Neurons come in a myriad of different shapes and forms, and interacts with other neuronal cells such as glial cells, which are vital for healthy function.

To structure the following discussion of the nervous system, a bottom up approach will be employed. The characteristics of the nerve cells are first presented, before the mechanisms by which neurons produce signals, interact with its surroundings and migrates, communicate and come together to create the complex network that is the nervous system is introduced. The text in following subsection is mainly adapted from Purves et al. (2001) [6].

The Nerve Cell

In vertebrates, the first neural cells appear as neural stem cells (NSC), early in the embryonic development. The characteristics of the nerve cell appears when differentiation is initiated. This process evolves the specialization attributes that distinguishes them from the rest of the cells in the body: the ability to communicate via both electrical and chemical signalling. The most important aspect of this is the protrusion of neurites from the cell body. These neurites further develop into the characteristic axons and dendrites, which serve to interconnect individual neurons [6]. A simplistic illustration of a typical neuron is illustrated in Figure 2.1. Dendrites can be

said to be the input structures, receiving signals transmitted from neighboring cells via synapses. Dendrites normally only grow to be a few micrometers long, but branch out to produce intricate branching patterns, at its most complex resembling a fully grown tree. Axons, on the other hand, are the output structure of nerve cells, and can extend to as far as a meter in length, conducting signals from the cell body along the axon length and to a neighbouring cell's dendrite [6]. As a mechanism to increase signalling transduction efficiency, the axon is insulated with evenly interspersed myelin sheaths of oligodendrocytes, with periodic gaps called the Nodes of Ranvier.

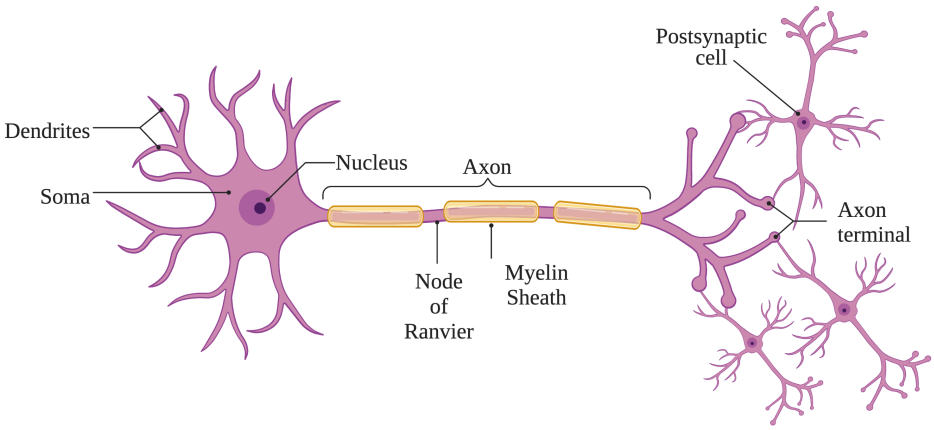

Figure 2.1: Illustration of the typical neuron anatomy showing cell body with its characteristic protruding dendrites and axon. The dendrites have dendritic branches, and the axon branches out where the ends are the axon terminals where synapses connect with other neurons. The axon is insulated with evenly interspersed myelin sheaths of oligodendrocytes, interrupted by Nodes of Ranvier for higher signalling transduction efficiency. Illustration is not to scale.

Neural Signaling

The quintessential property of neurons is their ability to generate and transmit electrical signals. This section gives a rather extensive introduction to the theory explaining this phenomena, as it is deemed important in order to appreciate the fundamentals of how the nervous system works. An introduction of this is furthermore important for understanding the results

acquired from electrophysiological recordings of the neural networks cultured in this project.

The ability to generate and transmit electrical signals is largely due to the cell membrane's selective permeability to different ions, and the non-uniform distribution of these ions across the membrane. The lipid bilayer of the membrane is in itself practically impermeable to ions. The selective permeability however, is due to the presence of ion channels, which are integral membrane proteins with a pore through which ions can cross the membrane. The non-uniform distribution of ions is caused by active ion transporters called ion pumps, which use cellular energy (ATP) to pump ions against their concentration gradient. The most pertinent ion pump is the sodium-potassium pump, which transports three Na^+ ions out of the cell and two K^+ in, resulting in around 20 times more K^+ inside than outside the cell [7]. A schematic illustrating the working mechanism of the sodium potassium pump is shown in Figure 2.2. Respective pumps and channels targeting the other ions present the cell, calcium (Ca^{2+}), and chloride (Cl^-), are also present.

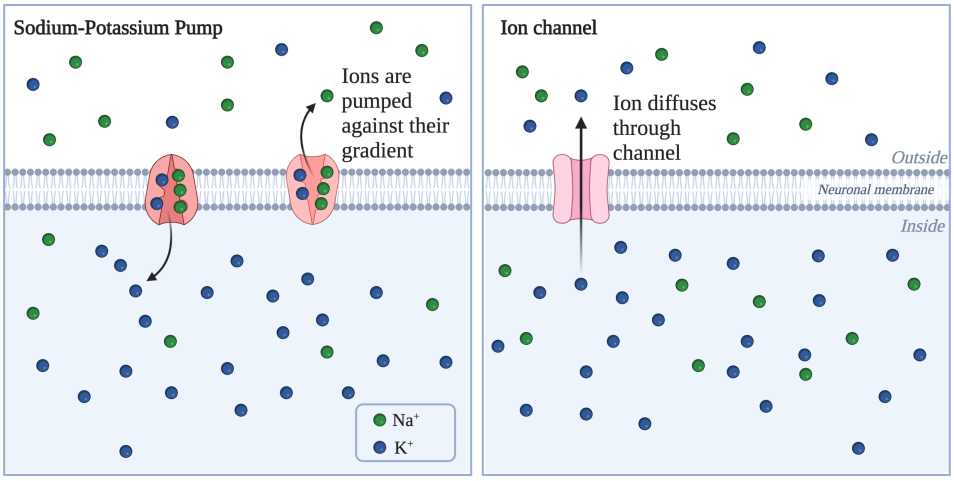

Figure 2.2: Illustration of potassium-sodium ion pump is shown on the left. It uses ATP to pump three Na^+ and two K^+ against their concentration gradient across the cell membrane. On the right, ion channels selectively permit ions to diffuse through the membrane.

With the abovementioned organization, there are essentially two processes that drive the movement of the ions during the resting membrane potential: diffusion and electric potential. Diffusion arises from the statistical tendency of particles to redistribute down their concentration gradient i.e.

entropy, effectively driving K^+ out of the cell (the same happens to the other ions, but are of less impact than K^+ due to their relative smaller concentration). An illustration of this mechanism is shown on the right in Figure 2.2. The accumulation of K^+ extracellularly generates an electrical potential across the membrane that tends to impede further flow of K^+. The ions move across the membrane until the two forces exactly counteract, the potential at this point is called the equilibrium potential.

In the neuron's baseline state, the membrane is more permeable to K^+ than to any of the other ions present, and there is more intracellular K^+ than extracellular. Together this produces a voltage difference, called the resting state [8]. In this state, the neuron is receptive to respond to stimuli. The stimuli can have a number of different sources, and if the stimuli increases the membrane potential (depolarized) to a certain threshold value of approximately -55 mV, it will induce an electrical signals that propagates along the length of axons in the form of an action potential (AP) – the fundamental signal of the nervous system (see Figure 2.3).

The AP is a spike in potential, and its amplitude is not dependent on the magnitude of the stimuli used to evoke it. If depolarization reaches the threshold potential of -55 mV , voltage-gated sodium ion channels are induced to change their geometric configuration which drastically increase its permeability of sodium, resulting in a large influx of sodium ions and a further depolarization of the cell [9]. This is quickly followed by a membrane re-polarization due to a rapid sodium channel inactivation as potassium channels are activated, resulting in a large efflux of potassium ions, driving the potential in the negative direction. If the potential gradient is sufficiently strong, local depolarization may provoke the same reaction in the adjacent section of the membrane, and thus the AP propagates down the axon. An important detail is that the potential after the re-polarization phase overshoots the resting potential, into a state of hyper-polarization. This leaves the ion channels in a passivized state, having the effect of avoiding back-propagation of the signal and thus ensuring unidirectional propagation. The action potential ends when the phase of enhanced potassium permeability subsides, and the membrane potential returns to its normal resting level [10].

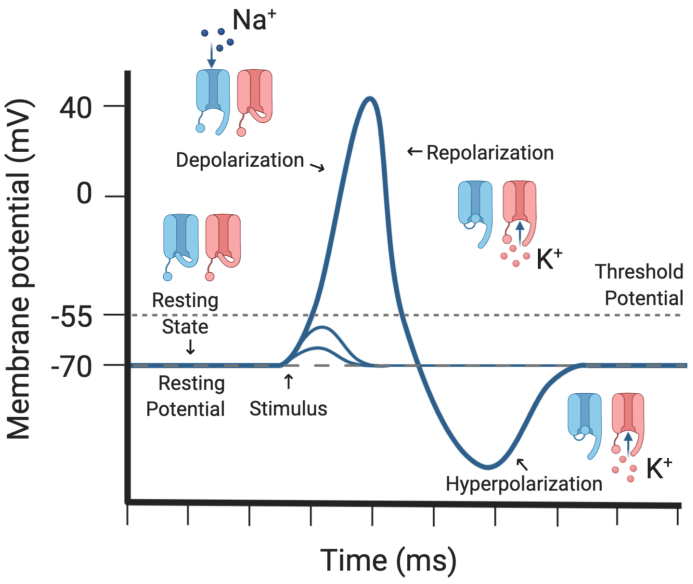

Figure 2.3: Illustration showing the three distinct phases of an action potential. Firstly, if the stimuli causes depolarization above the threshold potential, an AP is initiated with the opening of voltage-gated sodium channels, illustrated by the blue channels. If however the stimulus does not depolarize the cell membrane sufficiently enough to reach the threshold potential, sodium channels do not open, and without further stimuli the membrane potential returns to the resting potential. Sodium channels then alter their configuration to an inactive state and voltage-gated potassium channels are opened, causing out-flux of potassium ions, illustrated with blue ion channels. The membrane potential lastly hyperpolarizes below the resting membrane potential before returning to a resting state.

When an AP reaches the end of an axon (the axon terminal) the signal can be transmitted from one neuron to another, over a minute wide conjunction called a synaptic cleft [6].

Neurons and Their Interactions With The In Vivo Environment

To justify the hypothesis of this study, it is instructive to give a brief introduction to the theory of how neurons interact with their environment in in vivo conditions, and the central structural components present in these interactions. Thus, the next section will a include brief introduction to the theory behind two important processes: neuronal migration and neurite outgrowth, with the focus on how neurons interact with their environment.

Neuronal Migration - Establishing the Architecture

In the process of growing into the complex three dimensional CNS architecture, neurons migrate from their site of origin to their final position, a process called neuronal migration [11]. This translocation is tightly conducted under the influence of the surrounding environment providing a structural scaffold, called the extracellular matrix (ECM). The ECM is composed of a matrix of collagen fibers lined with interspersed proteins and polysaccharides. Collagen forms the matrix structure and the proteins provides interaction sites for interaction with the neuronal cells [12]. These interactions occur through adhesion complexes formed between trans-membrane receptor proteins of the cell membrane, and ligand molecules in the EMC. There is still debate around what exact mechanisms govern neuron migration, however, there is agreement on that it requires the dynamic interaction with the extracellular environment at specific sites, such as focal adhesions, podosomes and point contacts. These serve as physical anchor points that generates traction forces that drive the neuron forward [13]. This anchoring is mediated by transmembrane adhesion receptors cell such as the integrins, that bind to specific ECM ligands, such as laminin [14]. Furthermore, neurons also migrate with the help of other neuronal cells present in the brain. One of the main modes of neuronal migration is called *radial migration* [15]. Radial migration is the primary mechanism by which developing neurons reach their final position, where they travel intimately apposed to elongated vertical shafts of radial cells, acting as a substrate for guiding the direction and behaviour of the neurons. Depicted in Figure 2.6 are neurons migrating along radial glial cells. The elongated shafts of the radial glial cells can be seen to be studded with short thorn-like protrusions called lamellar expansions, which are thought to play an important role in providing attachment structures that promotes the migration [16, 17].

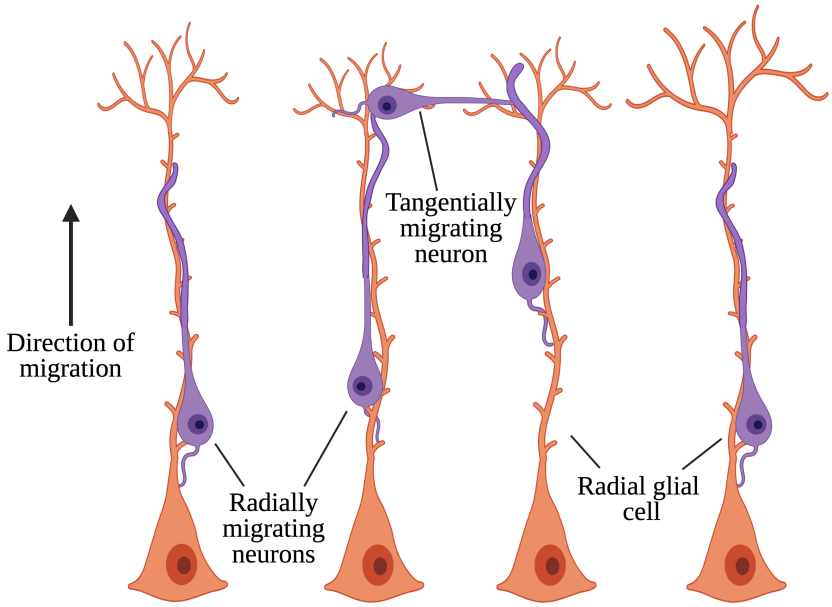

Figure 2.4: Simplified schematic of neurons migrating both radially and tangentially on the scaffold provided by radial glial cells. Neurons can be seen to be intimately apposed to the elongated vertical shafts of radial glial cells, and use these as a physical scaffold surface in its translocation. The neurons can form adhesion points on the short right angle protrusions called lamellar expansions, which facilitate the migration.

The Growth Cone - Connecting the Brain

Up until now, the neuron as the fundamental unit of the brain has been introduced, but what truly gives rise to the complexity of the brain are not neurons by themselves, but rather their organization into intricate anatomical networks, called *neural networks*. The correct wiring of the nervous system is dependent on the razor sharp ability of dendrites and axons to locate and recognize their appropriate complementary synaptic partners. This process is orchestrated within the specialized tip of the growing axon, called the *growth cone*, illustrated in Figure 2.5. At the edges of the growth cone are an array of protruding integrin-containing projections called *filopodia*, which act as sensing probes exploring the environment. As shown in Figure 2.5, the filopodia interacts with the environment through both physical and chemical cues [18]. Upon contact with a physical structure in the ECM, the actin in the filipodia can adhere to ECM surface ligand proteins, mediated by integrin, forming a mechanical link, called a adhesion

complex [19]. These links can mature into larger mechanical links called *focal adhesions*, which in much the same way as for soma migration, act as anchorage points from which the growth can exert traction forces that cause movement. In upon acting on the abovementioned variety of cues, the growth cone can stop, branch out, retract and change direction and speed by harnessing mechanical force from regulating internal polymerization processes [20].

Research continues to find increasing ways in which the filopodia and growth cone can sense and be influenced by the physical environment. Recent investigations have revealed interactions influenced by physical features such as rigidity and mechanical stiffness of the surface, the aspect ratio and contact angle of the filopodia with surface structures [21].

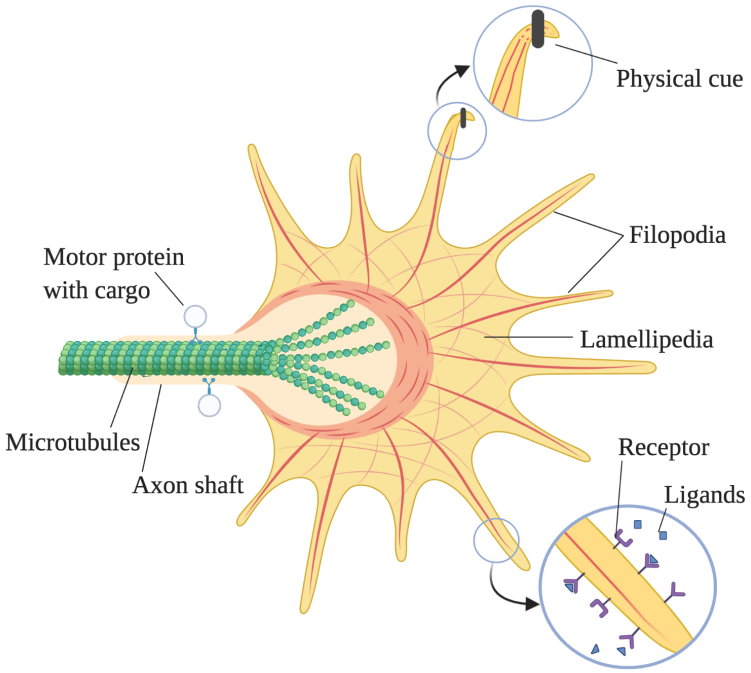

Figure 2.5: Illustration of the growth cone of an axon, here growing from left to right. Filopodia can interact with physical structures and biochemical concentration gradients of ligands present in the microenvironment. In interaction with the physical environment, the actin (red lines) in the filopodia may bind to ECM protein ligands, mediated by integrins, forming an adhesion complex which can mature into a focal adhesion and direct the growth of the axon by selective disassembly of the cytoskeleton.

Relevance To Current Project

The relevance to this project of the abovementioned neuronal interactions with the ECM becomes increasingly evident when noting the scale at which many of the processes take place. The surface substrate provided by radial glial cells protrudes thorn-like structures with a diameter as small as 6-15 nm [22]. Probing filopodia are 60-200 nm in diameter, and have been reported to be able to experience contact guidance from features just 10 nm in height [23]. ECM ligands, such as fibronectin, laminin or collagen fibrils are in the range from tens to hundreds of nanometers [14]. Furthermore, adhesion complexes are on the scale of 5-200 nm, while focal adhesions are between 200 nm and 10 μm [24]. Taking this together, this further motivates the interest of investigating how nanofabricated surfaces in vitro can affect the behaviour of the growth cone and neurite outgrowth, and the subsequent neural networks.

2.1.2 Network Neuroscience

Heretofore, the neurobiology of the nervous system and its constituents have been considered. This will serve as the backdrop for understanding the fundamental cell behaviours observed under the experiments of this thesis, and presented in results section. However, as discussed before, the truly complex functions arise when single cells assemble and interconnect to construct neural networks. To understand and be able to explain this, the theoretical framework of *network neuroscience* will now be introduced.

Network neuroscience is an approach employed to understand the organization and functionality of neural networks, taking advantage of the theoretical framework developed in network science [25]. The cornerstone of network neuroscience is studying neural networks through the lens of *graph theory*. According to graph theory, biological neural networks can be described as graphs that are composed of *nodes*, denoting neural elements, that are linked together by *edges* [26]. Interestingly, this framework can be applied to a wide range of phenomena, meaning that nodes can represent everything from individual neurons to larger clusters or compartments of neurons, depending on the aim of the study, as illustrated in Figure 2.6. Furthermore, edges connecting these nodes may represent either structural or functional connections, at different scales in the brain. An example of structural connections are physical connections in the brain in the form of synapses or axonal projections [27]. Whereas functional connectivity can be said to exist if there is a statistical relationship between the measures of

activity recorded, such as the statistical dependence in the spiking output between two neurons [28].

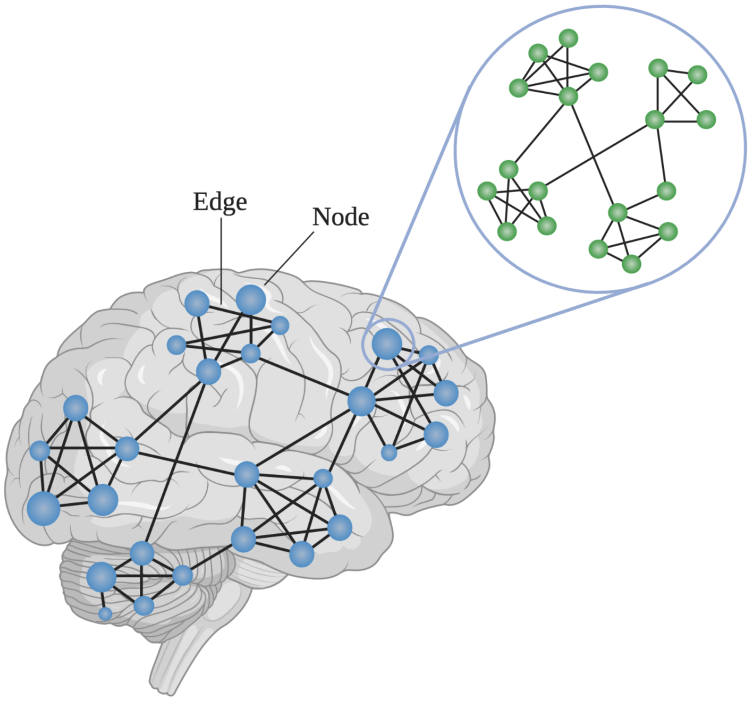

Figure 2.6: Simplified schematic of neural network of the brain, demonstrating how the brain can be represented by graph theory, with the abstract concepts *node* and *edges*. Small world topology is demonstrated by the nodes being organized into distinct clusters connected by short path lengths, and longer-spanning edges linking these clusters together. The nodes represent collections of neurons at different scales of the brain. This is illustrated by the zoom-in on one macro-node, where it is shown that network structures can be considered at lower scales.

When a network is represented by graph theory, there are a number parameters that one can compute to give insights into the properties of the network. Most commonly looked at is average path length and clustering coefficient. The average path length is defined as the average distance between all pairs of nodes in the network, and is associated with the efficiency of information propagation in a network. It is calculated by

$$\langle d \rangle = \frac{1}{N(N-1)} \sum_{i \neq j} d(n_i, n_j) \tag{2.1}$$

Where N is total number of nodes in the network and n_i, n_j are an arbitrary nodes. Furthermore, the clustering coefficient is the probability that two neighbors of a randomly selected node link to each other, and is calculated by

$$\langle C \rangle = \frac{1}{N} \sum_{i=1}^{N} C_i \tag{2.2}$$

where C_i is the local clustering coefficient defined as

$$C_i = \frac{2L_j}{k_i(k_i - 1)} \tag{2.3}$$

where L_i represents the number of links between the k_i neighbors of node i [27].

A range of studies have shown that, when brains are modeled with graph theory, they feature so-called *small-world topologies*, which is characterised by a low average path length and high clustering. Small world is denoted by ω and is defined as

$$\omega = \frac{L_r}{L} - \frac{C}{C_l} \tag{2.4}$$

Where the characteristic path length L and clustering coefficient C are calculated from the network in question, $C_l$is the clustering coefficient for an equivalent lattice network, and Lr is the characteristic path length for an equivalent random network. For a further introduction to this theory, the reader is directed to the original paper by Telesford et al. (2011) introducing the ω small world index [29].

The characteristic features of small world topology in the brain is thought to facilitate its high computational capabilities, low energy consumption, and non deterministic functions, as well as the simultaneous capacity of information integration and segregation; the two emerging network phenomena recognized as the basis of behaviour [30]. Recently, network neuroscience has attracted increasing interest as a promising framework to in-

vestigate perturbations of the brain, where it is looked at from the perspective of disturbed neuronal networks, instead of at the cellular level [31]. As an example, reduced small world topology and altered connectivity in particularly associative areas, have been reported in Alzheimer's Disease [32–35], and small-world topology has been shown to facilitate the spread of disease to a greater extent than other network architectures [36, 37].

There is little doubt that network topology is of paramount importance in in vivo network function. However, there is mounting evidence that the behaviour of neural networks grown on planar surfaces *in vitro*, is largely incompatible with the small world topology found in of the brain. From electrophysiological recordings, neural networks grown in vitro have been found to elicit tendencies of highly synchronous bust activity network-wide, which deviates from the small world topology behaviour [4, 38]. Other research points to an absence of small worlded topology in neural networks grown on standard planar glass chips, analysed through the lens of graph theory [39]. These discrepancies strongly limits the accuracy of in vitro models and highlights the importance of developing more advanced in vitro models that have the capacity of more pertinently recapitulating the complex network features found in the brain.

2.1.3 Neuronal Cell Culturing In Vitro

Neurons are a cell type that are particularly challenging to culture in vitro, as they can be highly sensitive to environmental changes, such as physical stress, alterations in temperature and pH shifts [40]. In order to continually evaluate the health and behaviour of neurons in vitro, it necessary to have an understanding of the fundamental characteristics of different cell processes, viewed through a standard light microscope found in most cell laboratories. In this section, the basic cell behaviours that hallmark healthy cell maturation in in vitro culturing will be presented. This will serve as a theoretical basis for explaining observed behaviours obtained by optical microscope throughout the experiments in this project.

In order to provide a viable in vitro environment for neuronal cell culturing, basic components such as nutrient, temperature and CO2 level must be held as constant as possible. In the same way as adhesion to ECM structures is necessary in in vivo development, attachment it is also a vital requirement for neurons to survive and consequently mature in vitro [41]. As discussed earlier, it is standard protocol to coat the surface with extracellular matrix proteins such as collagen, fibronectin, laminin, to facilit-

ate attachment, before seeding neuronal cells [42]. When neuronal cells are seeded on in vitro surfaces, and sufficient biocompatibility is provided, neuronal cells adhere to the surface within minutes and begin to initiate protrusion of neurites, and the neuron takes on its characteristic polarized shape [43]. Neuronal cells that do not successfully attach to the surface can be recognized by a shrunken morphology and lack of neurite outgrowth [44]. Growing axons, led by the growth cone, explores the local environment, and upon interaction with a neighbouring neuron, may form a synaptic connection. After a few days in vitro (DIV), healthy neuronal cultures can be expected to have established numerous synaptic connections, and a neural network can be seen to form [45]. In the following DIVs, further healthy maturation gives rise to axons bundling together, in what is called *fasciculations*, providing stable and strong connections. Furthermore, fasciculations may interconnect cells that have migrated together to form regions called *clusters*. Tying this in to the network neuroscience introduced in the previous section, both clustering and fasciculation can be indications of efficient networks and small world topology forming [46].

2.2 Literature Review: Topography Surfaces in in vitro Models

An insight into central biological processes has heretofore been presented. The extensiveness of this introduction was deemed necessary in order to establish a basic understanding of the behaviours that are attempted at being recapitulated in in vitro systems. The following section will present a review of previous research related to the current research. It will be structured as a funnel, firstly briefly discussing the wide range of topography surfaces previously developed, and then the focus will be narrowed in on previous research regarding nanotopography, which has been employed in this project. This serve to underscore the contribution of this current project to the existing body of previous research.

As discussed in the introduction, developing in vitro model platforms that more accurately recapitulate in vivo CNS environments can be pivotal for further advancement in medical neuroscience. There is a wide literature on different strategies employed to achieve this. Of these, one can largely divide them into two categories: controlling biochemical properties, and controlling physical properties [47]. The importance of biochemical cues is well investigated and established, playing a role in almost all cellular

behaviours, such as cellular differentiation, cell migration, neurite growth and network dynamics [48–50]. Physical properties, have on the other side been less studied. However, as discussed in Section 2.1.1, there is mounting evidence that the physical parameters of the extracellular milieu plays a crucial role during development of the CNS [48]. Recent years have seen the emergence of in vitro topography surfaces - or 2.5D growth platforms - that aim to recapitulate the physical structures found in vivo, and increase pertinence of research models.

Topography Surfaces

Topography can be described as the arrangement of the spatial and structural features of a surface. Fabricating such surfaces has been made possible by the emergence of nano- and microfabrication technologies in recent years, providing tools capable of controlling structures down to the low nanometer regime.

There have been a myriad of studies investigating the effect of topography on neural cells and their neural networks, including grooved surfaces [51–53], aligned fibers [54–58], pillars [59–62] and nanoroughened surfaces [39, 63, 64]. These have elucidated topographical effects on several neuronal behaviors including neuronal adhesion [24, 64], neurite outgrowth [65, 66] and network formation [39]. Other results indicate that surface topography has an effect on somal migration. Czeisler et al. found in their 2016 paper that neural stem cells showed differential migratory reactions in different topographical contexts, using electrospun polycaproalactone fiber mats [67]. In a similar manner, Seo et al. showed in their recent 2021 paper that migratory behaviors of primary hippocampal neurons on a siliconmicrocone array varied as as a function of the pitch of the microcones, concluding that speed and direction of migration, are correlated with the pitch and shape of underlying structures [68].

Nanotopography Surfaces

If topography can be said to be the arrangement of structural features of a surface, nanotopography can be said to refer to surface features at the nanoscopic scale. Nanostructured, or nanoroughened[1], topography sur-

[1]Note that in this project, nanostructured, nanotopographical and nanoroughened have been used synonymously.

faces are a sub group of anisotropic topography surfaces, meaning that it has the same properties in all directions. The degree of roughness is usually quantified in terms of statistical roughness parameters, such as the arithmetic average, S_a, defined as the mean vertical deviation from an average baseline value [63], which is used in the current study. In general, the higher the S_a value, the rougher the surface is.

Throughout the literature, the behaviour of cells on nanoroughened surfaces has been reported to yield a wide array of neuronal behaviour. Employing nanoroughened silicon surface, Saida Khan et al. and Y. W. Fan et al. found that primary cortical cells responded most optimally to surface roughnesses in the ranges from 20-100 nm and 20-50 nm, respectfully. They also found that cell adherence was negatively affected for surfaces with S_a less than 10 nm, and for rough surfaces with S_a above 70 nm [64, 69]. Cyster et al. found that nanotextured titanium nitride films with S_a values from 1.3-5.6 nm reduced the ability of primary hippocampal neurons to attach and adhere to the surface, relative to Poly-D-lysine (PDL)-coated glass [70]. Furthermore, Onesto et al. demonstrated in their 2017 paper that nanoroughened silicon substrate affects networks topology, directing neuronal migration to assemble into computationally more efficient networks than for planar surfaces, with maximum affect in the low nanometer range (S_a = 22-30 nm) [39].

2.3 Etched SU-8 as Growth Surface

Throughout the literature of nanoroughened surface topography research given above, many different materials have been used, such as silicon [39, 64, 69], gold [24], nanomaterials and nanowires [21, 66] and metals [65]. The common denominator of these materials is that they are biocompatible and allow for a surface modification. However, there are obvious shortcoming of many of these materials. Firstly, their inability to allow continually monitor growth of cells with standard optical microscope, as they are not transparent. Secondly, materials such as gold and silicon are also conductive materials, which is not compatible with integration with MEAs for electrphysiologal recordings. In this project, growth surfaces were based on the epoxy based negative photoresist SU-8. This section will give an introduction to its properties.

SU-8 is an epoxy based near-UV negative photoresist, and has been extensively employed for micro- and nanofabrication in the last decades [71]. SU-

8 exhibits many advantages, such as high biocompatibility, chemical stability, structural integrity, low cost and high fabrication versatility [72]. Furthermore, it is transparent, which allows for the possibility to continually monitor cultured cells with standard optical microscopy. Lastly, it is compatible with integration into microfluidics coupled with microelectrode arrays. To get an understanding of the environment that the cultured neuronal cells experience on such surfaces, a brief introduction of SU-8 and the nanostructuring process used to roughen the surfaces in this project will be presented next.

As for all photoresists (for a more extensive explanation of photolithography, the reader is directed to Isdal's thesis [73]), SU-8 is made up of three base components: polymer resin (Bisphenol A Novolac epoxy), an organic solvent (cyclopentanone) and a photo-acid generator (PAG) (triarylsulfonium hexafluoroantimonate salts). To create planar surfaces, SU-8 is spin coated in a glass substrate to create a micrometer thin film. Upon exposure to UV-light, the photosensitive PAG is activated, producing a strong acid, which catalyses a reaction forming a highly cross-linked network. The nanoroughening of SU-8 is achieved by exposure to partial oxygen plasma, which produces a roughness on a micro-/nanoscale, with roughness increasing with etching [74]. Research on the mechanism behind the roughening effect from partially etched SU-8 is scarce, however is believed to be caused by the antimony present in the PAG, and the generated acid upon photoactivation. Antimony compounds are mechanically rigid enough to resist the plasma exposure, and thus forms thermally stable compounds in reaction with the plasma. Micro-/nanoscale deposits of antimony compounds appearing on the SU-8 surface effectively shield underlying resist from etching, creating protruding surface structures of non-etched SU-8 [75]. The effect of these structures on neuronal cells and neuronal networks is the interest in this research.

2.4 Instruments and Techniques

Throughout the course of this project, several different instruments and techniques were employed, for fabrication, characterization and analysis. In the following subsections, a brief theoretical background of these instruments and techniques is presented. The techniques are presented in the order of which they were employed in the project.

2.4.1 Optical Microscopy

Light optical microscopy is the oldest design of microscope, making its appearance in modern form in the 17th century. It has its advantages of being both easy to use and available for a broad range of applications, but still with many complex designs that aim to improve resolution and sample contrast. Two parameters are important in describing the quality of a microscope: magnification and resolving power. Resolving power is measured by the ability to differentiate two discrete points in an object; the greater the resolving point, the smaller the minimum distance between two points that can be distinguished, and better the clarity and detail of the image.

Figure 2.7 illustrates the path light takes in an optical microscope instrument. Modern microscopes use LED as the source of light. On their path towards the sample of inspection, the light rays focused by the condenser, so they are projected equally. After the light interacts with the sample, it reaches the objective lens. Typically there will be a rotatable turn wheel which lets the user select between degrees of magnification. The objective gathers the light to then magnify and focus it. A second lens called the ocular lens is often included, and further magnifies the light to produce a total magnification of the product between the ocular magnification and objective magnification. Finally, the light reaches the eyepiece and the specimen can be observed.

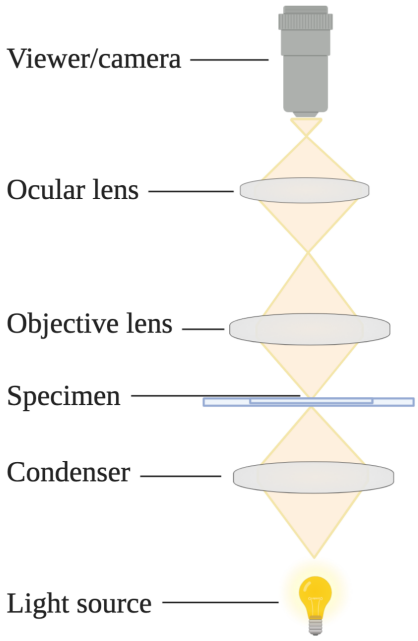

Figure 2.7: Schematic of the path light takes in an optical microscope. The light source here is shown as a lamp, but in modern microscopes it is often LED. The light rays are firstly focused by the condenser onto the specimen. The light interacts with the specimen and then follows to be focused by the objective lens and the ocular lens, before it reaches the observer.

2.4.2 Phase Contrast Microscopy

A further development of the conventional optical microscope is phase contrast microscopy. Phase contrast improves the challenge that is met from the fact that unstained cells absorb nearly no light, which results in extremely small differences in the intensity distribution and thus not a very insightful micrograph. The principle of phase contrast microscopy is essentially to translate minute variations in phase, due to refraction by the sample, into brightness intensities. When light waves pass through a medium interface, interaction with the medium causes the phase of the light wave to shift as a function of the properties of the medium, a phenomenon called refraction. Different media have different refraction indexes, water has 1.33 and a typical value for cell cytosol is 1.360-1.390 [76]. As a result, phase contrast microscope enables continual monitoring of ongoing

cell culturing, and high contrast and sharp clarity micrographs of minute specimen detail can be acquired. Phase contrast microscopy is utilized large parts of this current thesis, which was is permitted by the transparency of the SU-8 nanotopography growth surface, a major advantage of the current approach.

Working Principle

The following explains the working principle of the instrument, see Figure 2.8 for a schematic representation of the fundamental parts of the instrument. Firstly, the light source passes an annular ring, an opaque disk with a thin transparent ring, which produces a hollow cone of light. The light is then focused onto the specimen by a condenser. When the light pass through the specimen, some light rays are refracted due to the aforementioned medium properties, and thus the phase is retarded by about -90°. The light rays then pass a series of lenses, focusing the rays. To distinguish direct light from the refracted, a phase plate is introduced. Refracted rays crosses a thicker section of the plate effectively retarding its phase by -90° compared to the direct light which cross a thinner part. This results in a difference in wavelength of the refracted and direct rays by 180°. Due to the nature of waves, destructive interference between the rays occurs, which creates a phase contrast. The resulting image will then have a bright background, formed by the direct light, while the specimen appears dark and well-defined [77].The above describes the positive phase contrast technique. In its negative form, the direct light is instead phase-shifted by -90°. The refracted and direct light will thus be in phase when they hit the image plane and therefore constructively interfere, resulting in an increase in the brightness compared to regions that do not contain the specimen.

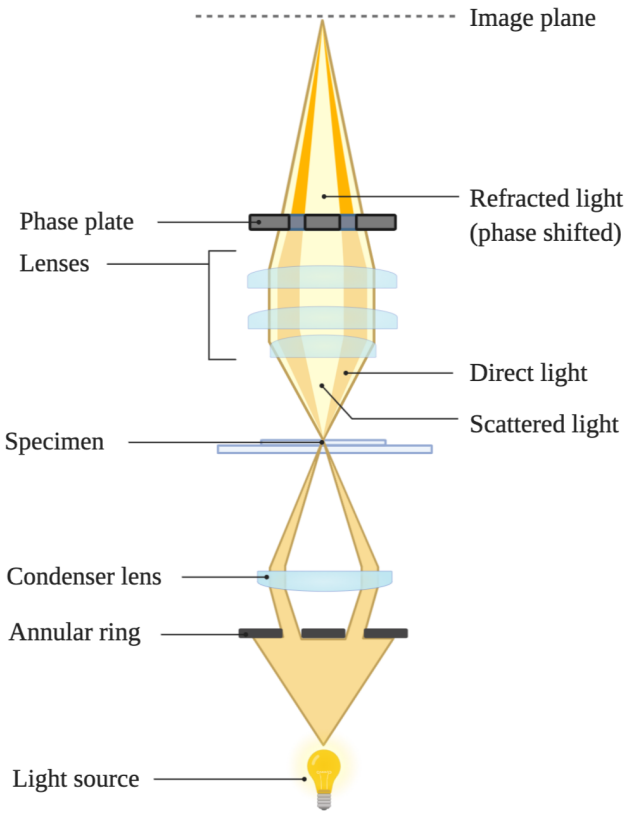

Figure 2.8: Schematic illustration of the path of refracted and direct rays in the dark-phase-contrast microscope. The light rays first pass the annular ring, which produces a hollow cone of light. The light is then focused onto the specimen by a condenser, where some light rays are retarded -90° out of phase. After this, the rays are again focused by a series of lenses. Finally, a phase plate further refracts the refracted light, causing the direct and refracted rays to destructively interfere, giving an image of the specimen where it will be dark against a brighter background.

2.4.3 Epifluorescence Microscopy

Epifluorescence microscopy is one of the most widely used tools in biological research, and uses optical microscopy in combination with the technique of *immunocytochemistry (ICC)*. An explanation of epiflourescence mi-

croscope demands an explanation of ICC. However, to keep the text clear, the principles of the microscope will be explained in this section, and a discussion on the principles of ICC will follow in 2.4.5. Before discussing the principles of an epifluorescent microscope, it is necessary to explain the theory of fluorescent molecules.

Principle of Fluorescent Molecules

The basic working principle of epifluorescent microscope is to stain the specimen in question with antibodies conjugated to a fluorescent reporter tag, which then can be detected by the use of laser systems and optical microscope. Most commonly, a fluorescent reporter tag is a molecule called a *fluorochrome*, and also used in this project. The essential property of such molecules is that when they absorb a photon, and re-emits a photon of a higher wavelength. A molecule or atom is said to become excited when a photon interacts, and transfers, energy to an electron. The energy of the electron will subsequently increase, and by nature of quantum mechanics, the electron will discretely jump to a higher, and more unstable, orbital state. As this state is unstable, the electron will quickly fall to a slightly lower, more stable, relaxed singlet electron state, giving off the energy as heat. Finally, the electron falls back to the ground state. Following the law of conserved energy, the energy difference between the two states will be released as a photon, called emission [78]. The difference in the wavelength of the emission and the excitation photon is named Stokes Shift (this is graphically illustrated in Figure 2.9); it is this phenomena that is exploited in epifluorescent microscopy.

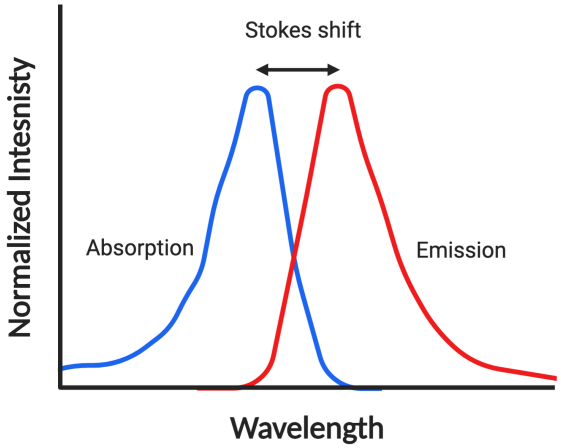

Figure 2.9: Stokes shift is the shift of wavelength between the absorption and emission wavelength for a fluorescent molecule, represented with blue line and red line, respectively. Y-axis is normalized, and is a measure of the proportion of light absorbed.

Principles of Instrument

After the steps of ICC have been conducted, the specimen is placed in the microscope and illuminated with a light of a specific wavelength, corresponding to the reporter tag used. According to the abovementioned theory of Stokes Shift, a light with a longer wavelength will be emitted by the fluorescent molecules. The illumination light is separated from the much weaker emitted fluorescent light through the use of a spectral emission filter (illustrated in Figure 2.10) [79]. A dichroic mirror is used, which is a mirror that has significantly different transmission properties at different wavelengths, effectively permitting the fluorescent light pass through to the detector, but reflecting the illumination light onto the specimen. Lastly, the fluorescent light passes an emission filter, which further selects the specific wavelength which is detected by the detector.

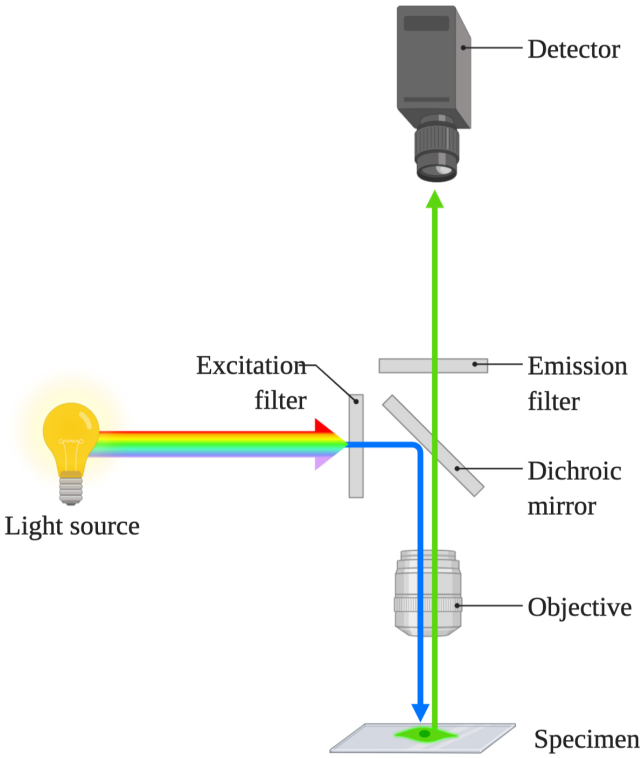

Figure 2.10: Illustration of light path in epifluorescence microscopy. The light first passes the excitation filter, which permits a specific wavelength of light to pass. The light is then redirected towards the specimen. The fluorescent molecules present in the specimen absorb and emit the light according to the theory of Stokes Shift. The emitted fluorescent light then passes through the dichroic mirror and emission filter, further specifying which wavelength reaches the detector.

2.4.4 Scanning Electron Microscopy

In this project, a scanning electron microscope (SEM) was employed to answer the research questions regarding neuron morphology, thus, it is instrumental that the inner workings of this tool is described.

A scanning electron microscope (SEM) is a type of electron microscope that uses a focused beam of electrons to produce an image of a sample. Highly energetic electrons are accelerated towards the sample, which then interact with the atoms in the sample to give various signals that contain in-

formation about the sample. By analysis of these signals, one can produce high resolution images at nanometer scale. An illustration of the fundamental functioning parts is shown in Figure 2.11. To structure this section, it will be divided into three parts: signal production, signal acquisition and preparation of biological samples for SEM.

Signal Production

The electron beam is generated by means of thermionic emission or cold field emission, and then emitted from an electron gun fitted with a tungsten filament cathode. The electrons are accelerated to an energy between 0.5keV and 30keV by electromagnetic condenser lenses in the instrument column, to form a high resolution beam aimed to a spot on the sample of about 0.4 nm to 5 nm, diameter. The strength of the electric field determines the kinetic energy of the electrons hitting the sample, and the depth into the sample the electron penetrates. A low acceleration voltage of the electrons is often chosen when examining surface structures, as this limits the interference from deeper penetrating electrons produced from high acceleration voltages [80]. After the beam is focused, the beam passes though pairs of scanning coils in the final column, which can deflect the beam in both the x and y dimensions, ultimately scanning the sample in a raster fashion [81].

Signal Acquisition

Various types of signals are produced as a product of the interaction between the incoming electron and the specimen, including secondary electrons (SE), characteristic X-rays and light (cathoduluminescence (CL)), reflected or back-scattered electrons (BSE), transmitted electrons and absorbed current (specimen current). In conventional SEM mode, when looking at surface features, it is the secondary electrons that we are interested in. Secondary electrons are ejected from conduction or valence bands of the specimen atoms from the inelastic interactions with the incoming primary electron. Only a small amount of kinetic energy is transferred to secondary electrons because the amount of energy in beam electron is small compared to the electrons of specimen. Because of their low energies, the secondary electron's mean free path is limited in solid matter. Consequently, secondary electrons have the innate quality of being highly localized at the point of interaction with the incoming electron in the top few nanometers of the sample. The electrons that are reflected from the substrate are detected by a scintillator-photomultiplier detector system, which use an electric field to attract the low-energy electrons. The pixel's intensity in the resulting image is directly proportional to the number of secondary electrons detected

per. scanned area.

The acceleration voltage allows electrons to penetrate the sample; thus, the higher the acceleration voltage the more penetration into the sample will occur. As a result, ultrastructural information from deeper layers will interfere with the actual surface morphology that is seen. Therefore, if acceleration voltage is lower, a better quality of the surface molecules and structures can be obtained [80].

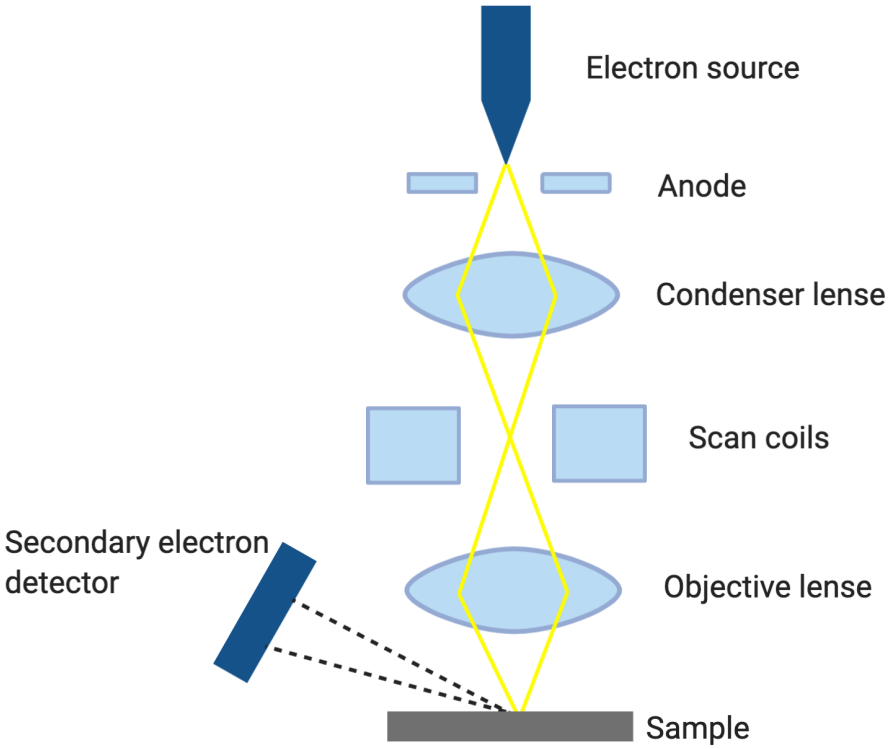

Figure 2.11: Schematic of working principle of SEM instrument in conventional mode detecting secondary electrons for analysis of surface features. Electron beam is shown in yellow line, which is emitted from a filament cathode. The electrons are accelerated by the condenser lens and ultimately focused on the sample. Subsequently produced secondary electrons are measured by a detector, which then sends the information to be analysed.

Preparation Methods for SEM

Conventional SEM demands that water and organic fluids must be removed from biological samples, and the sample must have a conductive surface. For that reason, sample preparation is a necessary to obtaining high quality SEM images, which was an objective in the current thesis. A short introduction to the theory behind the main steps of preparation of biological samples for SEM imaging will presented in the following paragraphs.

Fixation

The aim of fixation is to stop cellular processes whilst preserving the specimen as close as possible its natural state. Characteristics of a good fixitatives are that it permeates cells readily, are irreversible and do not cause fixation artifacts. There are two main methods of fixation; chemical and physical. Physical fixation is carried out either by exposing the specimen to very low temperatures (cryo-fixation) or very high temperature (boiling, microwave). Chemical fixatives fall into two broad categories: those that covalently crosslink macromolecules, and those that fix by denaturing and coagulating biological macromolecules. Denaturing fixatives such as ethanol, acetone and methanol preserve ultra-structure very poorly, while chemical cross-linking fixative offers better preservation of cell-tissue structures. [82]. Of the cross-linking fixitatives, glutaraldehyde (GA) is a often used, and was employed in this project. GA is a dialdehyde which can react simultaneously with two amines to form both inter and intra-molecular proteins crosslinks, ultimately converting the cytoplasm of all cell into a macromolecular gel [83]. GA preserves fine structure at least down to the level of macromolecular resolution and renders samples highly resistant to the various processing steps required to prepare them for SEM, and is therefore the fixative of choice for almost all biological SEM [**Hayat1981**].

Dehydration

Because cells are predominately composed of water, dehydration is potentially a very disruptive process, and several artifacts may be introduced, such as shrinking of the sample due to rapid loss of water or exposure to liquid air interface. Shrinkage is an unavoidable artifact of dehydration, caused by loss of waster that surrounds the macromolecules in the sample, causing them to collapse [82]. Therefore, samples are often dehydrated so as to allow them to shrink gradually, avoiding abrupt collapse [83]. Dehydration involves slow substitution of the water in the tissue with an dehydration agent, ethanol in this project. The standard protocol for the dehydration process to gradually passing the cell culture through a series

of increasing alcohol concentrations, where the last step uses anhydrous alcohol, to ensure that all water is removed.

Drying

Once the dehydration series is complete, the solvent itself must be removed from the sample. However, artifacts such as shrinkage and collapse of surface structures due to the effects of surface tension can be a problem if biological samples are air dried following dehydration [83]. This is due to the fact that substantial forces are created in hollow structures when a liquid/gas interface is present, causing collapse of the structures. Avoiding this is achieved through the use of a transitional fluid [83]. There are a multitude of different approaches to drying, the traditional method being critical point drying. Critical point drying was for a long time the method with the most favourable results, however, in later years, HMDS (hexamethyldisilazane) has often been used to replace the critical point drying step. Previous procedures required a Critical Point Drying apparatus to achieve the temperature/pressure combination to completely dehydrate the specimen, which is resource demanding [84]. HMDS on the other hand, brings the specimens to the same state of dehydrating without special equipment, with results equal to the previous methods [85]. To dry the sample using HMDS, ethanol is replaced by HMDS in gradual steps, and left to air dry. The key feature of HMDS is that it has a much lower surface tension than water and ethanol [86], evaporating without the introducing the high surface tension forces that damages the structure of the sample [87].

Coating

The last step is coating the specimen with an electrically conductive material, which is necessary to reduce the electric charge that builds up rapidly in a nonconducting specimen when it is scanned by a beam of high-energy electrons. It also reduces the microscope beam damage on the specimen, improves secondary electron emission and improves edge resolution [88]. This is typically applied using a tool called sputter coater; a plasma chambers with low discharge capability that he radiates a target made of heavy metal with argon atoms, such as gold or palladium. Sputtered films typically have a thickness range of 2–20 nm [88]. It is critical that the coating is thick enough to prevent charging, but not so thick that to obscure specimen surface details.

2.4.5 Immunocytochemistry

Immunocytochemistry (ICC) was employed in this project to investigate the effects of nanotopography SU-8 growth surfaces on neural cell properties. An explanation of the technique is therefore due.

The technique of immunocytochemistry (also referred to as immunostaining in this project)[2] is used in order to selectively bind the reporter tag to a specific protein or antigen in cells, thereby allowing visualization and examination under a microscope. In order to achieve this, the reporter tag is conjugated to an antibody which exhibits high affinity to a specific sequence of amino acids in a protein (antigens) that is present in a region of the cell which is of interest. Antibodies are large Y-shaped proteins used by the immune system to identify and neutralize intruding foreign objects in the body [89]. The antibody reporter tag conjugate is then added to the cell environment, and if the antigen in question is present in the cell, the antibody will bind [90]. There are a variety of different variations of ICC, but in this project, indirect immunocytochemistry was employed. This process uses an intermediate step of first binding an antibody directly to the antigen of interest (primary antibody), on which a secondary antibody, conjugated with the reporter tag, is subsequently bound (see Figure 2.12 for schematic illustration). The advantage of indirect immunocytochemistry is firstly the increased sensitivity due to signal amplification from multiple secondary antibodies binding to a single primary antibody. In addition, a given secondary antibody can be used with any primary antibody (of the same type and host species), making it more versatile than direct ICC, where one antibody is used to label one specific target.

Indirect ICC is traditionally carried out by first selecting a primary antibody, often produced by an animal, that selectively binds to the antigen of interest, and then select a secondary antibody that stems from another animal than the primary antibody, and has an affinity to the primary antibody used. An example of this could be to begin with an MAP2-chicken primary antibody, where the antibody stems from a chicken and has an affinity to MAP2 (microtubule-associated protein 2). And then select a secondary antibody from for example a goat, giving the antibody goat-anti-chicken, conjugated to the reporter tag.

[2] immunostaining is a general term used as a verb in describing both immunohistochemistry and immunocytochemistry, where immunohistochemistry targets biologic tissue, and immunocytochemistry target cells.

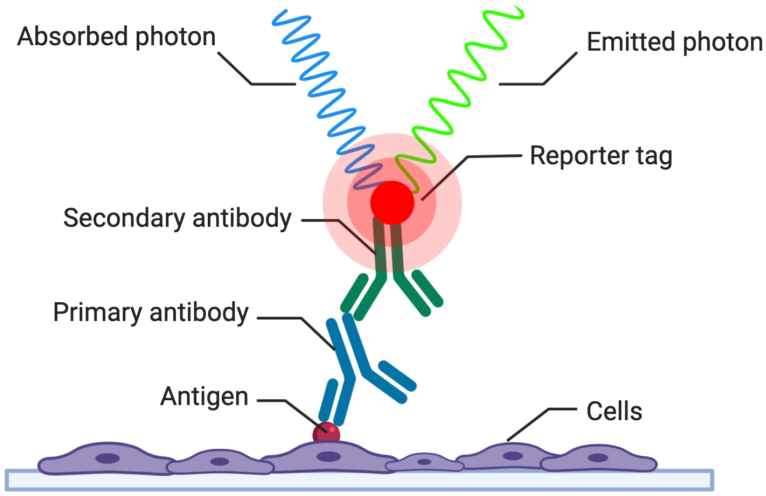

Figure 2.12: Schematic illustrating an indirect immunocytochemistry setup. The primary antibody will bind to a specific antigen present i the cell culture. The secondary antibody, which is connected to the primary antibody, is linked with a reporter tag, which emits a signal that can be detected.

It is furthermore common to add a series of blocking agents, to avoid nonspecific binding of antibodies, as this would result in signals from unwanted regions in the cell. In order to ensure that the antibodies are permitted into the cell, the cell membranes are 'opened' with the use of detergents, which effectively permit the antibodies to penetrate the cell membrane. Detergents are polar lipids, comprised of a polar and apolar end, and can bind the apolar region in the centre of the cell's lipid bilayer [91].

2.4.6 Extracellular Recording

ICC and SEM do not address the dynamic function of neural networks, only the static arrangement. One technique to asses the dynamic function neural networks in vitro is to measure the electrophysiological activity. A common technique for this is extracellular recording, and was used in this project.

Extracellular recording seeks to study the electrical signalling of neurons, and investigates this by the detection of the AP from outside of the neuron. Extracellular recordings can be used to answer a plethora of questions regarding neuronal network behaviour, such as neuronal communication, information encoding, propagation, processing and computation of neuronal circuits [92]. In in vitro studies, a common method of extracellular recording is integrating an array of extracellular electrodes are placed on the interface between surface and neuronal cells, a so called an microelectrode array (MEA). There has been developed a variety of different MEAs with each their own advantages and disadvantages, these have been thoroughly reviewed with respect to various properties in a number of review articles [92–94]. The main advantages with such electrodes in general is the capability to record and stimulate neurons at multiple sites simultaneously, as well as long-term recordings, with reported recording duration of several month [95]. Furthermore, the ease in fabrication and the ability to integrate the arrays on to transparent glass substrates makes it largely applicable for experimental research.

The electrode does not directly measure the potential change that occurs inside the cell. Rather, it measures a proxy: detects the changes in the medium potential around the electrode itself (i.e. the local field potential). If neurons are positioned in proximity to the electrode, and AP will generate a fluctuation in the ionic concentration around the electrode which is detected. In short, the detection of these ionic changes in the extracellular space results in a prototypical voltage curve, a so-called triphasic waveform [96], which, if sufficiently strong, is counted as a spike. A detailed description of the working principles of extracellular recording is beyond the scope o this text, but many excellent articles on this exists [97]. Common spike patterns extracted from data acquired from MEA recordings are *bursts*: a group of action potentials generated in rapid succession, followed by a period of relative quiescence [98]. Bursts inhabits numerous different features that bear information and function in neuroscience, such as synchronization, information carrier, and motorpattern generation [92]. Two main functional roles of bursts have been proposed. First, since most

synapses are unreliable, bursting could be a way to enhance reliability in information transmission. Second, bursts can carry additional information and thereby expand the coding space [98]. Furthermore, bursts may synchronize across in vitro neural networks, to produce what is called *network bursts* (NB). NBs are associated with increased efficiency in propagation of neuronal information, signaling and network functionality [99].

With the abovementioned neural network spiking phenomena in mind, the parameters of interest in this project was: The *firing rate*, a measure of how many spikes are detected per minute network-wide. *NBs rate*, defined as the number of NB detected per minute, and the mean size of NBs, measured as the average number of electrodes involved in network bursts. A further explanation of the technical details of how these parameters are attained will be explained in Methods and Materials 3.2.4

2.4.7 Waxman Algorithm For Network Simulation

In the analysis of the cultured neural networks in the experiments conducted in this thesis, an automated script for simulating the neural networks and calculating the topological features of the network was developed. The core of this computational analysis was the Waxman algorithm. The following section will give a brief introduction to inner workings of this algorithm. The implementation of the algorithm, together with the data processing pipeline, will be further discussed in Methods Section 3.3.2.

The Waxman model was originally developed by Bernard Waxman in 1988, in his paper, "Routing of multipoint connections", where he addressed the problem of routing connections in a large-scale networks [100]. Since then, it has been adopted into the field neuroscience, where it has been employed by several papers to address the topology of neural networks [30, 39, 101]. For neural networks, the nodes represent neurons, and the edges represent axons, as already discussed in Section 2.1. Essentially, the Waxman model establishes edges between nodes, whereby the probability an edge between two nodes exponentially decreases with the Euclidean distance between those nodes. Thus, underlying assumption of the Waxman algorithm, when applied to neural networks, is that the probability of a connection between two neurons decays exponentially with neuron-neuron distance, this has been validated as reasonable hypothesis by several independent papers [101]. More specifically, the Waxman algorithm connects two nodes, u and v, if

$$\alpha e^{\frac{-d(u,v)}{\beta L}} \geq R \tag{2.5}$$

where d is the Euclidean distance between nodes u and v, and L is the largest possible Euclidean distance between two nodes of the graph. R is a stochastic variable, between 0 and 1, generated for each iteration of the algorithm. In the equation, α and β are the Waxman model parameters and, and are chosen between 0 and 1. These parameters affect the number of the edges, and thus the connectivity of the graphs. Smaller values of these parameters yield a smaller number of edges, and if it is set too low, it is not possible to extract the organizational characteristics of the nodes as there are not enough edges. Conversely, selecting values towards unity produces very dense graphs, with almost every node connected to every other node. In this case, topological properties of different networks can be difficult to distinguish, as the graph is over-connected. However, currently no agreement exists over the typical values to be selected for these two parameters: Waxman himself sets $\alpha = \beta = 0.4$ [102].

Chapter 3

Methods and Materials

In this section, an explanation of the methods and materials employed throughout this project is presented. All fabrication work mentioned was carried out by Leik Isdal, thorough documentation can be found in his thesis [73]. Fabricated chips were delivered to the author, who conducted the remainder of the project pipeline: cell culturing and analysis of cell behaviour. Cell culturing protocols have been adapted from Nicolai Winter-Hjelm's Masters thesis [103]. More comprehensive protocols describing the cell culturing can be found in Appendix A.2.

The pipeline of this project can be be divided into 3 phases. Phase 1 was devoted to verifying and optimising protocols for cell culturing and imaging by ICC and SEM, and a script for *in silico* modelling was developed. In phase 2, an array of surfaces (with S_a ranging from 0 nm to 150 nm) were screened for cell viability and optimal cell behaviour, by culturing neuronal cell cultures on them. In phase 3, the optimal surface roughnesses from the above screening process were advanced to be used to investigate the effect of the nanotopography on cell behaviour, employing the optimised methods from phase 1. Additionally, nanotopography surfaces were integrated into microfluidic platforms, coupled with microelectrode arrays, for analysis of electrophysiological activity. Figure 3.1 illustrates the chips in which the surfaces were implemented, and subsequently seeded with neuronal cells.

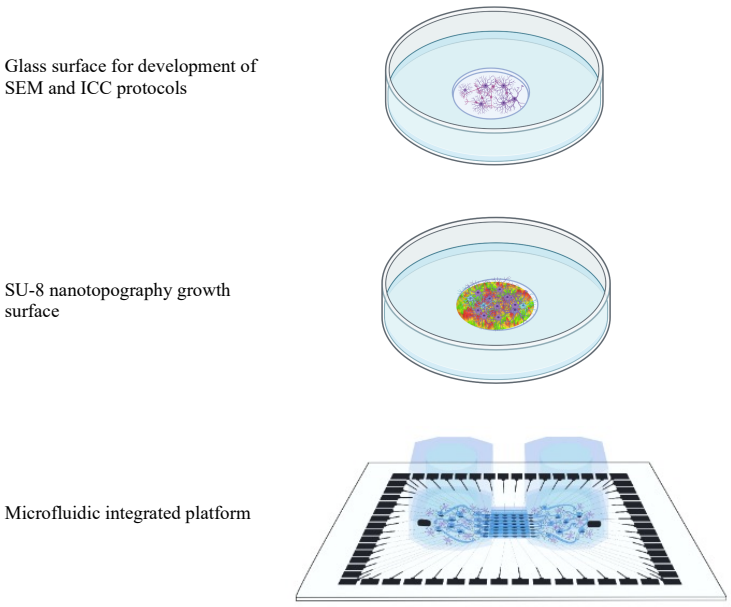

Figure 3.1: The chips employed throughout the project. Initial protocol development was carried out in the top chip, which was a standard planar glass slide. The first nanotopography SU-8 surface can be seen illustrated below, the colour of the surface indicates the nanotopography. With these, screening for cell viability and analysis of neuronal cells was conducted. Lastly, the SU-8 surface was integrated into a microfluidic integrated platform, to allow for extracellular recording of the neural networks. Schematic of microfluidic chip made by Nicolai Winter-Hjelm.

3.1 SU-8 Nanotopography Characterisation

All characterisation of the SU-8 surfaces was conducted by Leik Isdal. The results from these measurements were used in the results in this thesis [73], as it was deemed instructive to clarify the properties of the surfaces investigated.

Atomic Force Microscope

To quantitatively evaluate the degree of roughness of the nanotopography SU-8 growth surfaces, atomic force microscope was used. All measurements were taken with Nanolab's Dimension Icon AFM from Bruker us-

ing the ScanAsyst mode, which combines tapping and contact mode and automatically optimizes parameters such as feedback gain, setpoint and scan rate. Two different probes were used depending on the approximate degree of roughness of tested samples. ScanAsyst Air probe from Bruker was used for the lesser rough surfaces, with resonance frequency 70 kHz and spring constant 0.4 N/m. Rougher samples were measured with the RTESPA-300 probe from Bruker, with resonance frequency 300 kHz and spring constant 40 N/m. Acquired images were processed and analyzed, using the software Gwyddion [73].

Scanning Electron Microscopy of Topography

SEM imaging was used to qualitatively examine the topographies, using Nanolab's APREO Field Emission Scanning Electron Microscope (SEM) from FEI. This was carried out after the etching of the SU8. Samples were coated with 2 nm Pt/Pd and mounted on a 8 mm diameter sample holder with double sided copper tape, which in turn was mounted on the SEM sample stage. Samples were electrically connected to the sample stage by conductive copper tape attached at one end to the top of the sample and at the other to the sample stage. Images were taken in immersion mode, and detecting secondary electrons, with the beam current set to 6.3 pA and acceleration voltage to 2 kV. Image processing was done in Fiji ImageJ (NHI).

3.2 Analysis of Neuronal Cultures

In order evaluate the effect on cell behaviour of the various implemented topography parameters, the surfaces were seeded with with rat primary cortical astrocytes (ThermoFisher: N7745100) and primary rat cortex neurons (Thermofisher: A1084001). Fully detailed protocols explaining these steps are added in Appendix A.2. The following subsections explain the methods of analysis employed throughout this project.

3.2.1 Optical Microscopy

Neurite outgrowth dynamics were analysed with phase contrast microscopy using Zeiss Axio Vert 25 throughout the cell culturing process. Phase contrast was found to give the best quality of micrographs. Depending on

what aspects of the microfluidic design were in interest, magnifications from 5x to 40x were used. Data was processed and analysed primarily with ImageJ (NIH).

3.2.2 Immunocytochemistry

ICC was carried out closely following the theory of ICC discussed in Section 2.4.5. The process is comprised of a number of steps, which will be divided into: fixation, blocking, primary and secondary antibodies, and storage. All ingredients are from ThermoFisher if nothing else is stated.

Fixation

In order to preserve cell morphology, the cells were firstly fixated with a glyoxal solution (sigma aldrich 128465). Half of the media in was first removed, and then refilled with the glyoxal solution. The chips were then incubated at room temperature (RT) for 15 minutes. Following this, the glyoxal solution was aspirated and disposed properly (in a separate waste). Them, washing with PBS three times at 15 minutes per cycle followed. It was critical from this point on that the cells did not dry out, as this would cause increased levels of background staining and difficulty interpreting staining results.

Blocking

To avoid unspecific binding of antibodies, a blocking agent (goat serum (Merck G902))) was added to the cell culture. Furthermore, in order for the active ingredients to penetrate the cell membranes, a permeability agent was added (Triton X-100 (Sigma-Aldrich T8787-60ML)). Thus, a solution consisting of 5% goat serum, 0.3% Triton X-100, mixed in PBS (Sigma-Aldrich D8537-500mL) was made. The solution was added to the chambers, and subsequently incubated for 2 hours at RT on a shaking plate. As before, a volume gradient was established to ensure proper flow through channels.

Primary Antibodies

All primary antibodies used were from from Abcam, the product number is noted for each antibody in brackets.

The blocking solution was first aspirated, but not washed afterwards. A solution containing 1% goat serum, 0.1% Triton X-100 and the selected primary antibodies in PBS was made and added to the chambers, with a gradient to ensure flow. The primary antibodies used for micrographs were rabbit monoclonal anti-NeuN IgG antibody (ab177487), mouse monoclonal anti-β3-tubulin IgG antibody (ab78078), chicken monoclonal anti-GFAP IgG antibody (ab4674). The petri-dishes edges were then covered in parafilm, to prevent evaporation, and placed on a shaking plate at 4 °C overnight.

Secondary Antibodies

Firstly, the chambers were washed three times (15 min per cycle) with PBS. A secondary antibody solution consisting of 1% goat serum (catalog 16210064), 0.1% Triton X-100 in PBS and the secondary antibody was made, and added to the chambers with a volume gradient. A variation of specific secondary antibodies and conjugated fluorescent reporters were used, to express different features of the cells. The secondary antibodies were all from goat, and the theory of Section 2.4.3 was used to select compatible secondary antibodies to the primary antibodies. These were goat anti-rabbit IgG, Alexa Fluor Plus 488 (A32731), goat anti-mouse IgG, Alexa Fluor Plus 647 (A32728), and goat anti-chicken IgY, Alexa Fluor 546 (A11040) The chips were then incubated for 3 hours at RT in the dark on a shaking plate. The chips were then washed three times with 15 minutes per cycle with PBS. Following this, Hoechst was applied for 5 minutes. Hoechst (Merck 94403) was used mark all cells in general (binds to DNA), and served as a control to validate the presence of cells (note that Hoechst is not ICC). Lastly, the chips were washed three times with PBS, as before.

Storage

In order to store in a suitable manner until imaging, chips were filled with PBS. The petri-dishes edges were tightly covered with parafilm and then covered with aluminum foil and stored in a cool room.

Imaging

The epifluorecence microscope Invitrogen EVOS M5000 was utilized to image the cell cultures. An integrated LED system in the microscope was tuned to match the absorption/emission spectrum of the respective fluorescent reporter used. For acquiring optimal micrographs the parameters light, exposure and gain were tuned. Throughout an imaging session, (in order to acquire comparable data) light, exposure and gain were held constant, as well as the threshold function in ImageJ.

3.2.3 SEM

SEM was employed to acquire ultra high resolution qualitative micrographs of the cell's interaction with the topography surface. In the same manner as for ICC, a number of preparation steps is required for the cells to be viewed with the SEM instrument.

Fixation

Cell media was removed and the samples were rinsed with phosphate-buffered saline (PBS) twice, functioning as a washing step removing any debris and dead cells suspended in the liquid. PBS was then removed and the samples were fixed with 2.5% glutaraldehyde (G5882 Sigma-Aldrich) in Sorensen's phosphate buffer (0.1 M, pH 7.2)) (Chemi-Teknik AS, EMS, 16320), with a volume so that the cells are just covered. Glutaraldehyde crosslinks the proteins in the cell, fixating the structure for analysis. The samples were then placed in larger petri dishes and sealed with parafilm and left to incubate overnight at 4°C.

Dehydration and Drying

Water was then chemically extracted from the specimen by the process of serial dehydration with ethanol, in steps from 30p% to 100%, in 20% increments (10% for the last), for 10 minutes per step, with agitation. After the last step, 100% ethanol was changed three times (it is important that the 100% is a completely anhydrous ethanol). The samples were then transported to NTNU Department of Physics, where further dehydration with hexamethyldisilazane (HMDS (8.04324 Sigma-Aldrich)) was carried out.

In the same manner, serial drying was conducted (starting with 2:1 (ethanol:HMDS), then 1:1, then 1:2, then 100% HMDS, which was changed three times). At the last step, as little HMDS as possible, while still completely covering the cells, was used. Lastly, the samples were left in a fume hood overnight, to let the HMDS completely evaporate.

Sputter Coating

To prevent charge build-up on the specimen surface, the samples were sputter coated with 15 nm Pt/Pd with 208 HR B Sputter Coater from Cressington, with active manual tilting throughout the sputtering, from -45°C to +45 °C. Before insertion into the SEM chamber, the samples were mounted on a metal stub using double sided copper tape, and a single copper tape strip was placed on the edge of the sample, electrically connecting it with the metal stub to increase conductivity.

Imaging

Imaging was done with Nanolab's APREO Field Emission Scanning Electron Microscope (SEM) from FEI, detecting secondary electrons, using pre-optimised settings in immersion mode (low voltage (1 kV) and low current (3.1 pA), working distance from 2 mm to 8 mm) and tilt between 0 and 45°, and with magnifications from 1200x to 8000x.

3.2.4 Extracellular Recording

A 60-electrode MEA2100 recording system from MultiChannel Systems MCS GmbH was used to do recordings of the MEA microfluidic chips. Recordings were started 4 days after seeding of neurons, however, only recordings from 8 DIV were used for electrophysiological analysis. The recordings were consecutively repeated every second day. The culture was maintained at 37 °C during recording, and each recording was set to 15 min. To compensate for any initial voltage drift in the system, from transport of the culture, a 5-minute lapse was allowed for the data acquisition before the start of recording. Raw data acquired was converted to Hierarchical Data Format 5 (HDF5) files. The sampling frequency was 10 kHz. A filter was applied to the raw signal to separate the spikes from noise. This is done by applying a Butterworth filter, with a high pass cutoff at 200Hz,

to attain higher signal to noise ratio (SNR) and lower false positive rates. From this filtered data, spikes were detected using an amplitude threshold, set at 5.0 standard deviations (SD) above the threshold and -5.0 SD below the threshold

The firing rate, network burst detection and coherence index were all captured through preexisting in-house MATLAB scripts. The firing rate was computed from the total number of spikes divided by the length of the recording, while network burst and the coherence index were computed as described below. Network bursts (NB) were found by binning the recording into 50 ms bins. The average firing rate was then found for each of the bins. If the firing rate exceeded the firing threshold in a bin (mean firing + 5*SD from the whole recording) and more than 20% (5 electrodes) of the network was active, it was considered part of a network burst. Furthermore, consecutive bins that met condition of being in a network burst, were counted as parts of the same burst. From this analysis, the frequency of NBs in each recording were found.

3.3 Data Acquisition and Analysis

A number of different analysis methods were employed to evaluated the cell behaviour as a function of the topography parameters. Measures were taken to ensure that the acquisition and analysis of data was not subject to bias; the following subsections will explain the procedures employed.

3.3.1 Acquisition

Imaging

To ensure unbiased sampling selection, ROI of images (for ICC, SEM and phase contrast microscopy) were selected at random. For analysis of individual cells, the same randomized procedure was applied, so that all cells of interest had equal probability of being selected. Surfaces were labeled with dummy variables upon analysis, to avoid subjective selection of data, and original names were recovered after collection of data was done. Throughout acquisition and processing of micrographs, all imaging and processing settings were kept constant, in order to acquire comparable values. The settings values were chosen after some preliminary testing and was not

critical for the result, as they were kept constant.

Extraction of Nuclei Positions

Neuron nuclei positions were extracted by collecting the signal from the ICC NeuN marker. Five micrographs with ROI of $20mm^2$ with approximately 300 cells were acquired from each topography chip. The micrographs were inputted into ImageJ. An automated script was developed for separating the wanted signal from noise, and then separate any overlapping signal. This was done by firstly converting the image to 8-bit. Then, a the built-in Gaussian Blur filter was applied, to blur out noise and "speckle" and also to smooth out the inhomogeneity of the NeuN signal. The Gaussian Blur filter uses convolution with a Gaussian function. The adjustable parameter, *sigma*, is the radius of decay to exp(-0.5), i.e the standard deviation sigma of the Gaussian function. A sigma value of 2 was selected (if sigma is too small, the segmentation will be disturbed by noise and staining pattern. On the other hand, if it is too high, the nuclei will be too blurred, making it harder to find edges precisely and separate them.). A threshold filter was then applied, and was set at the point where detailed neurite signal was included, without including excessive noise. To separate any overlapping signal, caused by nuclei being stacked on top of each other, a Watershed Segmentation algorithm was applied [104]. The image was then analysed for particles, using the built-in Particle Analyser in FIJI, setting the interval of size inclusion to 200 μm^2 to infinity, to avoid including noise signal that had not successfully been filtered. It should be noted that the lower size threshold for inclusion was not found to be of realistic scale. From qualitative inspection of the raw NeuN images, it was confirmed that even the weaker nuceli signals were included in the particle analysis process presented above. The resulting analysis table were exported as .csv and then imported into the analysis tools employed. Images from each step is presented in Figure 3.2.

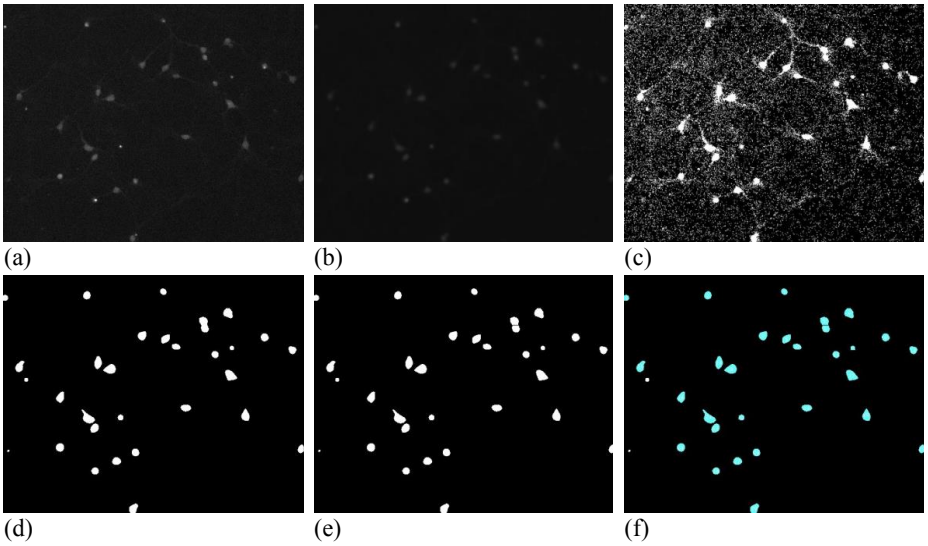

Figure 3.2: Presentation of the steps applied in processing the raw micrograph of NeuN signal. (a) shows the original micrograph taken with an EVOS microscope, which was then converted to a 8-bit image and passed through a Gaussian filter, which gave image (b). A threshold function was then applied, which gave image (c). By reducing the threshold to the level where noise and "speckle" was removed, image (d) was obtained. In order to overcome the issue of cell signal overlapping, a watershed algorithm was applied, which gave image (e); where overlapping signals in the upper right area can be seen to be successfully separated. Lastly, the in-built Particle Analyser function was applied, including particles above 200 μm^2, and the resulting table was exported as a .csv file.

3.3.2 Analysis

Several methods were employed to analyse the acquired data, these are briefly explained herein.

Morphology of Neurons determined from SEM

SEM images with 100x magnification, at a tilt of 45was acquired, and morphology features were analysed by manual edge detection and then using the built in Measure function in FIJI. Roundness was calculated according to the following formula:

$$R = \frac{4A}{\pi(M_a)^2} \tag{3.1}$$

where R is the roundness, A is the area, and M_a is the major axis of the measured shape.

Network density and neurite size determined from ICC

The cell cultures stained with beta-III-tubulin as imaged, at a magnification of 4x. 6 images of each surface was taken. The images were converted to 8-bit and binary, and a threshold of brightness of signal was applied, using the built in threshold function in FIJI. The threshold was set at 0-33. The remaining neurite mesh was measured with the built in Measure tool in FIJI, and the total area of neurite mesh was thus acquired. The final value of neurite area per cell was obtained by dividing the total area found here, with the number of neurons present in the ROI, as found by analysing the NeuN signal, as explained above.

Neural Network Simulation: Waxman Algorithm

In order to evaluate the topological properties of the neural networks, the networks were simulated employing a semi-automated script developed by the author. The core of this simulation was the Waxman model, which was described in Section 2.4.7. Firstly, the coordinates of neuron nuclei were extracted using the same procedure as explained in Section 3.3.1. These coordinates were saved as .csv and inputted into the developed Waxman model. The script for the model was written in Python (Python Software Foundation. Python Language Reference, version 2.7), and can be found here [1]. The code was adapted from the NetworkX [105] package Waxman Graph, and can be found here [2]. To quantify properties of network, Networkx packages for analysis of graph were employed. These were: average

[1] https://github.com/edehvide/Waxman-model.git

[2] networkx.org/documentation/networkx-1.10/reference/generated/networkx.generators.geometric.waxman_graph.html

shortest path[3], average clustering[4] and small worldness[5]. The theory of the abovementioned metrics are explained in Section 2.1.2.

For this experiment, the model parameters, α and β were set to 1 and 0.065, respectively. The documentation for choice of parameters can be found in Appendix A.1.2.

3.3.3 Statistical Analysis

All results are presented by the mean ± standard error of the mean. Significance in data comparison was assessed using the one-tailed non-parametric Mann Whitney U test. P-values of comparisons are noted when presenting results, and values below 0.01 were deemed significant.

[3] networkx.org/documentation/networkx-1.3/reference/generated/networkx.average_shortest_path_length

[4] networkx.org/documentation/stable/reference/algorithms/generated/networkx.algorithms.cluster.average_clustering

[5] networkx.org/documentation/stable/reference/algorithms/generated/networkx.algorithms.smallworld

Chapter 4

Results

In this project, the effects of nanotostructured SU-8 growth surfaces on neuronal cells and neural networks were studied, and these surfaces were implemented in dual chamber microfluidics coupled with MEAs. Protocols for preparations for SEM imaging (fixation, dehydration, coating) and ICC were verified and further optimised, and a Waxman model for computational analysis of network topology was developed. These served as the methods of analysis throughout the project, and were used to answer the research questions posed. The experiments of this thesis was divided into three distinct phases.

Phase 1 was devoted to verifying and optimising protocols for cell culturing and imaging by ICC and SEM, and a script for modelling neural networks with the Waxman model was developed. In phase 2, an array of different topography parameters were seeded with neuronal cells, on nanotopography SU-8 surfaces mounted in petri dishes, in order to screen for optimal roughness in terms of cell viability. Planar surfaces were included as control surfaces. The findings of this screening process were then employed in the third phase, where the effects of nanotopography on neuronal cells were systematically studied employing the abovementioned developed analysis methods. In the third phase, the nanostructured SU-8 surfaces were implemented into microfluidic integrated platforms (MIPs), and electrophysiological recordings of neuronal cell cultures were conducted.

The following chapter will present the experimental results acquired in this project. A short summary of the results from the fabrication process will be presented first. This work was conducted by Leik Isdal, and for more details on this process, the reader is directed to his thesis [73]. Then, the

results acquired from experiments conducted will be presented, structured in a manner where each subsection attempts to answering one research question each. Lastly, the findings regarding the objective of verifying and developing protocols for SEM will be presented.

4.1 Fabrication Process

4.1.1 Characterisation of Nanostructured Surfaces

In order to produce SU-8 surfaces with a roughness range from $S_a = 0$ nm to $S_a = 150$ nm, the parameters of the etching step were tuned and optimised, which is documented in Leik Isdal's thesis [73]. Table 4.1 presents an overview of all values of S_a explored in this project. The surface roughness of the surfaces was measured quantitatively by AFM, and SEM was used for qualitative characterization. Figure 4.1 presents representative SEM micrographs and AFM profile image of surfaces with an average roughness from 0 nm to 150 nm.

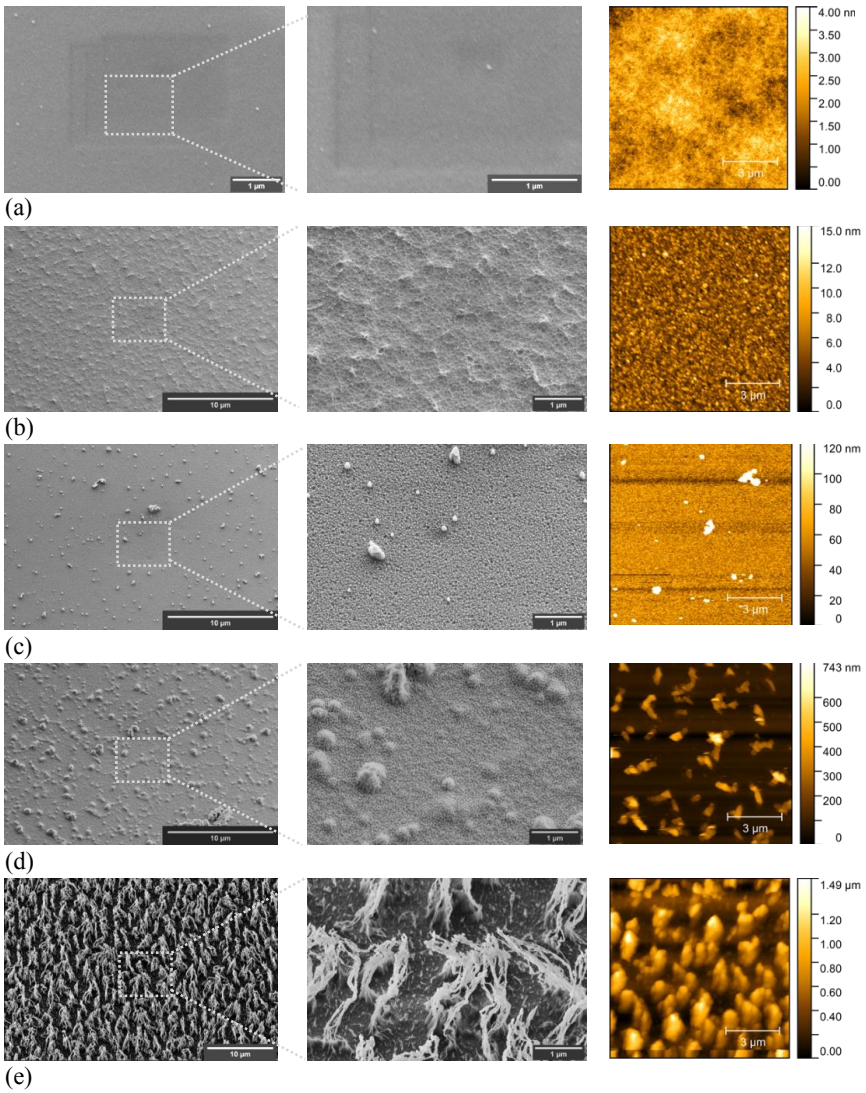

Figure 4.1: Form left to right: SEM micrographs taken at 8 000x and 35 000x magnification, and AFM profile of surfaces cultured with neuronal cells in this project. For row (a), magnification is 35000x and 65000x. For the surface row (a), $S_a = 0$ nm (planar SU-8 control), (b) $S_a = 1.3$ nm, (c) $S_a = 6.8$ nm, (d) $S_a = 10.3$ nm and (e) $S_a = 150$ nm. Images acquired by Leik Isdal.

Table 4.1: Average Roughness (S_a) of Surfaces (nm). investigated throughout the project

Phase 1:	25 nm	50 nm	75 nm	150 nm
Phase 2:	1.3 nm	6.8 nm	10.3 nm	
Phase 3:	4.7 nm			

4.2 Effect of SU-8 Nanotopography on Cell Viability

Perhaps the most fundamental requirement of an in vitro cell culturing platform, is that it provides a viable cell environment, and was thus formulated as the first research question in this thesis. Cell viability was systematically monitored to screen for the optimal roughness with regards to cell viability. From these results, roughness values for further analysis were selected. In the following subsections, the results form investigating the effect of SU-8 nanotopography on cell viability will be presented. The name of the titles indicate the roughness values investigated in the respective subsections.

4.2.1 S_a = 25 nm, 50 nm, 75 nm, 150 nm

An initial finding was that nearly all neuronal cells seeded on the nanotopographical surfaces displayed characteristics of having undergone necrosis after 4 DIV, such as a shrunken soma and absence of visible neurite extensions. In contrast, cells seeded on the glass control surfaces exhibited good cell viability, and neurons were clearly seen to have adhered to the surface and initiated neurite outgrowth. For SU-8 planar control, cell viability was observed to be in between that of glass and topography surfaces, but with the majority of cells exhibiting a shrunken soma and absence of visible neurite extensions. Figure 4.2 presents representative images of the cells' response to the respective surfaces, with average roughness increasing from 0 nm to 150 nm, from image (a) to (f). Green circles indicate examples of healthy cells, adhering and growing on the surface with visible neurite outgrowth. Red circles indicate dead cells, exhibiting a shrunken morphology and lack of neurite outgrowth. Taking this together, the introduction of the surface topography was thought to be the factor causing, or at least associated, with the necrotic behaviour. Appendix A.1 includes

a further collection of images acquired in this analysis, to underscore the observations.

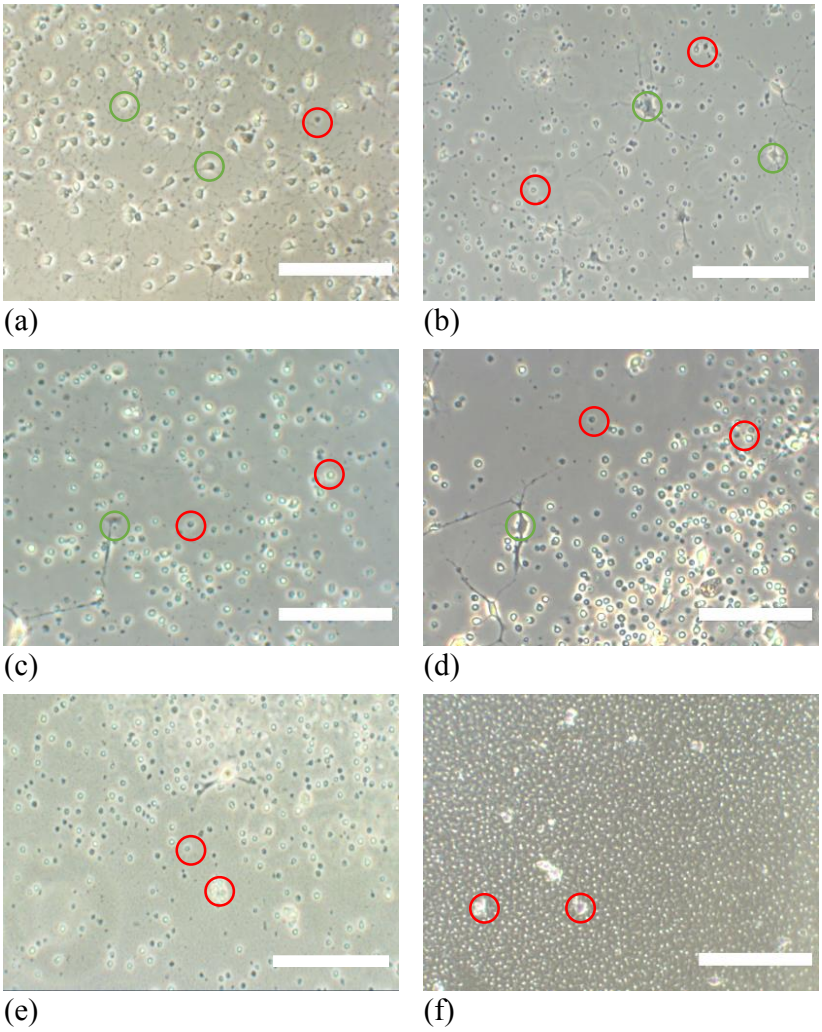

Figure 4.2: Representative images from surfaces cultured with cells, in increasing roughness. (a) 0 nm (glass control), (b) 0 nm (SU-8 planar control), (c) S_a = 25 nm, (d) S_a = 50 nm, (e) S_a = 75 nm and (f) S_a = 150 nm. A typical dead cell is highlighted with a red circle in each of the images, and where living cells are present, an example is shown by circling with a green circle. All images have a scale bar of 150 μm. Images acquired by phase contrast microscopy at 5 DIV.

Due to an unforeseen issue of potential paraffin pollution on the surfaces in the first screening, a follow-up round of surfaces were fabricated and

seeded, for which the paraffin pollution was avoided. It is important to note that for this follow-up round, all surfaces were plasma cleaned, to increase the hydrophilicity of the surfaces. Two examples of each surface S_a was included in this follow-up round. This served to control that it was not the paraffin pollution that was the factor causing the low cell viability.

For the cells seeded on nanostructured surfaces, the seeded astrocytes[1] showed poor ability to adhere, with similar necrotic tendencies as seen before, as illustrated in Figure 4.3. Again, the cells on the control surfaces showed substantially better ability to adhere and initiate growth. This is highlighted with green circles in Figure 4.3 (a) and (b). Although apparently unhealthy cells are present in the controls, several astrocytes can be seen growing on the surface, in contrast to the nanotopography surfaces, which show no signs of healthy cells.

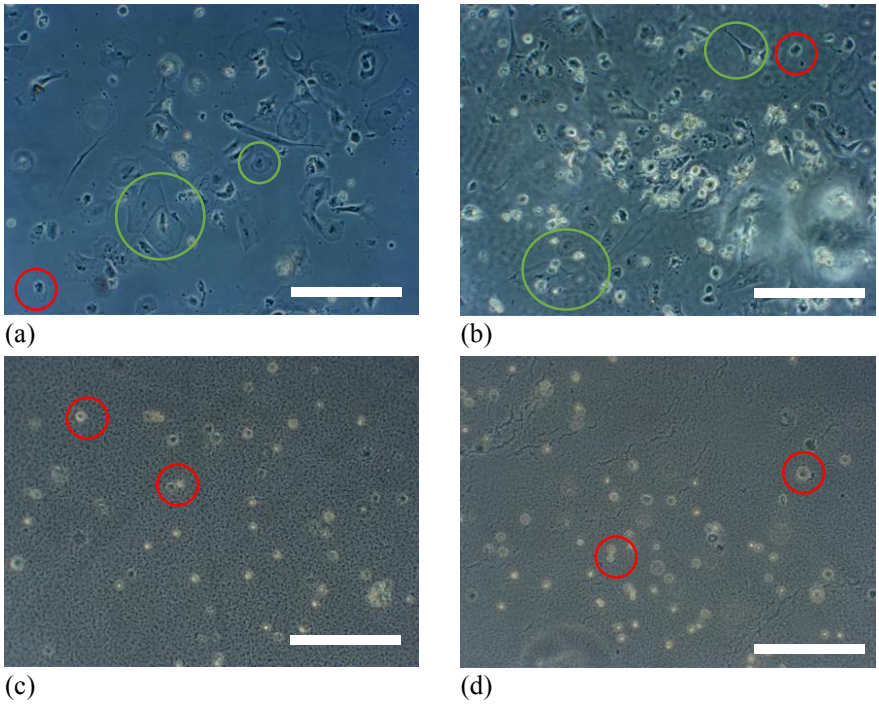

Figure 4.3: Representative images from surfaces that were not damaged. Image (a) shows glass control surface with $S_a = 0$ nm, (b) 0 nm (SU-8 planar control), (c) $S_a = 75$ nm, and (d) $S_a = 150$ nm. All images have a scale bar of 150 μm. Images acquired by phase contrast microscopy at 4 DIV.

[1]For this round of screening, commercial cells were taken in use, and according to protocol, astrocytes were seeded 2 days before neurons were seeded.

4.2.2 S_a = 1.3 nm, 6.8 nm, 10.3 nm

Based on the findings presented in Section 4.2.1, it was concluded that S_a above 25 nm was associated with low cell viability. Thus, further screening investigated the surfaces with S_a = 1.3 nm, 6.8 nm and 10.3 nm. This served as the final screening of nanotopography before the SU-8 growth surfaces were to be implemented into the MIPs. Therefore, the surfaces were analysed with an interest in detecting tendencies of healthy network characteristics. To carry this out, micrographs of ROIs (see Methods Section 3.3.1 for description of image acquisition process) were collected for each of the surfaces, and representative images of each surface is included in Figure 4.4. The images included are representative examples extracted from a larger dataset, added in Appendix A.1. Two examples of each surface were included, and planar surfaces were added as controls. Table 4.2 summarizes the findings of this screening, with regards to cell viability and key features observed in the cultured network.

Table 4.2: Summary of neuronal cell response to surfaces with S_a between 0 nm and 10.3 nm

0 nm:	High cell viability. Weak signs of mature network.
1.3 nm:	High cell viability. Strong signs of mature network.
6.8 nm:	High cell viability. Signs of mature network.
10.3 nm:	Low cell viability. Similar behaviour as for $S_a \geq 25nm$.

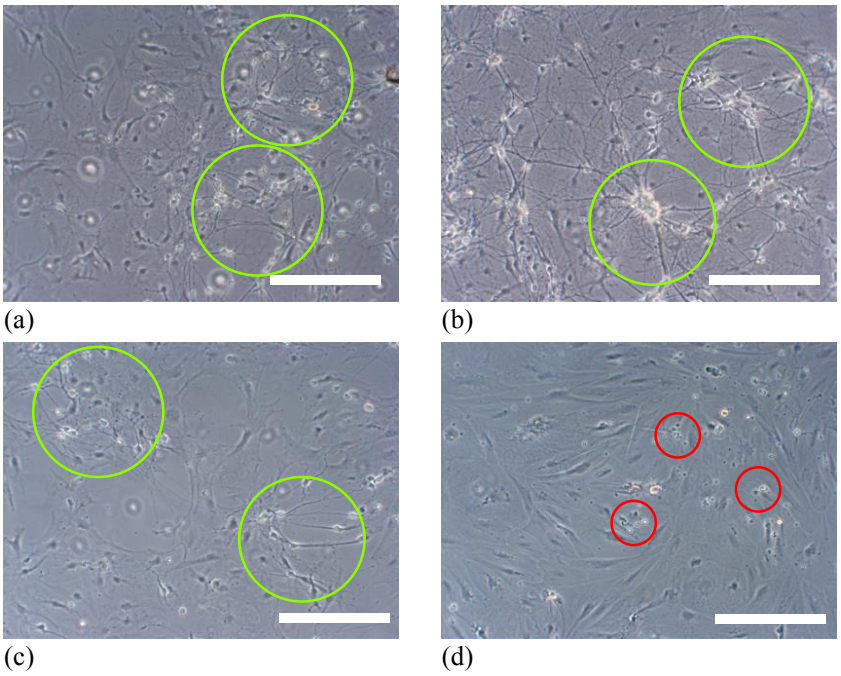

Figure 4.4: Representative images from central region of surfaces with (a) $S_a = 0$ nm (glass control), (b) $S_a = 1.3$ nm, (c) $S_a = 6.8$ nm, (d) $S_a = 10.3$ nm. The ROIs were selected at random, to avoid bias in analysis. Green circles in image (a) highlight regions exemplifying tendencies of neuronal networks forming. In image (b), the circle shows areas with large clusters and fasciculation (bundles) of axons between clusters. In image (c), the circles indicate areas with networks forming, but a clearly lower density than in image (e). In image (d), red circles show cells exhibiting a shrunken morphology similar to that observed for cells grown on surfaces with $S_a \geq 25$ nm, indicating cell death. All images have a scale bar of 150 μm. Images acquired by phase contrast microscopy at 14 DIV.

4.2.3 $S_a = 4.7$ nm

Based on the results from the above screening process, surfaces with $S_a = 1.3$ nm were selected to be integrated into the MIPs. Due to variability in the fabrication process, the surfaces obtained in the MIPs were measured to have an $S_a = 4.7$ nm. For a further discussion on this, the reader is directed to Isdal's thesis [73].

Three MIPs with an $S_a = 4.7$ nm were seeded, and two planar SU-8 chips were included as reference. Heretofore, analysis of cell viability has been

based on qualitative analysis of cell behaviour characteristics. In order to give a quantitative answer to the research question posed regarding cell viability, the fraction of cells that successfully had adhered to the surfaces was investigated. This was conducted 24 hours after seeding and images were acquired by phase contrast microscopy and analysis was conducted by manual counting. Cells clearly seen to have a rounded and shrunken morphology, were marked as dead cells, while adhered cells displaying a larger soma and neurite outgrowth, were marked as alive. Figure 4.5 shows a representative image from each surface, where the red and green circle indicate cells that were counted as dead and alive, respectively.

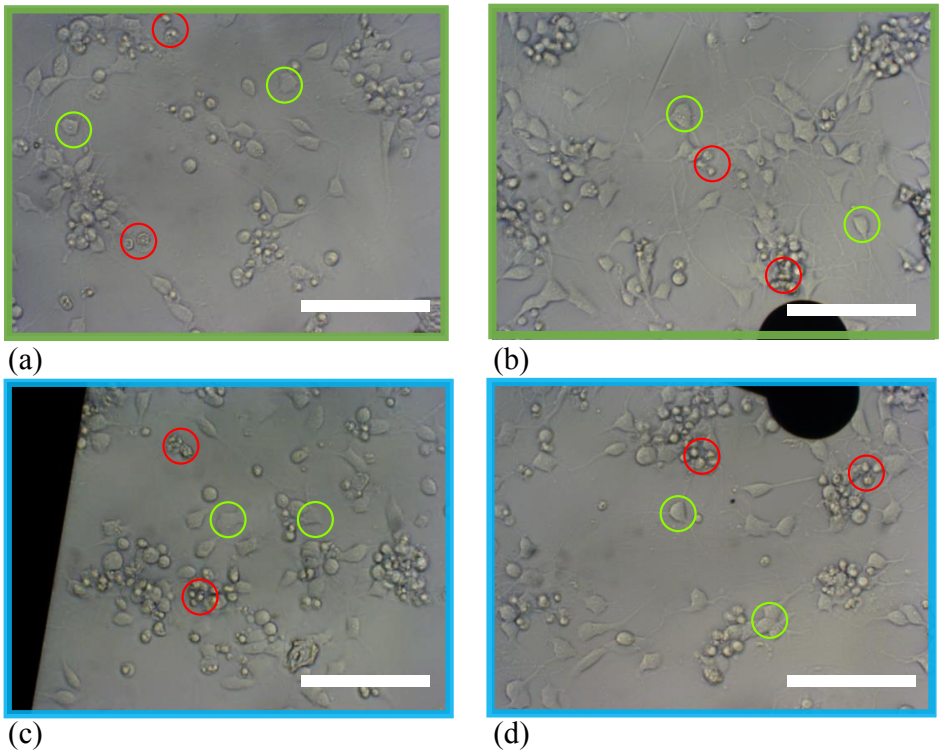

Figure 4.5: Phase contrast images of cells after 1 DIV. Cell count was conducted manually, by analysis of morphology of cells. A selection of typical healthy neurons, showing signs of neurite outgrowth, are indicated with a green circle, and a typical unadhered and dying cells are indicated by a red circle. Image (a) and (b) show cells cultured on $S_a = 0$ nm surfaces, while image (c) and (d) show cells cultured cultured $S_a = 4.7$ nm surfaces. Colour of frame corresponds to data displayed in Figure 4.5. All scale bars are 37.5 μm.

The calculated results of the analysis is displayed in Figure 4.6. The percentage of cells that had adhered and showed a typical healthy cell morphology was 47.8 % ± 11.8 %, 44.8 % ± 6.6 % for surfaces with $S_a = 0$ nm and 4.7 nm, respectfully. The values were statistically tested, and from this the populations were deemed to be insignificant from each other. Thus indicating that neither the surface material nor nanotopography had a significant effect on the initial neuron attachment or initial cell viability.

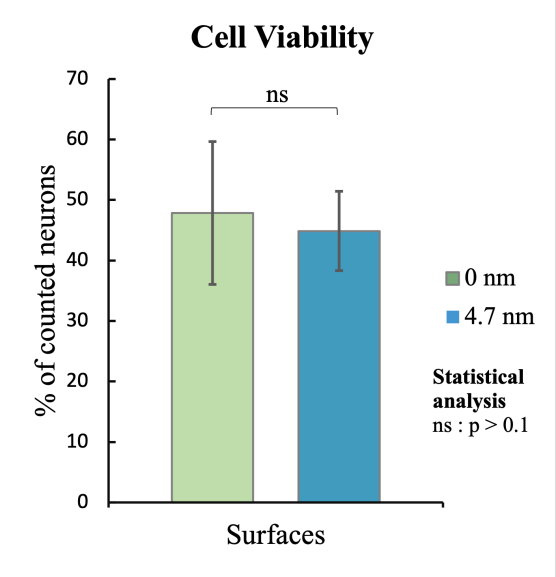

Figure 4.6: Histogram showing the percentage of seeded neurons that had adhered and started to grow on the surface after 24 HIV, which was found to be 47.8 % ± 11.8 % and 44.8 % ± 6.6 % for SU-8 control ($S_a = 0$ nm) and surface with S_a of 4.7 nm, respectfully. Colours of histograms corresponds to frames of micrographs in Figure 4.4.

4.3 Effect of SU-8 Nanotopography on Morphology: SEM Analysis

Now that the initial research question of this thesis has been addressed, the results acquired from the more advanced methods of analysis will be presented. Scanning electron microscopy (SEM) was employed to examine neurons with ultra high resolution at high magnification, and from this, the research question regarding the effect of SU-8 nanotopography on cell morphology was addressed. Secondary electrons were detected using op-

timised settings in immersion mode, with low acceleration voltage (1 kV) and low beam current (3.1 pA).

A qualitative investigation was first conducted, where a finding of interest was that cells cultured on planar glass and planar SU-8 exhibit a flatter morphology than that of cells cultured on topography surfaces, as can be seen in Figure 4.7 (a)-(b). Figure 4.7 (c)-(d) shows neurons growing on SU-8 surface with an $S_a = 4.7$ nm. It can be seen that the cells exhibit a less flat soma morphology, with a smaller area in direct contact with the surface, relative to what can be seen for neurons grown on planar surfaces in Figure 4.7 (a)-(b). It can furthermore me observed that the neurite outgrowth from the neurons in (c)-(d) are clearly suspended above surface level, in contrast to neurite outgrowth in (a)-(b), which can be seen to extend in a manner restricted to the 2D plane. Additional images underscoring these observations are included in Appendix A.1.1.

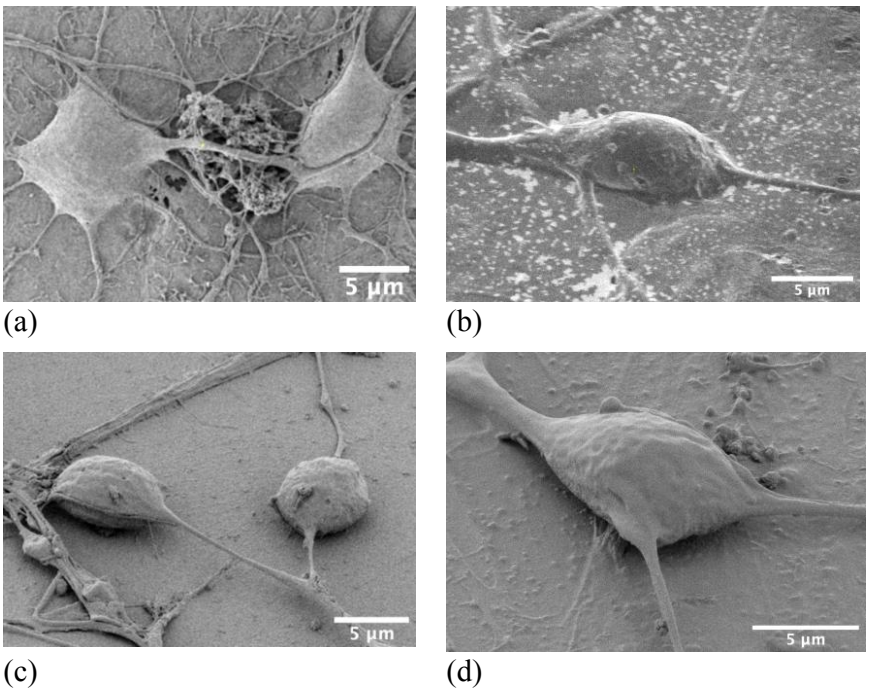

Figure 4.7: Investigation of neuron soma morphology as a response to surface topography. Images included were deemed representative of the general tendencies observed, an extensive collection of images is placed in Appendix A.1.1, to underscore the observations. Image (a) shows cells grown on a planar glass surface, exhibiting a flat geometry with a large contact area with the surface. Image (b) shows neurons cultured on planar SU-8 surfaces, exhibiting in the same manner as for the glass control, a large contact area with the surface. In (c) and (d), neurons cultured on nanostrcutured SU-8 with $S_a = 4.7$ nm is shown, and it can be seen that the cells exhibit a less flat morphology, with a relatively small area in direct contact with the surface. It can furthermore me observed that neurite outgrowth are clearly suspended above surface level. All scale bars are 5 μm.

To further investigate this qualitative observation, and attain quantitative data on these features, high resolution images of a random selection of cells were attained. An analysis of the geometry of the cells was then performed. 10 SEM images were taken of surfaces with S_a of 4.7 nm and 0 nm (planar SU-8 control). Images were attained at 755x magnification and 45° tilt, keeping all other settings constant. The images were exported to FIJI where a total of 67 cells from the nanoroughened surfaces, and 66 from the planar surfaces were analysed. Cells that directly interacted with other

cells were not included, to ensure that the neurons were only affected by the surface, as illustrated in Figure 4.7. Full size of all images included in analysis are presented in Appendix A.1.1. The area and roundness of these cells were then analysed, by manually tracing the periphery and exporting the measures to FIJI's built-in analyser.

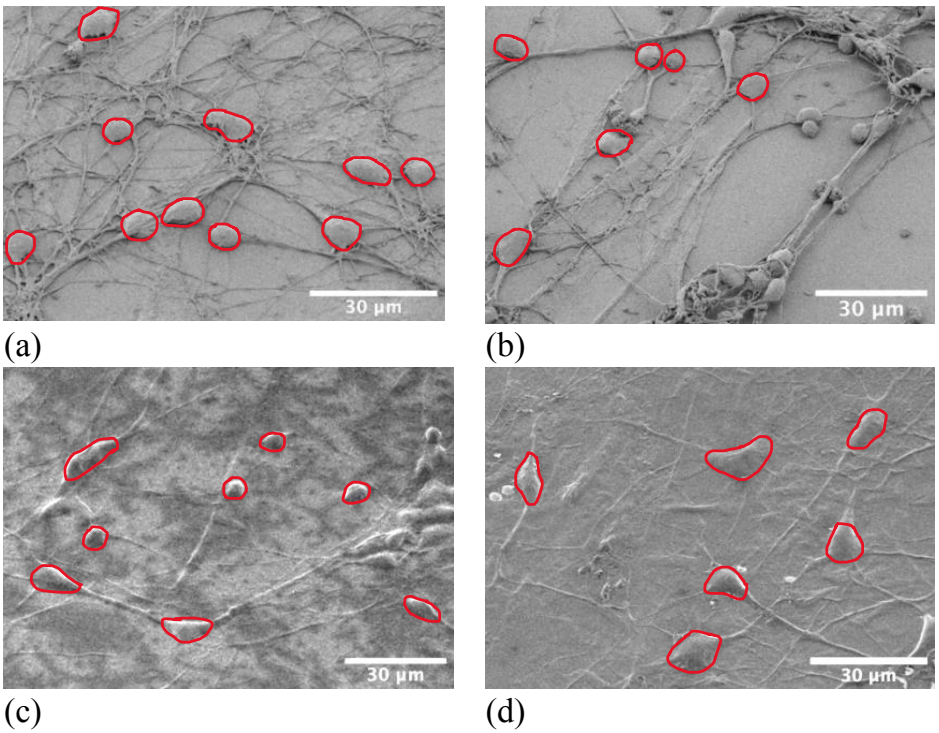

Figure 4.8: Images illustrating process of analysing shape of cells, red circles show tracing of circumference of cells. (a) and (b) show representative micrographs of cells on surfaces with an S_a of 4.7 nm, and (c) and (d) of cells on planar SU-8 control surfaces. Images are zoomed in to allow details to be concerned, full size images can be found in Appendix A.1.1. All scale bars are 30 μm.

In order to asses the morphology of the soma of neurons, the mean area of neurons was calculated. This gave the area of each neuron in as projected in 2D, and was aimed to asses to which degree the cells "spread out" on the surface, where a larger area would mean a more flattened shape, and a lower area would mean a less flattened and thus a lower area of contact with the surface. The area for neurons grown on planar surfaces was calculated to be 54 $\mu m^2 \pm 22$ μm^2, whilst mean area for neurons grown

on surfaces with an $S_a = 4.7$ nm had a mean area of 41 $\mu m^2 \pm 11$ μm^2. Furthermore, the roundness (where 1 is a perfect circle and 0 is a shape approaching 2D line) was found to be positively correlated with surface roughness, with values of 0.58 ± 0.16 for 0 nm, and 0.68 ± 0.12. This supports the qualitative observation initially done, and serves as a result in favour of the hypothesis that SU-8 nanoroughness has an effect on the morphology of neuron soma.

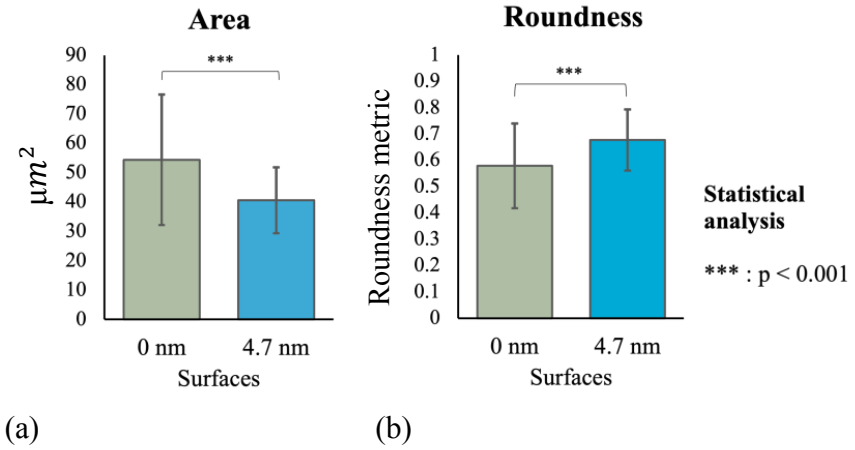

Figure 4.9: Area and roundness of neurons, as found by analysis of SEM images. A total of 66 cells from planar surfaces were measured, and 67 from surfaces with $S_a = 4.7$ nm. Area for neurons grown on planar surfaces was 54 $\mu m^2 \pm 22$ μm^2. Area for neurons grown on $S_a = 4.7$ nm surfaces had a mean area of 41 $\mu m^2 \pm 11$ μm^2. Roundness was found to be positively correlated with surface roughness, with values of 0.58 ± 0.16 for 0 nm, and 0.68 ± 0.10 (significance of difference: $p < 0.001$).

4.4 Effect of SU-8 Nanotopography on Neural Network: ICC Analysis

In this section, the results acquired from attempting to answer the question regarding the effect of nanotopography on neurite outgrowth and neural network features will be presented. To do this, ICC was performed on the cultured cells on surfaces with an $S_a = 0$ nm (glass control), 1.3 nm and 6.8 nm. Antibodies targeting beta-III-tubulin, NeuN and GFAP were used. Beta-III-tubulin is specifically located in neuron microtubules, therefore staining for neurites, NeuN is a protein localized in neuron nuclei, staining

for neuron nuclei, and GFAP is a protein only found in glial cells, staining for astrocytes. Hoechst was used to confirm presence of all cell nucleus in general. The experiments conducted focused on characterising the neurite outgrowth and neurite mesh of the neuronal cells. The underlying hypothesis was that the nanotopography would provide surface interactions that more accurately mimicked in vivo conditions, providing the growth cone with physical cues in the nanometer regime that would influence the dynamics of the neurite outgrowth in a different manner than for planar surfaces.

Specifically, neurite area per neuron was investigated, as the extent of neurite outgrowth is a process that is highly dependent on growth cone dynamics. This was quantified as the ratio between the total area of detected neurite signal (beta-III-tubulin) and the corresponding number of NeuN-stained nuclei within the respective ROI. This measure gives an estimate of the average contribution of each neuron to the neuritic mesh. It was paramount to keep all but the surface roughness parameter constant, such as staining concentrations and image settings of microscope (brightness, light, gain). The networks were imaged at the interface region, between the SU-8 growth surface, and periphery glass surface, see Figure 4.10 for visual explanation. Neurite mesh area was calculated for at least 5 random 200 mm^2 interface areas. Images were split at the interface, and each sub-image was analysed, by employing FIJI's built in Analyse tool. Representative images from all the surfaces are included in Figure 4.11. A glass surface chip was analysed in a likewise manner, to serve as a control, and ensure that any differences in network properties in the interface area was not an effect cell density in the radial direction.

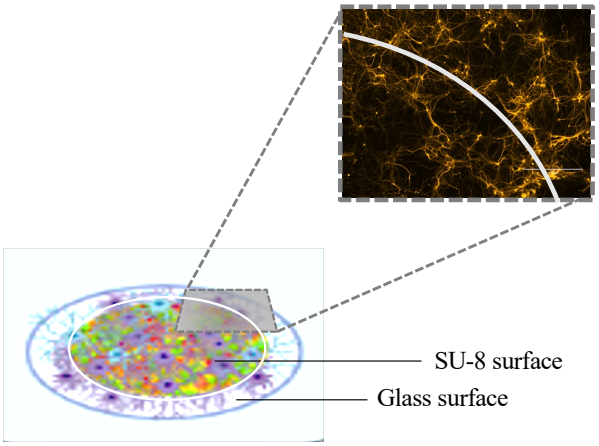

Figure 4.10: Schematic illustrating the setup for the analysis of neurite outgrowth by ICC. Neuronal cells, coloured purple and blue, are depicted growing on the nanostructured surface, which is seen underneath, as a coloured topography heat map. The SU-8 growth surface is restricted to the area inside the white circle, and the area outside the white circle is a glass surface. An example micrograph of beta-III-tubulin is shown, with dotted lines connecting to clarifying the ROI on the chip.

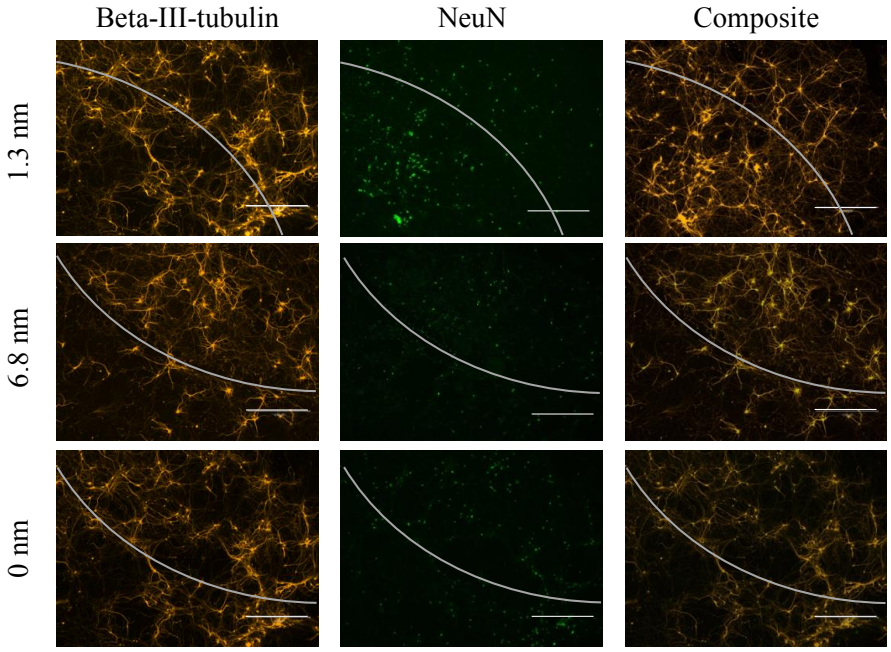

Figure 4.11: Compilation of representative images used for analysis of neurite area per neuron as a function of surface roughness. Included are signals from beta-III-tubulin (yellow) and NeuN (green), and the composite image of them both. Scale bars are all set to 1000 μm. The edge of the SU-8 surface is indicated with a grey curved line, explained in Figure 4.10, where SU-8 surface is on the inside of the curve, and glass is on the outside.

The computed values are presented in Figure 4.12, and show a tendency of the nanotopography surfaces promoting a denser network of neurites per cell, with an average value of 21 370 μm^2 ± 7200 μm^2, 31 910 μm^2 ± 6420 μm^2, 32 160 μm^2 ± 6400 μm^2 for S_a = 0 nm, 1.3 nm and 6.8 nm, respectfully.

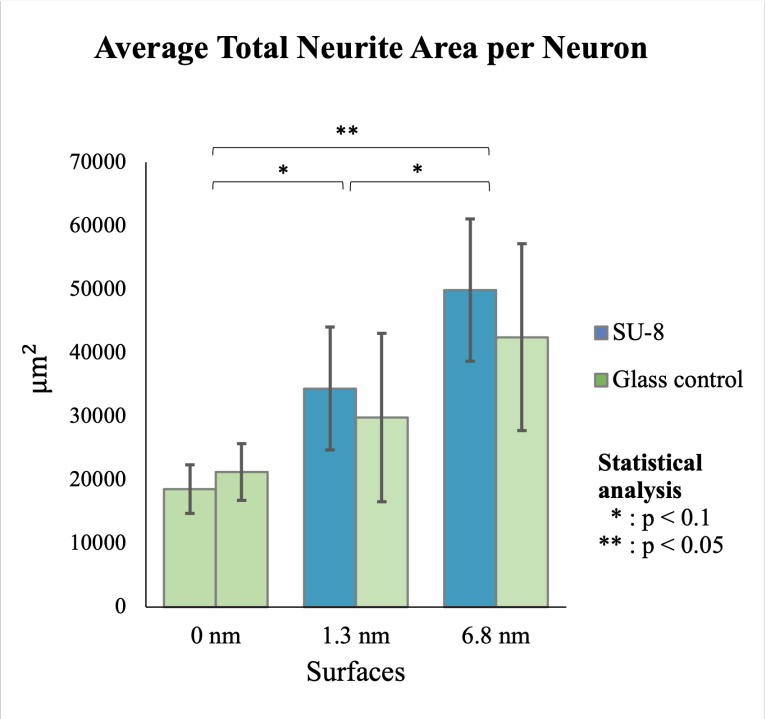

Figure 4.12: Average neurite mesh area measured by area of neurite mesh (from beta-III-tubulin signal) in ROI divided by number of neuron nucleus present (from NeuN signal) The computed values were 21 370 μm^2 $\pm$ 7200 μm^2, 31 910 μm^2 $\pm$ 6420 μm^2, 32 160 μm^2 $\pm$ 6400 μm^2 for $S_a = 0$ nm, 1.3 nm and 6.8 nm, respectfully. Statistical comparison of data across surfaces gave significant values, as indicated in the figure. Comparison of values for SU-8 surface and glass surface within chips did not give significant values ($p > 0.1$).

It should be noted that the values acquired are primarily a measure that gives insight into the relative value between the surfaces, and may not be an accurate absolute measure of the cell area. A number of other shortcomings in the method of analysis will be mentioned in Section 5.6.3.

4.5 Effect of SU-8 Nanotopography on Neural Network Topology: Simulating Neural Networks with Waxman Model

To address the effect of SU-8 nanotopography on the neural network topology, the neural networks were simulated employing the Waxman model. This served to explore the hypothesis regarding the nanotopography surface's ability to affect network topology. More precisely, by providing a growth surface that, to a further extent than planar surfaces, promotes neuron migration into assemblies characteristic of increased network topology complexity. This was expected to result in neural networks exhibiting a lower average path length, higher clustering, and ultimately, more small worlded networks.

To do this, coordinates of neurons were firstly extracted from the NeuN signal from ICC, and used as input in the Waxman model, to create artificial topological networks associated with the coordinates. Filtering and extracting the coordinates followed an automated process developed in this project, and is explained in Section 3.3.2. Four images of each surface, including approximately 300 neurons, were included. Five simulations were run for each image. A representative resulting Waxman graph for each S_a value is presented in Figure 4.13, with the input source (left), Waxman graph (middle), and the neural network depicted with beta-III-tubulin staining (right). The model parameters, α and β, were set to be 1 and 0.065, respectfully. The documentation of the process behind selecting these values is presented in Appendix A.1.2. Because of the aforementioned failure to culture the SU-8 control surfaces, these were not included in this experiment, and glass surfaces served as control.

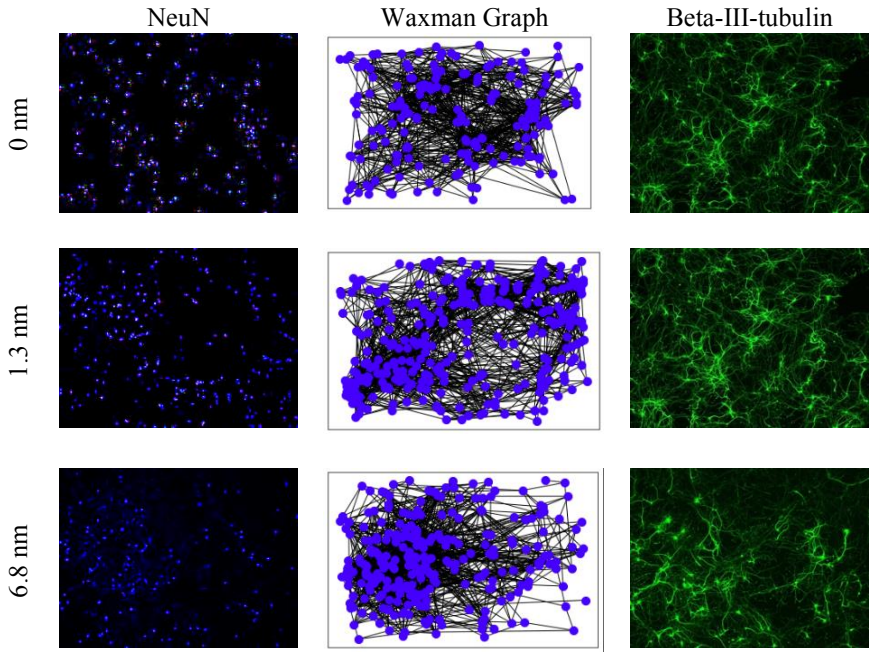

Figure 4.13: Illustration of simulated network based on a Waxman model. Input to the model is NeuN staining, as shown in the left column of images. From applying a Waxman algorithm on the coordinates extracted from the NeuN signal, the graphs shown in the middle column were acquired. The right column shows the beta-II-tubulin signal of the same ROI, expressing neurites of the neurons. Area of ROI is 200 mm^2.

In order to quantify the topology properties of these networks, the resulting graphs were analysed using network algorithms explained in Section 3.3.2, computing the values of average clustering coefficient, average shortest path length and small worldness.

The results showed a slightly higher clustering coefficient for the control surface (0 nm: 0.30 ± 0.03, 1.3 nm: 0.27 ± 0.03, 6.8 nm: 0.26 ± 0.03), while a slightly longer average shortest path length, compared to the networks from the nanostructures surfaces (0 nm: 3.26 ± 0.42, 1.3 nm: 3.07 ± 0.33, 6.8 nm: 2.85 ± 0.30), as can be seen in Figure 4.14. However, these differences were not found to be of significant difference ($p > 0.1$). The small world measure was found to be 0.10 ± 0.07 for the network grown control surfaces, and 0.11 ± 0.06 for networks grown on both $S_a =$ 1.3 nm and 6.8 nm (where 0 is given to a network with the highest degree of small world topology). Significance was not found in these differences

neither ($p > 0.1$).

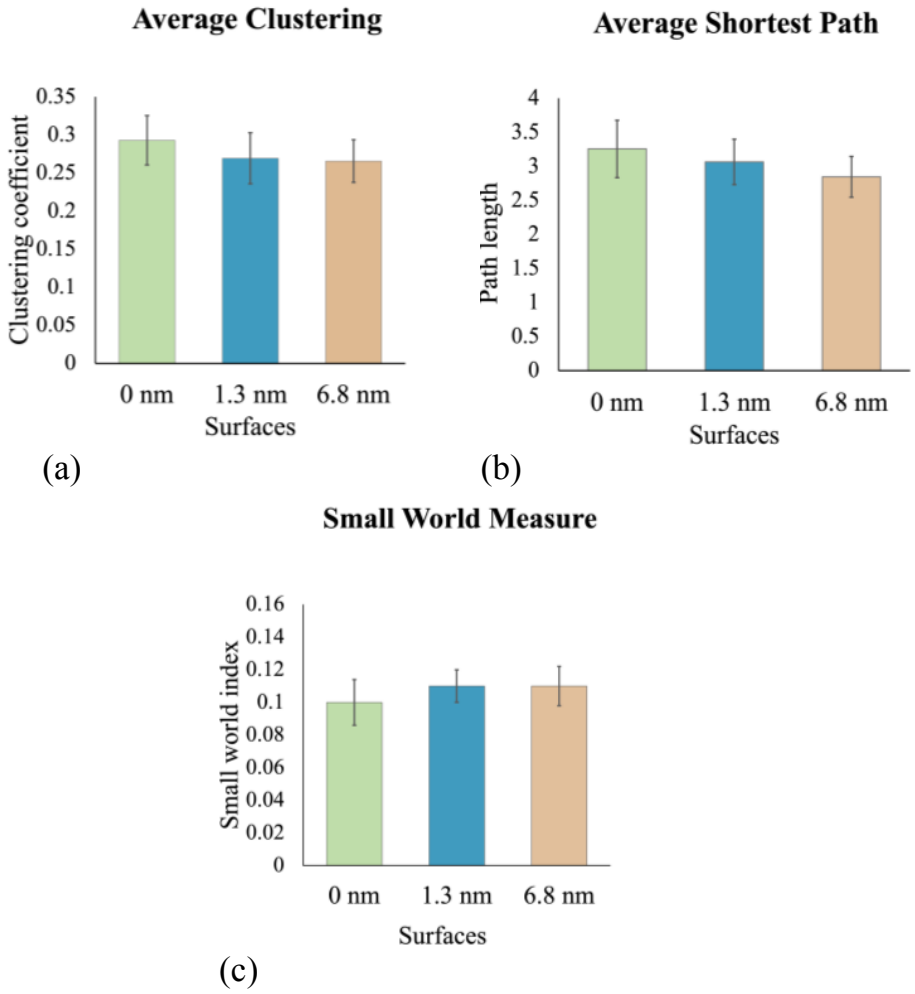

Figure 4.14: Histograms presenting results from analysis of graphs simulated with Waxman model based on NeuN staining from ICC. Data from five images of each surface was included, each containing approximately 300 neurons Five simulations were run for each image. Comparing results between groups did not yield significant differences ($p > 0.1$).

4.6 Effect of SU-8 Nanotopography on Neural Network Communication: MEA Analysis

In order to answer the research question posed regarding the effect of nanotopography on neural network communication development and efficiency, neural activity was monitored with MEAs. Neural cells were successfully seeded in two microfluidic chips with nanotopography surfaces with $S_a = 4.7$ nm, and two planar SU-8 control chips. The cell cultures were maintained for a period of three weeks [2]. Recordings were conducted every second day, from 4 DIV to 18 DIV. Employing the in-house data analysis algorithm presented in Methods and Materials Section 3.2.4, the spike firing rate, network burst rate and mean size of network bursts were attained.

Throughout the experiment, the vast majority of electrodes detected spiking activity, which served to ensure that the results were not biased by defect electrodes. Figure 4.15 includes the overview of spiking activity of all electrodes, from DIV 4 and DIV 18, for both planar and nanotopographical chips.

[2] Due to one of the nanotopography surface chips breaking off and thus rendering the chip destroyed, only one nanotopography chip was included in this experiment.

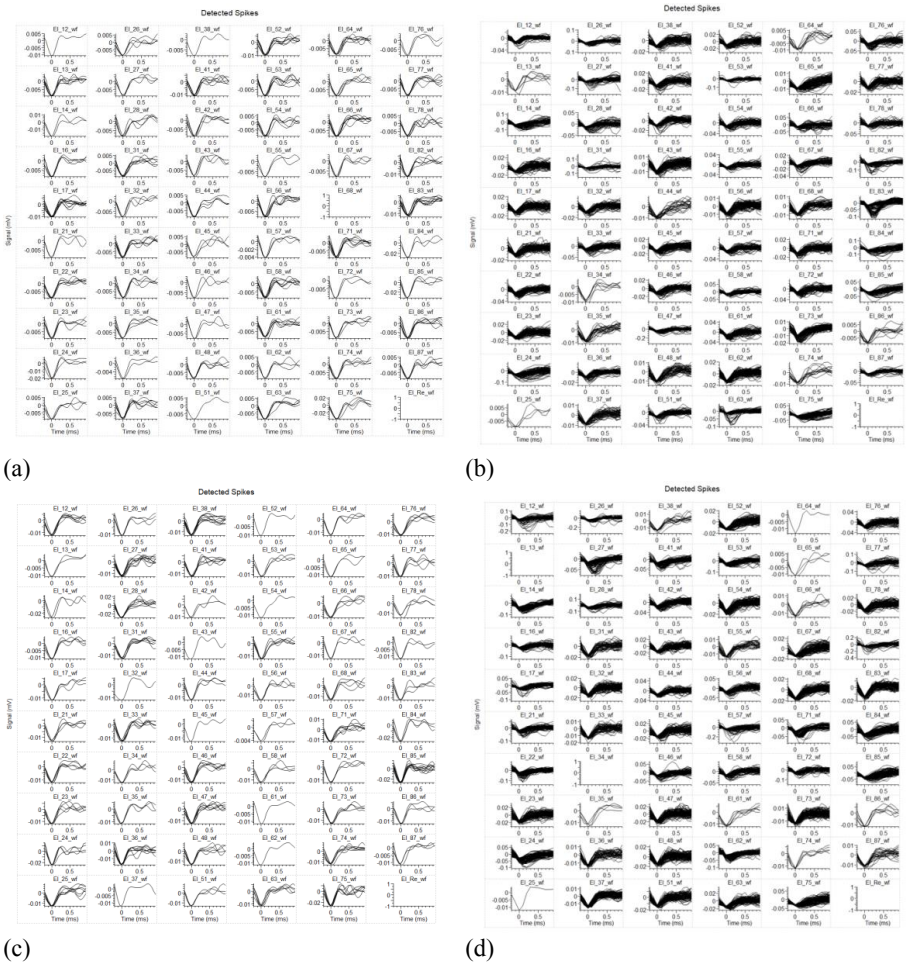

Figure 4.15: Each sub-graph within each figure contains all signals the respective electrode detected. (a) and (b) show the activity of one of the control chips, at 4 and 18 DIV, respectively. (c) and (d) show the activity of the chip with $S_a = 4.7$ nm. Y-axis are signal amplitude (mV), and x-axis are time (ms).

The chip with surface $S_a = 4.7$ nm was the first to produce spikes that exceeded the pre-defined threshold, as can be seen from Figure 4.16 (a). The flat SU-8 control chips elicited this extent of activity at a point between 12 and 14 DIV. The recordings performed during the 10 days showed sporadic, largely unsynchronized spontaneous spikes scattered among the electrodes. In general, activity for both groups increased over development, with the firing monotonically rising with increasing DIV. After 18 DIV, both groups elicit similar firing rates, 177 and 133 spikes per minute, for 0 nm and 4.7

nm S_a surfaces, respectively.

The first substantial synchronous neural network activity was detected at 11 DIV (Figure 4.16 (b)), with NB rates of 0,042 and 0,054, for 0 nm and 4.7 nm S_a chips, respectively. In the same manner as the spike rate, the NB bursting rate increased with age. However, the two groups can be seen to diverge after 14 DIV, where the nanotopography chip shows an increasingly higher number of network bursts per minute. At 18 DIV, the nanotopography chip had an average of 0.32 network bursts a minute, while the control chip had 0,18. The mean size of network bursts, measured as the average number of electrodes involved in network bursts, can be seen to also increase for both groups (Figure 4.16 (c)). Moreover, the nanotopography surface chip exhibited a considerably lower mean size of network bursts, meaning that fewer electrodes are active in network bursts. At DIV 18, the mean size of network bursts was 22.7 for $S_a = 4.7$ nm chip and 36.7 for the control chips.

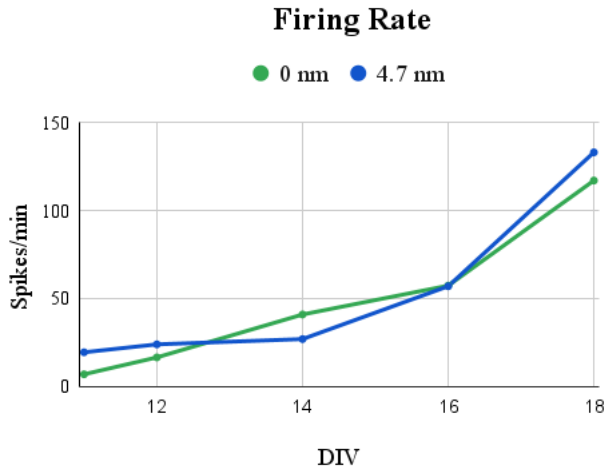

(a)

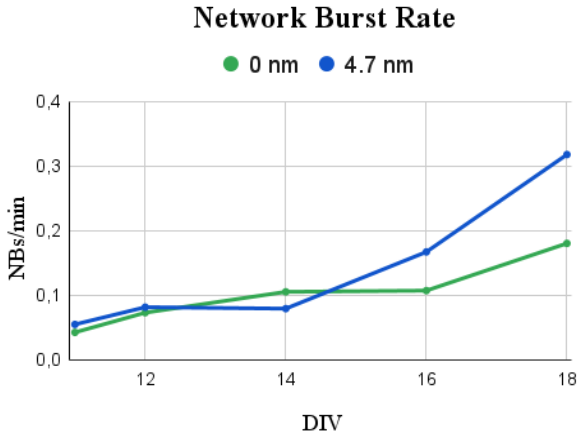

(b)

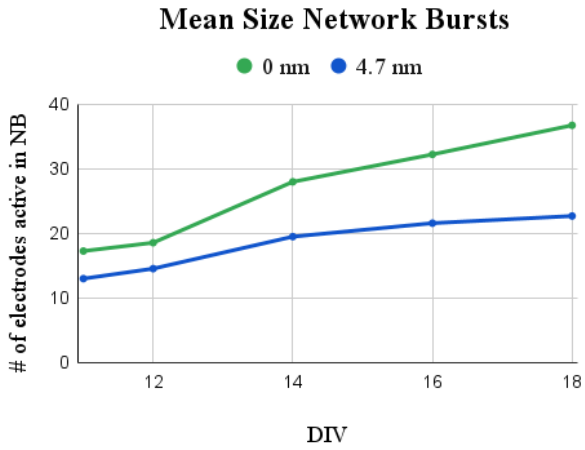

(c)

Figure 4.16: Line graphs illustrating data acquired by extracellular recording of neuronal cultures. Green lines represent SU-8 planar control group and blue lines represents the surface with an $S_a = 4.7$ nm.

4.7 Validation and Development of SEM Preparation Protocols

A secondary aim of this project was to develop and validate methods for cell analysis. This was met by development of optimised SEM preparation protocol for analysis of neuron cell cultures on nanostructured SU-8 growth surfaces cultures for analysis in SEM was developed. Herein, the main development and optimisation steps will be presented.

In preparing cell cultures for SEM imaging, there were a number of suboptimal parameters that were present in the initial attempts. These were addressed and improved upon in order to obtain high quality and resolution images. Representative SEM images acquired throughout the project can be seen in Figure 4.17. Firstly, an initial protocol using glutaraldehyde for fixating was used, according to the theory explained in Section 2.4.4. As can be seen in Figure 4.17 (a), excessive charging was an initial issue, as well as dark spots which indicated lack of coating. Different thicknesses of coating with Pt/Pd were explored, where the optimal thickness was found to be 15 nm. This balanced the problem with excessive charging on the one hand, and loss of detail on the other. A further improvement was made by tilting the sample under coating in a cyclic manner, from -45°to +45°with a period of 20 seconds. The combination of these two changes eradicated the dark spots and overcharging, resulting in micrographs with the qualities of the image in Figure 4.17 (b).

Although this was an improvement, there is a lack of details on the surface of cells, with the cell morphology having a "raisin" like appearance. This artifact was hypothesised to be caused an improper dehydration and drying process. In order to ensure that the dehydration did not cause artifacts, completely anhydrous, 100% ethanol, was used. Furthermore, three changes of 100% was done at the end of the gradient ethanol dehydration steps, instead of only one change. This was thought to ensure that all water was removed, as water present in the drying step can cause collapse of structures due to surface tensions arising in evaporation. It was furthermore confirmed that it is paramount to keep the samples emerged in fluid for all steps after fixation had started, as substrates that dehydrated prematurely were seen to exhibit clearly collapsed structures. Because of the minute volumes of liquid used in the drying steps, dehydration time steps with HMDS were decreased from 15 minutes to 5 minutes, which ensured that the sample was not exposed to air at any time. Together, these modification yielded micrographs with the qualities seen in the image in Figure

4.17 (c).

Protocol was finally applied to the last generation of surfaces, which were fabricated on MIPs. A challenge in imaging microfluidics with SEM is that the PDMS structure of the surface prohibits low working distances, as well as it blocks outgoing electrons from reaching the detector. It was therefore sought to develop a method to remove the PDMS structure after fixation and dehydration were carried out. It was discovered because SU-8 does not form covalent bonds with PDMS, as glass does (Si-O), but rather form weak van der Waals forces [73]. The PDMS structures were therefore possible to detach from the substrate, with relative ease after the dehydration steps were completed, leaving the fixated cell culture easily accessible for SEM imaging. This detachment finding was tested on chips used for electrophysiological recordings, after the 3 weeks of recording was completed. This served to confirm that the chips could be detached with a relatively low force (approximately in the same range as required to remove standard tape from a glass surface), providing an observation that MIPs mounted on SU-8 surfaces may enable SEM imaging by detachment of the MIP. Representative SEM image of one of the MIPs can be seen in Figure 4.17 (c), which illustrates the improved quality of the micrograph, in terms of absence of charging, high contrast and good visibility of surface details. The final protocol can be found presented in Methods and Materials Section 3.2.3.

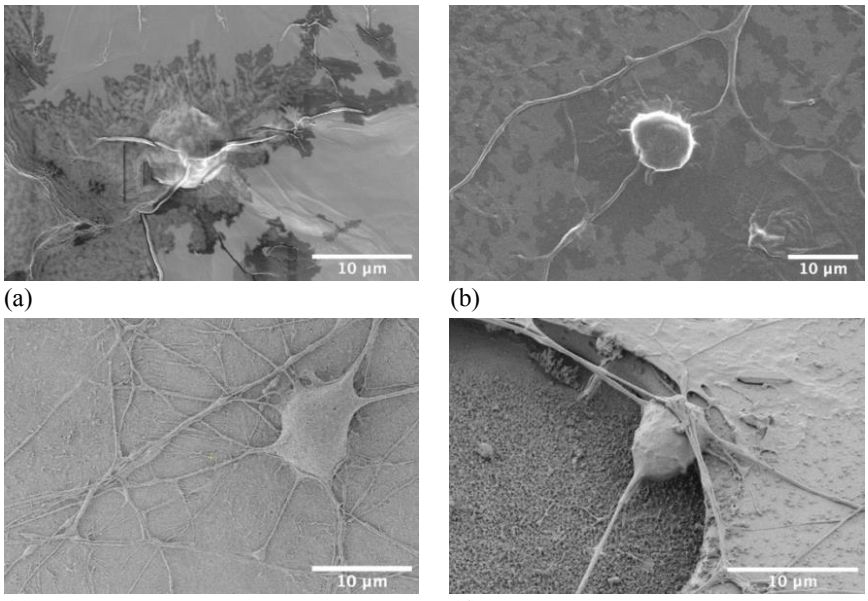

(a) (b)

(c) (d)

Figure 4.17: SEM images from different points in the development of improved preparation protocol. Image (a) is from the first round of SEM imaging, and clear defects are visible, such as charging, poor surface structure details and dark areas. Image (b) shows cell from second round of SEM imaging, where coating thickness was increased from 6 nm to 10 nm. Charging is less pronounced, but dark areas and poor surface details still persist. Increased sputter coating thickness to 15 nm, with tilting, as well as several protocol adjustments yielded images such as the one shown in (c). The above improvements were applied on cell cultures in MIPs, which gave images of the quality shown in (d). The neuron can be seen to be hanging above an electrode, held in suspension by neurites. All scale bars are 10 μm

Chapter 5

Discussion

This chapter will firstly summarize the main findings that served to answer the research questions posed in this thesis. The implications of the results will then be discussed in light of the theory presented earlier in this thesis, and existing literature. Together with this, limitations of the methods employed and the results obtained will be discussed. Lastly, some general limitations of the field of study will be discussed.

In this research, it was sought out to investigate the effects of nanostructured SU-8 growth surfaces on neuronal cell cultures, with focus on cell viability, cell morphology and neurite growth and subsequent neural network properties. It was found that cell viability was adversely affected on surfaces with S_a of 10.3 nm and above. For $S_a = 6.8$ nm and below, cell viability was not found to be significantly affected compared to planar controls. Furthermore, data collected by SEM imaging on cell morphology suggests that nanotopography surfaces with S_a of 4.7 nm promotes a more round and tridimensional morphology, compared to planar controls. Regarding neurite outgrowth, data attained by ICC demonstrated a positive correlation between increased roughness and average area of neurite outgrowth per neuron, for $S_a = 1.3$ nm an 6.8 nm. Neural network topology analysis employing an a Waxman model did not show any significant differences in topology parameters such as small worldness of the networks. Lastly, data from electrophysiology recordings indicated similar increase of firing rate by age, and while NB rate and mean size of NB increased for both $S_a = 0$ nm and $S_a = 4.7$ nm chips, divergent tendencies between the groups was observed. Most notably that the mean size of NB was found smaller in networks grown on surfaces with $S_a = 4.7$ nm.

In the following sections, discussions around these main findings will be presented.

5.1 S_a Above 6.8 nm is Associated with Necrosis

As presented in Section 4.2, surfaces with $S_a = 10.3$ nm and above were observed to cause mass necrosis, while surfaces with $S_a = 6.8$ nm and below exhibited high cell viability, insignificantly different to planar controls.

The necrotic behaviour associated with $S_a = 10.3$ nm and was speculated to be caused by the porous and sharp surface potentially inhibiting the cells from properly adhering to the surface. As adhesion is a vital requirement for neurons to survive and consequently grow and proliferate [41], this could cause the necrotic behaviour observed. This hypothesis coincides with findings from Brunetti et al.'s 2010 research, reporting that the sensing cellular machinery of neurons were not able to correctly interact with nanotopography substrates with S_a above 60 nm, leading to absence of functional focal adhesion points. The lack of organized focal adhesion points, they argued, triggers a cascade of signaling processes that produces loss of neuron polarization and activity, ultimately leading to necrosis [24]. The same observation has been noted in other papers, reporting adversely affected cell adherence on surfaces with S_a above 70 nm [69] and 204 nm [64].

In addition to this, it was also hypothesised that the low cell viability was caused by the inability of the coating protein employed, laminin, to adhere to the surface, for $S_a = 10.3$ nm and above. One of the primary functions of laminin coating in vitro is to facilitate attachment. Thus, by the same token as argued with above, a loss sufficient surface coverage could lead to an inability for cells to adhere to the substrate, and ultimately lead cell death. This furthermore corroborates with Lord et al.'s (2010) finding that a necrotic cell response on nanorough surfaces may be explained by the surfaces properties influencing the adsorption of cell adhesive serum proteins, in terms of composition or correct folding of the adsorbed protein layers [42].

Lastly, it can also be speculated that the observed cell death on the roughest surfaces could have been caused direct physical damage to the neuronal cells, due to the the sharp and protruding topography. This speculation is strengthened by inspection of the SEM images in Figure 4.1 (e), showing

a $S_a = 150$ nm surface, where elongated sharp and porous structures can be seen. The sharp features could potentially puncture the cell membrane, causing the cytoplasm to spill out and lead to cell death [106].

Contradictions To Previous Studies

These current findings are contradictory to previous reports on two counts. Firstly, a much lower upper limit to roughness was found in the current study, $S_a = 6.8$ nm, than in previous studies, $S_a = 60$ nm [24], 70 nm [69] and 204 nm [64]. Secondly, previous research also reports a lower limit for roughness, at $S_a = 1.3$ nm [70] and 20 nm [64], which was not found in this study. Two further hypotheses were formulated in an attempt to explain each of these incoherent findings.

The reason for the significantly lower upper limit to surface roughness found in this study was hypothesised to be due to a positive correlation between the accumulation of antimony contamination on the surface, and the etching time used to structure the surface. As as discussed in Section 2.3, antimony is thought to be the source of the roughening effect from plasma etching SU-8. An unwanted accumulation of antimony could thus be a side effect of the fabrication process, which increases for increased roughness. Furthermore, antimony has been reported to have a cytotoxic effect at high concentrations [72]. Taken together, this could be thought to be the source of the disparity in the upper limit of surface roughness, compared to previous research.

Contrary to previous research, no lower limit to cell viability was found for nanostructured surfaces in this study (that were plasma cleaned [1]). However, low cell viability was indeed observed for the planar SU-8 surfaces not treated with plasma cleaning, as can be seen in Figure 4.2 (b). The increase in surface hydrophilicity caused by plasma cleaning was thought to circumvent the low cell viability. This hypothesis is in line with previous reports stating that low surface hydrophilicity can be detrimental to biocompatability [107, 108]. In Isdal's thesis, it was found that non-treated planar SU-8 had a considerably lower hydrophilicity than plasma cleaning the surfaces, above the limit for biocompatability noted in previous studies. Therefore, the attribution of poor cell viability to the low hydrophilicity of non-etched SU-8 seems warranted. The full results regarding hydrophilicity of surfaces are presented in Isdal's thesis [73]. This furthermore corroborates with the speculations of Khan et al. (2005), who hypothesised that the lower limit

[1] It is important to note that plasma cleaning of the surfaces was introduced after the first round of experiments. Thus, only the first batch of surfaces were cultured without prior plasma cleaning.

of cell viability could be due to decrease in hydrophilicity for surfaces with low nanometer regime roughnesses [64].

Further investigation of two hypothesised reasons for low cell viability was not conducted, as the focus was directed at exploring S_a values that promoted high cell viability. This limitation of focus was necessary to ensure completion of the project within the time restraints set. However, in order to fully elucidate the effect of nanotopography on cell viability, further investigation into the effect of nanotopgraphy on laminin's ability to adhere to the surface and cytotoxic effect of antimony accumulation should be conducted.

5.2 Nanotopography May Promote More Tridimensional Soma Morphology

Analysis of SEM images revealed an effect of nanotopography on neuron soma morphology. The flat morphology of cells observed on the control surfaces is in line with the expected behaviour based previous research, which validates one of the premises of this research, cells grown on planar surfaces exhibit a changed morphology compared that of cells in vivo [109].

From quantitative analysis, a decrease in flatness, and an increase in roundness was seen for the neuron soma for neurons grown on surfaces with an $S_a = 4.7$ nm. The data suggests that the surface roughness promotes a cellular morphology that is more tridemensional, with a smaller contact area with the substrate than for planar surfaces. An investigation into the mechanism of this behaviour was beyond the capabilities of the analysis methods employed in this research. However, it can be speculated that the nanotopograhic surface induced a change in adhesion points between the cell and the substrate. This is in line several other findings where it has been found that nanotopographical surfaces influence the formation of focal adhesions and thus cell adherence, causing a stronger cellular adhesion due to an increase in potential adhesion sites for the cell, ultimately altering the cytoskeletal tension which impacts the cell's 3D morphology [110].

It must be clearly noted that the increased cellular roundness and less flat and polarised neuron soma geometry might be one indication that the cells adhere more in a 3D like manner when placed on nanostructured SU-8 growth surfaces, but due to the immense complexity of cell-substrate interactions, others factors might also contribute to this observation.

5.3 Average Neurite Size is Correlated With S_a

Based on the results presented in 4.4, it can be inferred that nanostructured SU-8 surfaces may have a supportive effect on increasing neurite growth compared with planar surfaces. This is in line with several previous in vitro studies that have reported an increase in neurite outgrowth and subsequent neurite mesh [62, 111]. An hypothesis for the increased neurite outgrowth on topography surfaces was postulated by Spedden et al. (2014), arguing that the topography served as anchoring points for the growth cone, providing an asymmetric torque force. This ties into the theory discussed in Section 2.1.1, and illustrated in Figure 2.5. This was further explained to be driven by the filopodium of the growth cone, having the ability to wrap over sharp protruding nanoscale features, providing an increase in forces produced, relative to more shallow angled features and planar surfaces [112]. It can be further speculated that the increased neurite outgrowth can be explained by the findings of Dalby et al. 2004, reporting that cells cultured on 10 nm topography islands produced an increase in number of filopodia [23]. This suggests that, on nanotopography surfaces, more filopodia are probing and locating nanofeatures in the vicinity of the growth cone, and thus directing the neurite outgrowth. An important note has to be made regarding difference in neurite area between glass and nanostructured SU-8 within the same chips. Although a strong statistical significance was not found, there are still tendencies which allow for speculative arguments to be made.

These finding may be important in questions regarding improved neurite regeneration, outgrowth and promoting more a healthy neuronal architecture, as the ability of neuronal cells to project membrane extensions from their cell bodies is closely linked to their function and cell health [113]. However, it should be noted that the increased neurite mesh could be a sign of increased efficient in neurite outgrowth, but it could also be a symptom of less advantageous network behaviours, such as less specification of neurite outgrowth.

5.4 No Significant Network Topology Effects Observed From In Silico Modelling

The analysis of the Waxman graphs constructed of the neural networks revealed minute differences in the effect of nanotopography on average path

length, clustering coefficient. Although the small world index did show a high degree of small worledness for the networks cultured on nanostructured surfaces, the index score for the control surface was even lower, although not significantly. The underlying hypothesis in this study was that nanotopography would serve as a quasi-biomimetic microenvironment for the cells, and as shown in previous literature for comparable surfaces, promote increased mobility dynamics and thus provide an assembly of neuron cells that increased the complexity of the network topology. From this, it was expected that modelling the network with the Waxman model would reveal a more efficient topology, with a lower average path, higher clustering and thus small worldness for the topography surfaces, compared to planar surfaces.

The approach of modelling in vitro grown neural networks in silico, based on ICC acquuired neuron nuclei coordinates, closely relates to the work of Onesto et al. (2017), who employed roughened silicon substrates to attempt to promote assembly networks with a small world topology. In contrast to the current findings, Onesto et al. concluded in their study that cells on cultured in surfaces $S_a > 22nm$ exhibited small world attributes. However, they also noted that cells on surfaces with $S_a < 10nm$ exhibited a more uniformly distributed network without altered significantly affected network topologies. Thus, it can be argued that the absence of significant topology effects in this study could be due to the nanostructures being of insufficient size to promote neural migration to the extent that it influences network topology. In light of the theory discussed in Section 2.1.1 and inspection of the SEM images included in Figure 4.1 (b)-(c), this argument is further underscored. It is evident that surfaces with $S_a = 1.3$ nm exhibits only mildly protruding structures, and surfaces with $S_a = 6.8$ nm exhibits a sparse distribution of grain-looking structures, which, may not provide sufficiently increased attachment dynamics to induce observable network topology effects.

Model Parameter Selection

The selection of model parameters, α and β, was based on a qualitative argument by comparison of resulting networks from different model parameters with the actual neural network as imaged by ICC (beta-III-tubulin), see Appendix A.1.2. β was set to 0.065, and α was set to 1. From these values, it could be inferred that two nodes separated by 290 μm would have a 50% probability of being connected. Although this verification method can be criticized for being weakly based, it can be argued that, since parameters were set to the same value for all simulations, a potential sub-optimal

parameter choice would affect the networks in a similar manner, not affecting the viability of comparing data across substrate topographies.

5.5 Increased Network Communication Efficiency Associated With Nanotopography

The present results describes the development of network activity on nanotopography, from the first 18 DIV. The results demonstrated a rapid increase of spiking, bursting and network spiking activity over this period of time, where first significant spike detection was after 4 DIV. The time scale of the development coincides with previous research employing nominal planar surfaces, where it is generally found that activity begins to appear between DIV 2 and 6, and starts to increase rapidly between DIV 6 and 13 [114–116].

The firing rate of the two groups followed a similar increase over time, indicating a similar progression of the maturation of the network. At the last recording, it was seen that the firing rate was nearly indifferent between the two surfaces, indicating that health and stability of the networks were comparable, and that the maturation of the networks had reached the same maturity. Regarding the bursting dynamics, interesting insights have been observed through the analysis of the spontaneous network-wide bursting activity. It was evident that the NB rate for nanotopography surfaces was considerably higher than that of the control group, which indicates that the network engages in synchronized events more frequently. Furthermore, when network bursts did occur in the networks, it was found that the mean size of NBs was lower for nanotopography chips, which means that fewer electrodes were involved in each NB. Taken together, this indicates that surfaces with $S_a = 4.7$ nm promoted higher levels of synchronised neural network activity, that at the same time was more localized and segregated, compared to the control chips.

As discussed in Theory Section 2.4.6, the emergence of network bursts are associated with more complex information propagation and network-wide communication. The localization of network activity furthermore coincides with the hallmarks of network small worldness and efficient communication found in the brain (discussed in Section 2.1.2). As argued in the research conducted by Valderhaug et al. (2019), simple forms of emergent localized network bursting behaviour may reflect basic emergent phenomena of information segregation seen in the brain [38]. Although these elec-

trophysiological network traits are also present in the control group, and are seen in planar surface neural network studies in general [117], an increase in the degree of localisation may be indicative of an increase in the pertinence of the neural network behaviour in vivo.

Viewing these results in the light of the morphology analysis conducted based on SEM images of the cell cultures (Figure 4.9), the increase of NB rate and localization of network activity may be influenced by the increase of tridimensional structure of the neurons. As discussed in Results, a planar morphology limits many functions to the 2D plane, such as neurite outgrowth. It can be argued that a slight increase in tridimensional morphology has the capacity to overcome some of the reductionistic limitations, and thus promote more complex network interactions and communication. Combining the electrophysiology results with the increased neurite area finding, may indicate that the promotion of increased neurite area indeed is connected to the development of neural networks with increased communication efficiency. However, it must be noted that this is a speculative correlation argument, and must be investigated further in order to draw conclusions.

In relation to the insignificance effect on network topology as measured by the Waxman model, one would expect that a similar insignificant results would be found in this electrophysiology analysis. However, due to the limitations of the network topology analysis (which will be discussed in the next section), it may be that an underlying behaviour is not accurately detected. Or, by the same token, since the electrophysiology results consisted of only one sample, these results may due to statistical variations.

5.6 Limitations of Results

Throughout this project, several instruments and techniques have been taken in use in an attempt to answer the research questions posed. Although optimised protocols and measurements for statistical rigidity was taken, several limitations of the results were still present. This section will look at each of the analysis methods employed in this research, and discuss the main limitation imposed on this research.

5.6.1 Limitations of AFM as Roughness Measurement Method

Although measurement of the roughness of the nanotopography surfaces was not conducted by the author, a short discussion on its shortcomings must be included. Further discussion is presented in Leik Isdal's manuscript [73].

AFM was used as the instrument to characterize the nanoroughness of the surfaces. However, since the roughness parameter used, S_a, reduce all the information in a profile to the deviations from a mean line, they may be insensitive to grossly different spatial and height symmetry features of profiles [39]. This is particularly relevant for the surfaces with S_a above 75 nm. From looking at Figure 4.1 (b) (FIX THIS), it can be clearly seen that the structures are on the magnitude of the scale bar in the image, which is 1000 nm. This strongly indicates that the AFM measurement does not measure the roughness in a manner that is representative, but instead measures only the top region of the structures. To overcome this shortcoming of AFM to characterise nanotopography surfaces, the S_a could be accompanied with another metric, which elucidates dimensions that AFM does not capture. For example, in previous studies, supplementary metrics such as fractal dimension are also often included, which captures surface features by quantifying their complexity as a ratio of the change in detail to the change in scale [39].

5.6.2 Limitations of SEM Analysis

Even with an optimised protocol, preparation of the cell cultures for SEM is prone to variability between experiments, and also within experiments. SEM images used in this research were from two different generations of surfaces, for which the fixation and dehydration process was not of identical nature. An unsuccessful fixation and dehydration process can potentially destroy the morphology of cells, which renders the validity of morphological studies limited. However, for the preparation of the cells images included in this thesis, it is argued that the success of the preparation process is of sufficient quality. For example, edges of the cells are clearly distinguishable in all images included for the analysis, which is the most important feature for determining the shape of the cells.

Another limitation in the analysis of cells from SEM images in this research was that the process sputter coating (15 nm Pt/Pd) effectively covered the nanotopgraphy surface (S_a below 10.3 nm). This made investigation of

neuronal cells interactions with the SU-8 growth surfaces limited to including shapes and features above 15 nm.

5.6.3 Limitations of ICC and Epiflourescent Imaging

Several experiments in this project was dependent on data extracted from epifluorescent imaging of cells stained according to ICC protocol. Although strict measures were taken to ensure constant settings throughout the imaging process, it is generally considered that using intensity of signal is prone to substantial variability. For example, the different S_a of the surfaces used in this study may have had a different impact on the light used in the microscope, where especially comparing SU-8 surfaces to glass surfaces may impose a bias as more light permitted through glass substrates. Furthermore, a generic weakness using secondary antibodies, is that a single cell can be stained multiple times, thereby affecting the signal intensity between samples.

For the analysis dependent on detection of NeuN signal, the sharpness of the signal sets a limitation to how precisely overlapping nucleus signals can be discerned. This limitation extends into the processing of the signal, where it is challenging to precisely segment individual cells in clusters from each other. The presence of this limitation is apparent when comparing cell cultures imaged with SEM (Figure 4.9 (b)); it can be seen that neuron clusters contain several cells. The individual cells in such clusters are systematically not accounted for when analysing ICC attained images, failing to completely segment clustered cells into the individual constituents. In the current research, this limitation is probable to have skewed the results of average neurite size in the direction of unrealistically large values. However, the validity of the results is conserved if it is assumed that this limitation does not correlate positively with increased S_a, which if was the case, would more often under-count individual cells in clusters and thus result in a larger average neurite area per cell for nanotopography chips. In order to overcome this limitation, improved methods for segmentation of cells from NeuN signal needs to be developed.

5.6.4 Limitations of Waxman Model for Network Topology Analysis

The Waxman model is subject to the same abovementioned bias caused by the challenge of correctly extracting and segmenting positions of neurons from ICC NeuN signals. Under-counting individual cells in clusters would have a direct impact on features such as clustering coefficient, which could have a detrimental impact on the viability of the results obtained. This caveat could furthermore weaken the results if the under-representation of clusters was correlated with increased surface roughness. Additionally, it should be mentioned that neurons can cluster together for other reasons than assembly into efficient network topologies. However, as cell viability was found to be indifferent between topographies with S_a below 6.8 nm, an assumption was made that clustering was an effect of healthy cell behaviour.

Model parameters were determined based on a qualitative inspection between the resulting Waxman graph and the beta-III-tubulin image of the same network. Although the parameters were kept constant, it may be that the parameters used did not optimally express the differences. For example, if parameters are set too high, networks have a very edge high density independent of differences in input, and metrics such as average path length and thus small worldness converges to a similar value for similar inputs. To overcome this, a further investigation into the effects of model parameter choice should be conducted. This can be done by systematically mapping the effect of parameter values on the topology metrics, to determine the robustness of change in model parameters.

Furthermore, a generic limitation of the Waxman model lies in the assumption of exponential decrease in the probability of two nodes connecting, as distance increases. Because of this, the probability of long range connections quickly becomes increasingly minute. This has the effect of underrepresenting long range connections in the simulated network, compared to neural networks in vivo. Long range connections between clusters, is one of the hallmarks of small world networks, and is a feature that is poorly recapitulated in the Waxman model.

5.6.5 Limitations of MEA for Network Analysis

Electrophysiological recordings in this study was limited to 18 DIV, which is generally regarded as the initial stage of development for in vitro cultures. Development beyond DIV 18 was not studied in the current study, due to time limitations, and it can therefore not be ruled out that features examined may continue to mature with additional time in culture.

5.7 Statistical Significance

Because of the nature of this project, concerning the extensiveness of the fabrication method, and time consuming aspect of cell culturing and analysis preparation, the number of data points of some experiments suffered from being too low. This means that the p-values, computed by Mann-Whitney U test, were not significant in many cases, and renders parts of this research limited to being indicative of actual behaviours. This was especially the case with electrophysiology recordings. Due to loss of two of three nanotopography growth surface chips, the recording from only one nanotopography chip and two planar SU-8 controls was acquired. This limits the results to indications and the discussion to speculations. Additionally, for the analysis employing ICC, loss of planar SU-8 control group, prevented systematic control of the biochemical and biophysical design parameters. However, glass surfaces were used as control groups. Based on the facts that SU-8 is considered a highly bio-compatible surface with negligible chemical impacts, glass surfaces can be argued to have a large overlap properties, and served as a viable control group.

In order to provide answers to the research questions with more statistical significance, studies must be conducted with several more surfaces per nanotopography value, to acquire more images and thus more data points.

5.8 Limitations of Inter-Study Comparison

It is important to note that the diverging results found in the existing literature, and also comparing the results of this study with previous literature findings, might be explained by an omnipresent challenge in this area of scientific research. Essentially, this is the challenge of comparing results

across studies, when the independent conditions of the experimental settings are not identical. In an ideal scientific experiment, all independent variable are known and controllable, and the dependent variable (the one that is being investigated) changes in an observable manner in response to the independent variables. However, in the field of neuronal networks cultured on advanced growth surfaces, this is often not the case, and ensuring that the independent variables are kept constant can be an exercise in futility. For one, variables such as average roughness are difficult to precisely reproduce, and the metric of which they are measured (S_a with AFM in this study) can be at worst unreliable and subject to grave biases, as argued for being the case for surfaces with $S_a = 150$ nm in this study. Secondly, the experimental setup varies greatly between research, with a wide range of different materials and cell types employed. Moreover, neuron-substrate interactions vary across neuronal cell origin, feature dimension and feature geometry of the nanotopography, and even when cells, materials and topography designs are attempted to be the same, the nature of experimental variability makes it difficult to reproduce findings. These challenge underscores the necessity to develop standardized research platforms, so that research groups can join forces, and together systematically investigate advancements of in vitro neural network platforms.

Chapter 6

Conclusion

The main aim of this project was to study the effects of nanostructured SU-8 growth surfaces on neurons and neural networks in vitro. This aim was further broken down into four research questions. Can nanostructured SU-8 growth surfaces:

- Contribute to improved neuronal cell viability?
- Influence neuronal morphology?
- Affect neural network topology?
- Contribute to increased neural network communication efficiency?

The underlying hypothesis was that such surfaces would act as a quasi-biomimetic environment, providing nanostructures that promote cell behaviour more closely mimicking that of neuronal behaviour in vivo, compared to planar controls.

In order to acquire high quality data used to answer these research questions, protocols for preparation for SEM imaging and ICC were firstly verified and further optimised, and a Waxman algorithm was developed to computationally analyse images acquired from ICC. Then, an array of nanostructured SU-8 growth surfaces, with roughnesses ranging from $S_a = 0$-150 nm, were fabricated by Leik Isdal, and seeded with neuronal cell cultures. The surfaces were seeded with rat cortical neurons and astrocytes and screened with respect to cell viability. Then, ICC was employed to investigate neurite outgrowth as a response to nanotopography. ICC images were furthermore used in combination with the Waxman model, which sought to answer the research question regarding network topology. The optimised SEM protocol was applied to acquire high magnification images

of neuronal cultures grown on planar and nanostructures SU-8, to study influences on neuron morphology. Lastly, nanostructured SU-8 growth surfaces were implemented into microfluidic chips, integrated with microelectrode arrays, to conduct electrophysiological recordings of cultured neural networks, to answer the research question regarding the effects of nanostructured SU-8 growth surfaces on neural network development and computational efficiency.

Answering the research questions posed, the results in this thesis showed that:

- Surfaces with an S_a below 6.8 nm provided cell viability in line with planar controls, while surfaces with an S_a above 10.3 nm were associated with low cell viability. This reinforces the findings of previous literature that there is an upper limit to nanoroughness with regard to cell viability. However, the limit was found to be substantially lower in the current work compared to previous literature. Further investigations are needed to elucidate the root cause of this.
- Nanostructured SU-8 growth surfaces may promote a more tridimensional neuronal soma morphology on surfaces with $S_a = 4.7$ nm. This was hypothesised to be due to increase in potential adhesion sites for the cell, ultimately impacting the tridimensional morphology.
- Nanostructured SU-8 growth surfaces increased total neurite area per neuron, which was thought to be due to nanotopography structures providing an increase in structures for filiopodia interaction and anchorage, influencing growth cone dynamics and thus neurite outgrowth.
- Nanostructured SU-8 growth surfaces with $S_a = 1.3$ and 6.8 nm did not significantly affect neural network topology features compared to planar surfaces. However, compared to previous research, this may have been due to insufficient surface roughness in promoting neuron migration to an extent which affected neural network topology. It was also thought to be due to limitations of the analysis.
- Nanostructured SU-8 growth surface with an $S_a = 4.7$ nm may promote more computationally efficient neural networks than for planar controls, detected as more localized network bursts in electrophysiological recordings. This difference was speculated to arise due to the differential behaviours found in cell morphology and neurite features, acting together to contribute to increased communication network efficiency, more pertinent to network dynamics seen in the brain.

In conclusion, this study demonstrated that nanostructured SU-8 provides cell viable growth surfaces that have the capacity to influence aspects of neuronal cell behaviour from the individual neuron to the entire neural network, compared to planar controls. Although cation is taken in not concluding that results are definite examples of more relevant behaviour, indications of nanostructured SU-8 promoting behaviours more similar to that found in vivo have been argued for. Additionally, proof-of-concept of a novel microfluidic platform with a nanostructured SU-8 growth surface and integrated microelectrode arrays was shown. This platform permits for continual monitoring during culturing with common optical microscope techniques, as well as advanced electrophysiological recordings. Further advancements of this platform can provide a powerful tool for in vitro study of biological neural network communication and computation, with increased clinical relevance and experimental control.

Chapter 7

Further Directions

Even though research employing reductionistic in vitro models has seen great advancements in recent years, there is still a long way to go before models can accurately recapitulate behaviour seen in vivo. For this to become a reality, further advancements are needed. In more immediate terms, several further improvements and future studies have been recommended in the current study, and some of them will be briefly expanded upon here.

Cell viability was found to be limited to a much lower roughness than in previous studies. A number of hypotheses were postulated in order to explain this, but due to time limitations, were not further investigated. Firstly, it was questioned whether coating using PLO and laminin was negatively impacted by increasing topography. This would mean that a more rough surface would prevent cell adhesion, and ultimately lead to the observed necrosis, not intrinsically due to the roughness, but due to a lack of adhesion sites for the cells. Secondly, it was hypothesised that the observed necrosis could be due cytotoxic levels of antimony accumulation produced in the etching process of SU-8. In the same way as laminin coating may have been negatively impacted by nanotopography, accumulation of antimony may have been positively correlated with etching time, and thus roughness. To further elucidate the exact relationship between these unmeasured sources of uncertainty, a systematic study should be conducted. The extent of laminin coating could be analysed utilizing ICC techniques, using anti-laminin antibodies. For the antimony pollution hypothesis, efforts should be directed at investigating the exact levels of accumulated antimony, as a function of surface roughness. This can be conducted with energy-dispersive X-ray spectroscopy, which is a technique that allows for

elemental analysis or chemical characterization of a sample [118]. If it is found that one of these factors were the root cause of low cell viability, new investigations into surfaces with an S_a above 6.8 nm could be conducted, employing the same analysis framework as developed and employed in the current thesis.

As noted in Section 2.1.1, neurons can sense a myriad of surface features, such as height and lateral spacing of nanoscale features, elasticity and aspect ratio of features. The current method of etching surface roughness is restricted to a stochastic roughening process, making it difficult to precisely tune the surface with regards to the abovementioned features. In future studies employing nanostructured SU-8 as growth surfaces, investigation into surface structuring using electron beam lithography could be done, optimisation of this process could allow for fabrication of surface features with details in the low nanometer regime [119]. This would allow for controlled exploration of more surface topography dimensions than roughness, such as fabricating nanopillars with controlled height, pitch and width.

For future investigations of nanostructured SU-8, the weakness of only employing AFM to characterize the nanotopography could be improved upon. To provide a more precise characterisation, other metrics, such as fractal dimension, could be utilized, to capture more information about the properties of the surface.

In broader terms, with the proof of concept of implementing nanostructured SU-8 growth surfaces into microfluidics, it is of interest to extend the two-chambered microfluidic devices to multi-chambered microfluidic devices combined with MEA. This would allow for mimicking of the compartmentalized hierarchically structure found in the CNS, and at the same time transferring the effect of nanotopography on cell behaviour found in this study, while allowing for extracellular recording of the neural network. This approach can furthermore serve as a platform to enable advanced modelling of hierarchical neural networks for study of healthy and perturbed neural networks, and the mechanisms behind the shortcomings of CNS injury rehabilitation.

Bibliography

[1] V. L. Feigin *et al.*, 'Global, regional, and national burden of neurological disorders, 1990–2016: A systematic analysis for the global burden of disease study 2016,' *The Lancet Neurology*, vol. 18, 5 May 2019, ISSN: 14744422. DOI: 10.1016/S1474-4422(18)30499-X.

[2] B. Morrison *et al.*, 'In vitro models of traumatic brain injury,' *Annual Rev Biomedical Engineering*, 2011. DOI: 10.1146/annurev-bioeng-071910-124706.

[3] J. Seok *et al.*, 'Genomic responses in mouse models poorly mimic human inflammatory diseases,' *Proceedings of the National Academy of Sciences of the United States of America*, vol. 110, pp. 3507–3512, 9 Feb. 2013, ISSN: 00278424. DOI: 10.1073/pnas.1222878110. [Online]. Available: www.pnas.org/cgi/doi/10.1073/pnas.1222878110.

[4] K. Heiney *et al.*, *Criticality, connectivity, and neural disorder: A multifaceted approach to neural computation*, Feb. 2021. DOI: 10.3389/fncom.2021.611183. [Online]. Available: www.frontiersin.org.

[5] J. Bickle, P. Mandik and A. Landreth, 'The philosophy of neuroscience,' *The Stanford Encyclopedia of Philosophy*, 2019.

[6] D. Purves *et al.*, *Neuroscience in the 21st Century*. Sinauer Associates, 2012, vol. 5, ch. 5, 8, 22, 2, 4.

[7] A. Hodgkin, 'The ionic basis of electrical activity in nerve and muscle,' *Biol. Rev.*, 1951. DOI: 10.1111/j.1469-185X.1951.tb01204.x..

[8] H. Asdf and K. Rsdf, 'Active transport of cations in giant axons from sepia and loligo,' *J. Physiol*, 1955. DOI: 10.1113/jphysiol.1955.sp005290.

[9] R. Phillips, J. Kondev and J. Theriot, *Physical biology of the cell*. 2013.

[10] J. Hardin, G. Bertoni and L. Kleinsmith, *Becker's World of the Cell*. 2003.

[11] M. Rahimi-Balaei *et al.*, *Neuronal migration during development of the cerebellum*, Dec. 2018. DOI: 10.3389/fncel.2018.00484. [Online]. Available: www.frontiersin.org.

[12] E. A. Vitriol and J. Q. Zheng, *Growth cone travel in space and time: The cellular ensemble of cytoskeleton, adhesion, and membrane*, Mar. 2012. DOI: 10.1016/j.neuron.2012.03.005. [Online]. Available: https://pubmed.ncbi.nlm.nih.gov/22445336/.

[13] M. Rashid *et al.*, 'Neural-specific deletion of the focal adhesion adaptor protein paxillin slows migration speed and delays cortical layer formation,' *Development (Cambridge)*, vol. 144, pp. 4002–4014, 21 Nov. 2017, ISSN: 14779129. DOI: 10.1242/dev.147934. [Online]. Available: /pmc/articles/PMC5702069/%20/pmc/articles/PMC5702069/?report=abstract%20https://www.ncbi.nlm.nih.gov/pmc/articles/PMC5702069/.

[14] G. Marchetti *et al.*, 'Integrin 51 is necessary for regulation of radial migration of cortical neurons during mouse brain development,' *European Journal of Neuroscience*, vol. 31, pp. 399–409, 3 Feb. 2010, ISSN: 0953816X. DOI: 10.1111/j.1460-9568.2009.07072.x. [Online]. Available: /pmc/articles/PMC3460545/%20/pmc/articles/PMC3460545/?report=abstract%20https://www.ncbi.nlm.nih.gov/pmc/articles/PMC3460545/.

[15] O. Marín *et al.*, *Guiding neuronal cell migrations*. Feb. 2010. DOI: 10.1101/cshperspect.a001834. [Online]. Available: http://cshperspectives.cshlp.org/.

[16] J. Grosche *et al.*, 'Microdomains for neuron-glia interaction: Parallel fiber signaling to bergmann glial cells,' *Nature Neuroscience*, vol. 2, pp. 139–143, 2 Feb. 1999, ISSN: 10976256. DOI: 10.1038/5692. [Online]. Available: http://neurosci.nature.com.

[17] M. Valiente and O. Marín, *Neuronal migration mechanisms in development and disease*, Feb. 2010. DOI: 10.1016/j.conb.2009.12.003.

[18] N. Li and A. Folch, 'Integration of topographical and biochemical cues by axons during growth on microfabricated 3-d substrates,' *Experimental Cell Research*, vol. 311, pp. 307–316, 2 Dec. 2005, ISSN: 00144827. DOI: 10.1016/j.yexcr.2005.10.007. [Online]. Available: /pmc/articles/PMC3880801/%20/pmc/articles/

PMC3880801/?report=abstract%20https://www.ncbi.nlm.nih.gov/pmc/articles/PMC3880801/.

[19] N. O. Alieva *et al.*, 'Myosin iia and formin dependent mechanosensitivity of filopodia adhesion,' *Nature Communications*, vol. 10, pp. 1–14, 1 Dec. 2019, ISSN: 20411723. DOI: 10.1038/s41467-019-10964-w. [Online]. Available: https://doi.org/10.1038/s41467-019-10964-w.

[20] B. Martynoga, D. Drechsel and F. Guillemot, 'Molecular control of neurogenesis: A view from the mammalian cerebral cortex.,' *Cold Spring Harb Perspect Biol.*, 2012. DOI: 10.1101/cshperspect.a008359.

[21] J. Albuschies and V. Vogel, 'The role of filopodia in the recognition of nanotopographies,' *Scientific Reports*, vol. 3, pp. 1–9, 1 Apr. 2013, ISSN: 20452322. DOI: 10.1038/srep01658. [Online]. Available: www.nature.com/scientificreports.

[22] O. J. Castejon, 'Surface and membrane morphology of bergmann glial cells and their topographic relationships in the cerebellar molecular layer,' *Journal of Submicroscopic Cytology and Pathology*, vol. 22, pp. 123–134, 1 Jan. 1990, ISSN: 00224782. [Online]. Available: https://europepmc.org/article/med/2311096.

[23] M. J. Dalby *et al.*, 'Investigating the limits of filopodial sensing: A brief report using sem to image the interaction between 10 nm high nano-topography and fibroblast filopodia,' *Cell Biology International*, vol. 28, pp. 229–236, 3 2004, ISSN: 10656995. DOI: 10.1016/j.cellbi.2003.12.004. [Online]. Available: https://pubmed.ncbi.nlm.nih.gov/14984750/.

[24] V. Brunetti *et al.*, 'Neurons sense nanoscale roughness with nanometer sensitivity,' *Proceedings of the National Academy of Sciences of the United States of America*, vol. 107, pp. 6264–6269, 14 Apr. 2010, ISSN: 00278424. DOI: 10.1073/pnas.0914456107. [Online]. Available: https://pubmed.ncbi.nlm.nih.gov/20308580/.

[25] O. Sporns, 'Graphtheorymethods:applications in brain networks,' *Dialogues in clinical neuroscience*, 2018.

[26] D. Basset and E. Bullmore, 'What is a small-world network?,' 2006. DOI: 10.1177/1073858406293182.

[27] E. Bullmore and O. Sporns, 'Complex brain networks: Graph theoretical analysis of structural and functional systems,' *Nature Reviews Neuroscience*, 2009. DOI: 10.1038/nrn2575.

[28] A. Fornito and A. Zalesky, *Fundamentals of brain network analysis*. Academic Press, 2016, ch. 2.

[29] Q. K. Telesford *et al.*, 'The ubiquity of small-world networks,' *Brain Connectivity*, vol. 1, pp. 367–375, 5 Dec. 2011, ISSN: 21580022. DOI: 10.1089/brain.2011.0038. [Online]. Available: /pmc/articles/PMC3604768/%20/pmc/articles/PMC3604768/?report=abstract%20https://www.ncbi.nlm.nih.gov/pmc/articles/PMC3604768/.

[30] G. Marinaro *et al.*, 'Networks of neuroblastoma cells on porous silicon substrates reveal a small world topology,' *Integrative Biology (United Kingdom)*, vol. 7, pp. 184–197, 2 Feb. 2015, ISSN: 17579708. DOI: 10.1039/c4ib00216d. [Online]. Available: https://academic.oup.com/ib/article/7/2/184/5191117.

[31] A. L. Barabási, N. Gulbahce and J. Loscalzo, 'Network medicine: A network-based approach to human disease,' *Nature Reviews Genetics*, vol. 12, pp. 56–68, 1 Jan. 2011, ISSN: 14710056. DOI: 10.1038/nrg2918. [Online]. Available: /pmc/articles/PMC3140052/?report=abstract%20https://www.ncbi.nlm.nih.gov/pmc/articles/PMC3140052/.

[32] E. J. Sanz-Arigita *et al.*, 'Loss of 'small-world' networks in alzheimer's disease: Graph analysis of fmri resting-state functional connectivity,' *PLoS ONE*, vol. 5, e13788, 11 2010, ISSN: 19326203. DOI: 10.1371/journal.pone.0013788. [Online]. Available: www.plosone.org.

[33] C. Stam *et al.*, 'Graph theoretical analysis of magnetoencephalographic functional connectivity in alzheimer's disease,' *Brain*, 2009. DOI: https://doi.org/10.1093/brain/awn262.

[34] Y. He, Z. Chen and A. Evans, 'Cortical hubs revealed by intrinsic functional connectivity: Mapping, assessment of stability, and relation to alzheimer's disease,' *Journal of Neuroscience*, 2009. DOI: https://doi.org/10.1523/JNEUROSCI.5062-08.2009.

[35] Y. He, Z. Chen and A. Evans, 'Structural insights into aberrant topological patterns of large-scale cortical networks in alzheimer's disease,' *Journal of Neuroscience*, 2008. DOI: https://doi.org/10.1523/JNEUROSCI.0141-08.2008.

[36] A. Fornito, A. Zalesky and M. Breakspear, *The connectomics of brain disorders*, Feb. 2015. DOI: 10.1038/nrn3901. [Online]. Available: www.nature.com/reviews/neuro.

[37] D. Bassett and E. Bullmore, 'Small-world brain networks revisited,' *Neuroscientist*, 2016. DOI: 10.1177/1073858416667720.

[38] V. D. Valderhaug *et al.*, 'Formation of neural networks with structural and functional features consistent with small-world network topology on surface-grafted polymer particles,' *Royal Society Open Science*, vol. 6, 10 2019, ISSN: 20545703. DOI: 10.1098/rsos.191086. [Online]. Available: /pmc/articles/PMC6837210/%20/pmc/articles/PMC6837210/?report=abstract%20https://www.ncbi.nlm.nih.gov/pmc/articles/PMC6837210/.

[39] V. Onesto *et al.*, 'Nano-topography enhances communication in neural cells networks,' *Scientific Reports*, vol. 7, pp. 1–13, 1 Dec. 2017, ISSN: 20452322. DOI: 10.1038/s41598-017-09741-w. [Online]. Available: www.nature.com/scientificreports/.

[40] D. Karra and R. Dahm, *Transfection techniques for neuronal cells*, May 2010. DOI: 10.1523/JNEUROSCI.0183-10.2010. [Online]. Available: http://www.jneurosci.org/misc/.

[41] A. T. Nguyen, S. R. Sathe and E. K. Yim, *From nano to micro: Topographical scale and its impact on cell adhesion, morphology and contact guidance*, Apr. 2016. DOI: 10.1088/0953-8984/28/18/183001. [Online]. Available: https://pubmed.ncbi.nlm.nih.gov/27066850/.

[42] M. S. Lord, M. Foss and F. Besenbacher, *Influence of nanoscale surface topography on protein adsorption and cellular response*, Feb. 2010. DOI: 10.1016/j.nantod.2010.01.001.

[43] M. K. Leach *et al.*, 'Stages of neuronal morphological development in vitro-an automated assay,' *Journal of Neuroscience Methods*, vol. 199, pp. 192–198, 2 Aug. 2011, ISSN: 01650270. DOI: 10.1016/j.jneumeth.2011.04.033. [Online]. Available: https://pubmed.ncbi.nlm.nih.gov/21571005/.

[44] S. Huh *et al.*, 'Apoptosis detection for adherent cell populations in time-lapse phase-contrast microscopy images,' vol. 7510 LNCS, Springer Verlag, 2012, pp. 331–339, ISBN: 9783642334146. DOI: 10.1007/978-3-642-33415-3_41. [Online]. Available: https://link.springer.com/chapter/10.1007/978-3-642-33415-3_41.

[45] J. Gordon, S. Amini and M. K. White, *General overview of neuronal cell culture*, 2013. DOI: 10.1007/978-1-62703-640-5_1. [Online]. Available: /pmc/articles/PMC4052554/%20https://www.ncbi.nlm.nih.gov/pmc/articles/PMC4052554/.

[46] C. G. Wakade *et al.*, 'Axonal fasciculation and the role of polysialic acid-neural cell adhesion molecule in rat cortical neurons,' *Journal of Neuroscience Research*, vol. 91, pp. 1408–1418, 11 Nov. 2013, ISSN: 03604012. DOI: 10.1002/jnr.23268. [Online]. Available: https://pubmed.ncbi.nlm.nih.gov/23963795/.

[47] L. M. Yu, N. D. Leipzig and M. S. Shoichet, *Promoting neuron adhesion and growth*, May 2008. DOI: 10.1016/S1369-7021(08)70088-9.

[48] S. W. Moore and M. P. Sheetz, 'Biophysics of substrate interaction: Influence on neural motility, differentiation, and repair,' *Developmental Neurobiology*, vol. 71, 11 Nov. 2011, ISSN: 19328451. DOI: 10.1002/dneu.20947.

[49] S. Okujeni, S. Kandler and U. Egert, 'Mesoscale architecture shapes initiation and richness of spontaneous network activity,' *Journal of Neuroscience*, vol. 37, pp. 3972–3987, 14 Apr. 2017, ISSN: 15292401. DOI: 10.1523/JNEUROSCI.2552-16.2017. [Online]. Available: /pmc/articles/PMC6596716/%20/pmc/articles/PMC6596716/?report=abstract%20https://www.ncbi.nlm.nih.gov/pmc/articles/PMC6596716/.

[50] S. Okujeni and U. Egert, 'Self-organization of modular network architecture by activity-dependent neuronal migration and outgrowth,' *eLife*, vol. 8, Sep. 2019, ISSN: 2050084X. DOI: 10.7554/eLife.47996.

[51] C. Simitzi *et al.*, 'Microconical silicon structures influence ngf-induced pc12 cell morphology,' *Journal of Tissue Engineering and Regenerative Medicine*, vol. 9, pp. 424–434, 4 Apr. 2015, ISSN: 19327005. DOI: 10.1002/term.1853. [Online]. Available: https://onlinelibrary.wiley.com/doi/10.1002/term.1853.

[52] M. J. Mahoney *et al.*, 'The influence of microchannels on neurite growth and architecture,' *Biomaterials*, vol. 26, 7 Mar. 2005, ISSN: 01429612. DOI: 10.1016/j.biomaterials.2004.03.015.

[53] A. Ferrari *et al.*, 'Nanotopographic control of neuronal polarity,' *Nano Letters*, vol. 11, pp. 505–511, 2 Feb. 2011, ISSN: 15306984. DOI: 10.1021/nl103349s. [Online]. Available: https://pubs.acs.org/sharingguidelines.

[54] G. G. Genchi *et al.*, 'Pc12 neuron-like cell response to electrospun poly(3-hydroxybutyrate) substrates,' *Journal of Tissue Engineering and Regenerative Medicine*, vol. 9, pp. 151–161, 2 Feb. 2015, ISSN: 19327005. DOI: 10.1002/term.1623. [Online]. Available: https://onlinelibrary.wiley.com/doi/full/10.1002/term.1623%20https://onlinelibrary.wiley.com/doi/abs/10.1002/term.1623%20https://onlinelibrary.wiley.com/doi/10.1002/term.1623.

[55] M. K. Leach *et al.*, 'The culture of primary motor and sensory neurons in defined media on electrospun poly-l-lactide nanofiber scaffolds,' *Journal of Visualized Experiments*, p. 2389, 48 Feb. 2010, ISSN: 1940087X. DOI: 10.3791/2389. [Online]. Available: www.jove.comURL:https://www.jove.com/video/2389.

[56] E. Schnell *et al.*, 'Guidance of glial cell migration and axonal growth on electrospun nanofibers of poly--caprolactone and a collagen/poly--caprolactone blend,' *Biomaterials*, vol. 28, pp. 3012–3025, 19 Jul. 2007, ISSN: 01429612. DOI: 10.1016/j.biomaterials.2007.03.009.

[57] J. M. Corey *et al.*, 'Aligned electrospun nanofibers specify the direction of dorsal root ganglia neurite growth,' *Journal of Biomedical Materials Research - Part A*, vol. 83, pp. 636–645, 3 Nov. 2007, ISSN: 15493296. DOI: 10.1002/jbm.a.31285. [Online]. Available: www.interscience.wiley.com.

[58] H. S. Koh *et al.*, 'Enhancement of neurite outgrowth using nanostructured scaffolds coupled with laminin,' *Biomaterials*, vol. 29, pp. 3574–3582, 26 Sep. 2008, ISSN: 01429612. DOI: 10.1016/j.biomaterials.2008.05.014.

[59] F. Haq *et al.*, 'Neurite development in pc12 cells cultured on nanopillars and nanopores with sizes comparable with fi lopodia,' *International Journal of Nanomedicine*, vol. 2, pp. 107–115, 1 Mar. 2007, ISSN: 1176-9114. DOI: 10.2147/nano.2007.2.1.107. [Online]. Available: /pmc/articles/PMC2673821/%20/pmc/articles/PMC2673821/?report=abstract%20https://www.ncbi.nlm.nih.gov/pmc/articles/PMC2673821/.

[60] W. Li *et al.*, 'Large-scale topographical screen for investigation of physical neural-guidance cues,' *Scientific Reports*, vol. 5, pp. 1–8, 1 Mar. 2015, ISSN: 20452322. DOI: 10.1038/srep08644. [Online]. Available: www.nature.com/scientificreports.

[61] M. A. Bucaro *et al.*, 'Fine-tuning the degree of stem cell polarization and alignment on ordered arrays of high-aspect-ratio nanopillars,' *ACS Nano*, vol. 6, pp. 6222–6230, 7 Jul. 2012, ISSN: 19360851. DOI: 10.1021/nn301654e. [Online]. Available: www.acsnano.org6222.

[62] L. Micholt *et al.*, 'Substrate topography determines neuronal polarization and growth in vitro,' *PLoS ONE*, vol. 8, p. 66 170, 6 Jun. 2013, ISSN: 19326203. DOI: 10.1371/journal.pone.0066170. [Online]. Available: /pmc/articles/PMC3681759/%20/pmc/articles/PMC3681759/?report=abstract%20https://www.ncbi.nlm.nih.gov/pmc/articles/PMC3681759/.

[63] N. R. Blumenthal *et al.*, 'Stochastic nanoroughness modulates neuron-astrocyte interactions and function via mechanosensing cation channels,' *Proceedings of the National Academy of Sciences of the United States of America*, vol. 111, pp. 16 124–16 129, 45 Nov. 2014, ISSN: 10916490. DOI: 10.1073/pnas.1412740111. [Online]. Available: www.pnas.org/cgi/doi/10.1073/pnas.1412740111.

[64] S. P. Khan, G. G. Auner and G. M. Newaz, 'Influence of nanoscale surface roughness on neural cell attachment on silicon,' *Nanomedicine: Nanotechnology, Biology, and Medicine*, vol. 1, pp. 125–129, 2 Jun. 2005, ISSN: 15499634. DOI: 10.1016/j.nano.2005.03.007.

[65] W. K. Cho *et al.*, 'Pitch-dependent acceleration of neurite outgrowth on nanostructured anodized aluminum oxide substrates,' *Angewandte Chemie - International Edition*, vol. 49, pp. 10 114–10 118, 52 Dec. 2010, ISSN: 14337851. DOI: 10.1002/anie.201003307. [Online]. Available: https://pubmed.ncbi.nlm.nih.gov/20886482/.

[66] G. Piret, M. T. Perez and C. N. Prinz, 'Neurite outgrowth and synaptophysin expression of postnatal cns neurons on gap nanowire arrays in long-term retinal cell culture,' *Biomaterials*, vol. 34, pp. 875–887, 4 Jan. 2013, ISSN: 01429612. DOI: 10.1016/j.biomaterials.2012.10.042.

[67] C. Czeisler *et al.*, *Surface topography during neural stem cell differentiation regulates cell migration and cell morphology*, Dec. 2016. DOI: 10.1002/cne.24118.

[68] J. Seo *et al.*, 'Neuronal migration on silicon microcone arrays with different pitches,' *Advanced Healthcare Materials*, vol. 10, 4 Feb. 2021, ISSN: 21922659. DOI: 10.1002/adhm.202000583. [Online]. Available: https://pubmed.ncbi.nlm.nih.gov/32815647/.

[69] Y. W. Fan *et al.*, 'Culture of neural cells on silicon wafers with nanoscale surface topograph,' *Journal of Neuroscience Methods*, vol. 120, pp. 17–23, 1 Oct. 2002, ISSN: 01650270. DOI: 10.1016/S0165-0270(02)00181-4.

[70] L. A. Cyster *et al.*, 'The effect of surface chemistry and nanotopography of titanium nitride (tin) films on primary hippocampal neurones,' *Biomaterials*, vol. 25, pp. 97–107, 1 2004, ISSN: 01429612. DOI: 10.1016/S0142-9612(03)00480-0. [Online]. Available: https://pubmed.ncbi.nlm.nih.gov/14580913/.

[71] S. Keller *et al.*, 'Processing of thin su-8 films,' *Journal of Micromechanics and Microengineering*, vol. 18, p. 125 020, 12 Dec. 2008, ISSN: 09601317. DOI: 10.1088/0960-1317/18/12/125020. [Online]. Available: https://iopscience.iop.org/article/10.1088/0960-1317/18/12/125020%20https://iopscience.iop.org/article/10.1088/0960-1317/18/12/125020/meta.

[72] K. V. Nemani *et al.*, 'In vitro and in vivo evaluation of su-8 biocompatibility,' *Materials Science and Engineering C*, vol. 33, pp. 4453–4459, 7 Oct. 2013, ISSN: 09284931. DOI: 10.1016/j.msec.2013.07.001.

[73] L. Isdal, 'Developing 2.5d nanotopographical neural network recording platform to mimic the physiological conditions of the *in vivo* brain,' *NTNU Master's Thesis*, Jun. 2021.

[74] N. Oruganti, M. Goedert and S. J. J. Lee, 'Process variability in surface roughening of su-8 by oxygen plasma,' *Microsystem Technologies*, vol. 19, pp. 971–978, 7 Jul. 2013, ISSN: 09467076. DOI: 10.1007/s00542-012-1680-0. [Online]. Available: https://link.springer.com/article/10.1007/s00542-012-1680-0.

[75] S. W. Youn *et al.*, 'Microstructuring of su-8 photoresist by uv-assisted thermal imprinting with non-transparent mold,' *Microelectronic Engineering*, vol. 85, pp. 1924–1931, 9 Sep. 2008, ISSN: 01679317. DOI: 10.1016/j.mee.2008.06.016.

[76] . [Online]. Available: https://pubs.rsc.org/-/content/articlepdf/2016/lc/c5lc01445j?page=searc.

[77] F. Zernike, 'Phase contrast, a new method for the microscopic observation of transparent objects,' *Physica*, vol. 9, 7 Jul. 1942, ISSN: 00318914. DOI: 10.1016/S0031-8914(42)80035-X.

[78] J. M. Mullins, 'Fluorochromes: Properties and characteristics.,' *Methods in molecular biology (Clifton, N.J.)*, vol. 588, pp. 123–134, 2010, ISSN: 19406029. DOI: 10.1007/978-1-59745-324-0_15.

[79] K. Spring and M. Davidson. (2008). 'Ntroduction to fluorescence microscopy.'

[80] E. Pretorius, 'Influence of acceleration voltage on scanning electron microscopy of human blood platelets,' *Microscopy Research and Technique*, vol. 73, pp. 225–228, 3 Mar. 2010, ISSN: 1059910X. DOI: 10.1002/jemt.20778. [Online]. Available: https://pubmed.ncbi.nlm.nih.gov/20087904/.

[81] N. Erdman, D. C. Bell and R. Reichelt, *Scanning electron microscopy*, 2019. DOI: 10.1007/978-3-030-00069-1_5. [Online]. Available: https://doi.org/10.1007/978-3-030-00069-1_5.

[82] P. B. Bell and B. Safiejko-Mroczka, 'Preparing whole mounts of biological specimens for imaging macromolecular structures by light and electron microscopy,' 1997, pp. 225–239. DOI: 10.1002/(SICI)1098-1098(1997)8:3.

[83] A. M. Kashi *et al.*, 'How to prepare biological samples and live tissues for scanning electron microscopy (sem),' *undefined*, 2014.

[84] *The use of hmds (hexamethyldisilazane) to replace critical point drying (cpd) in the preparation of tardigrade for sem (scanning electron microscope) imaging on jstor*. [Online]. Available: https://www.jstor.org/stable/40588242?seq=1#metadata_info_tab_contents.

[85] J. Gumpert, 'G. a. meek, practical electron microscopy for biologists (2 nd edition). xix, 528 s., 182 abb., 2 tab. london-new york-sydney-toronto 1976: John wiley and sons. £ 13.50,' *Zeitschrift für allgemeine Mikrobiologie*, vol. 17, pp. 330–330, 4 Jan. 1977. DOI: 10.1002/jobm.19770170422. [Online]. Available: https://onlinelibrary.wiley.com/doi/full/10.1002/jobm.19770170422%20https://onlinelibrary.wiley.com/doi/abs/10.1002/jobm.19770170422%20https://onlinelibrary.wiley.com/doi/10.1002/jobm.19770170422.

[86] S. Nikara, E. Ahmadi and A. A. Nia, 'Effects of different preparation techniques on the microstructural features of biological materials for scanning electron microscopy,' *Journal of Agriculture and Food Research*, vol. 2, p. 100 036, Dec. 2020, ISSN: 26661543. DOI: 10.1016/j.jafr.2020.100036.

[87] E. R. Fischer *et al.*, 'Scanning electron microscopy,' *Current Protocols in Microbiology*, vol. CHAPTER, Unit2B.2, SUPPL.25 May 2012, ISSN: 19348525. DOI: 10.1002/9780471729259.mc02b02s25. [Online]. Available: /pmc/articles/PMC3352184/%20https://www.ncbi.nlm.nih.gov/pmc/articles/PMC3352184/.

[88] J. I. Goldstein *et al.*, *Coating and conductivity techniques for sem and microanalysis*, 1992. DOI: 10.1007/978-1-4613-0491-3_13. [Online]. Available: https://link.springer.com/chapter/10.1007/978-1-4613-0491-3_13.

[89] R. M. Lu *et al.*, *Development of therapeutic antibodies for the treatment of diseases*, Jan. 2020. DOI: 10.1186/s12929-019-0592-z. [Online]. Available: https://doi.org/10.1186/s12929-019-0592-z.

[90] R. W. Burry, *Antibodies*, 2010. DOI: 10.1007/978-1-4419-1304-3_2. [Online]. Available: http://link.springer.com/10.1007/978-1-4419-1304-3_2.

[91] R. W. Burry, *Antibodies*, 2010. DOI: 10.1007/978-1-4419-1304-3_2. [Online]. Available: http://link.springer.com/10.1007/978-1-4419-1304-3_2.

[92] M. E. J. Obien *et al.*, *Revealing neuronal function through microelectrode array recordings*, Jan. 2015. DOI: 10.3389/fnins.2014.00423. [Online]. Available: http://www.multichannelsystems.com.

[93] G. H. Kim *et al.*, *Recent progress on microelectrodes in neural interfaces*, Oct. 2018. DOI: 10.3390/ma11101995. [Online]. Available: https://pubmed.ncbi.nlm.nih.gov/30332782/.

[94] B. Ghane-Motlagh and M. Sawan, 'Design and implementation challenges of microelectrode arrays: A review,' *Materials Sciences and Applications*, vol. 04, pp. 483–495, 08 2013, ISSN: 2153-117X. DOI: 10.4236/msa.2013.48059.

[95] S. M. Potter and T. B. DeMarse, 'A new approach to neural cell culture for long-term studies,' *Journal of Neuroscience Methods*, vol. 110, pp. 17–24, 1-2 Sep. 2001, ISSN: 01650270. DOI: 10.1016/S0165-0270(01)00412-5. [Online]. Available: https://pubmed.ncbi.nlm.nih.gov/11564520/.

[96] Z. Israel *et al.*, *Microelectrode Recording in Movement Disorder Surgery*. Georg Thieme Verlag, Jun. 2014. DOI: 10.1055/b-002-56126.

[97] J. Zhang, J. Xia and H. Xiong, *Techniques for extracellular recordings*, 2014. DOI: 10.1007/978-1-4614-8794-4_23. [Online]. Available: https://link.springer.com/protocol/10.1007/978-1-4614-8794-4_23.

[98] F. Zeldenrust, W. J. Wadman and B. Englitz, *Neural coding with bursts—current state and future perspectives*, Jul. 2018. DOI: 10.3389/fncom.2018.00048. [Online]. Available: www.frontiersin.org.

[99] E. S. Kuebler *et al.*, 'Burst predicting neurons survive an in vitro glutamate injury model of cerebral ischemia,' *Scientific Reports*, vol. 5, p. 17718, 1 Dec. 2015, ISSN: 20452322. DOI: 10.1038/srep17718. [Online]. Available: www.nature.com/scientificreports.

[100] B. M. Waxman, 'Routing of multipoint connections,' *IEEE Journal on Selected Areas in Communications*, vol. 6, pp. 1617–1622, 9 1988, ISSN: 07338716. DOI: 10.1109/49.12889.

[101] V. Onesto *et al.*, 'Small-world networks of neuroblastoma cells cultured in three-dimensional polymeric scaffolds featuring multi-scale roughness,' *Neural Regeneration Research*, vol. 15, pp. 759–768, 4 Apr. 2020, ISSN: 18767958. DOI: 10.4103/1673-5374.266923. [Online]. Available: http://www.nrronline.org/article.asp?issn=1673-5374;year=2020;volume=15;issue=4;spage=759;epage=768;aulast=Onesto%20http://www.nrronline.org/article.asp?issn=1673-5374;year=2020;volume=15;issue=4;spage=759;epage=768;aulast=Onesto;type=0.

[102] M. Naldi, 'Connectivity of waxman topology models,' *Computer Communications*, vol. 29, pp. 24–31, 1 Dec. 2005, ISSN: 01403664. DOI: 10.1016/j.comcom.2005.01.017.

[103] N. Winter-Hjelm, 'Development of a tailored microfluidic platform with improved electrical signal detection for in vitro studies of neural networks and neural network pathology,' *M.S. thesis, Norwegian University of Science and Technology*, 2020.

[104] B. Preim and C. P. Botha, *Visual Computing for Medicine: Theory, Algorithms, and Applications: Second Edition*. Elsevier Inc., 2014, pp. 1–812, ISBN: 9780124158733. DOI: 10.1016/C2011-0-05785-X.

[105] A. Hagberg, D. Schult and P. J. Swart. (2008). 'Exploring network structure, dynamics, and function using networkx.'

[106] S. K. Tang and W. F. Marshall, *Self-repairing cells: How single cells heal membrane ruptures and restore lost structures*, Jun. 2017. DOI: 10.1126/science.aam6496. [Online]. Available: /pmc/articles/PMC5664224/%20/pmc/articles/PMC5664224/?report=abstract%20https://www.ncbi.nlm.nih.gov/pmc/articles/PMC5664224/.

[107] K. Göbbels *et al.*, 'Neuronal cell growth on iridium oxide,' *Biomaterials*, vol. 31, pp. 1055–1067, 6 Feb. 2010, ISSN: 01429612. DOI: 10.1016/j.biomaterials.2009.10.029.

[108] K. Webb, V. Hlady and P. A. Tresco, 'Relative importance of surface wettability and charged functional groups on nih 3t3 fibroblast attachment, spreading, and cytoskeletal organization,' *Journal of Biomedical Materials Research*, vol. 41, pp. 422–430, 3 Sep. 1998, ISSN: 00219304. DOI: 10.1002/(SICI)1097-4636(19980905)41:3<422::AID-JBM12>3.0.CO;2-K. [Online]. Available: /pmc/articles/PMC2632339/%20/pmc/articles/PMC2632339/?report=abstract%20https://www.ncbi.nlm.nih.gov/pmc/articles/PMC2632339/.

[109] S. Bosi *et al.*, 'From 2d to 3d: Novel nanostructured scaffolds to investigate signalling in reconstructed neuronal networks,' *Scientific Reports*, vol. 5, pp. 1–11, 1 Apr. 2015, ISSN: 20452322. DOI: 10.1038/srep09562. [Online]. Available: www.nature.com/scientificreports.

[110] M. J. Dalby, N. Gadegaard and R. O. Oreffo, 'Harnessing nanotopography and integrin-matrix interactions to influence stem cell fate,' *Nature Materials*, vol. 13, pp. 558–569, 6 May 2014, ISSN: 14764660. DOI: 10.1038/nmat3980. [Online]. Available: www.nature.com/naturematerials.

[111] K. J. Lampe, A. L. Antaris and S. C. Heilshorn, 'Design of three-dimensional engineered protein hydrogels for tailored control of neurite growth,' *Acta Biomaterialia*, vol. 9, pp. 5590–5599, 3 Mar. 2013, ISSN: 17427061. DOI: 10.1016/j.actbio.2012.10.033.

[112] E. Spedden *et al.*, 'Effects of surface asymmetry on neuronal growth,' *PLoS ONE*, vol. 9, p. 106 709, 9 Sep. 2014, ISSN: 19326203. DOI: 10.1371/journal.pone.0106709. [Online]. Available: /pmc/articles/PMC4153665/%20/pmc/articles/PMC4153665/?report=abstract%20https://www.ncbi.nlm.nih.gov/pmc/articles/PMC4153665/.

[113] M. K. Hancock *et al.*, 'A facile method for simultaneously measuring neuronal cell viability and neurite outgrowth,' *Current Chemical Genomics and Translational Medicine*, vol. 9, pp. 6–16, 1 Mar. 2015, ISSN: 22139885. DOI: 10.2174/2213988501509010006. [On-

line]. Available: /pmc/articles/PMC4382562/%20/pmc/articles/PMC4382562/?report=abstract%20https://www.ncbi.nlm.nih.gov/pmc/articles/PMC4382562/.

[114] B. L. Robinette *et al.*, 'In vitro assessment of developmental neurotoxicity: Use of microelectrode arrays to measure functional changes in neuronal network ontogeny,' *Frontiers in Neuroengineering*, vol. 4, pp. 1–9, JANUARY Jan. 2011, ISSN: 16626443. DOI: 10.3389/fneng.2011.00001. [Online]. Available: www.frontiersin.org.

[115] E. Cotterill *et al.*, 'Characterization of early cortical neural network development in multiwell microelectrode array plates,' *Journal of Biomolecular Screening*, vol. 21, pp. 510–519, 5 Jun. 2016, ISSN: 1552454X. DOI: 10.1177/1087057116640520. [Online]. Available: https://pubmed.ncbi.nlm.nih.gov/27028607/.

[116] M. Chiappalone *et al.*, 'Dissociated cortical networks show spontaneously correlated activity patterns during in vitro development,' *Brain Research*, vol. 1093, pp. 41–53, 1 Jun. 2006, ISSN: 00068993. DOI: 10.1016/j.brainres.2006.03.049.

[117] L. M. Bettencourt *et al.*, 'Functional structure of cortical neuronal networks grown in vitro,' *Physical Review E - Statistical, Nonlinear, and Soft Matter Physics*, vol. 75, p. 021 915, 2 Feb. 2007, ISSN: 15393755. DOI: 10.1103/PhysRevE.75.021915. [Online]. Available: https://journals.aps.org/pre/abstract/10.1103/PhysRevE.75.021915.

[118] C. O. Colpan, Y. Nalbant and M. Ercelik, *Fundamentals of fuel cell technologies*, Feb. 2018. DOI: 10.1016/B978-0-12-809597-3.00446-6.

[119] B. Bilenberg *et al.*, 'High resolution 100 kv electron beam lithography in su-8,' *Microelectronic Engineering*, vol. 83, pp. 1609–1612, 4-9 SPEC. ISS. Apr. 2006, ISSN: 01679317. DOI: 10.1016/j.mee.2006.01.142.

Appendix A

Appendix

A.1 Additional Images used in Analysis

This section includes additional images references to in the results section. They serve to underscore significance of the observations made in this thesis.

In Figure A.1, two additional images of each surface, S_a from 0-150 nm, is presented, and serves as complimentary data to the data presented in Section **??**.

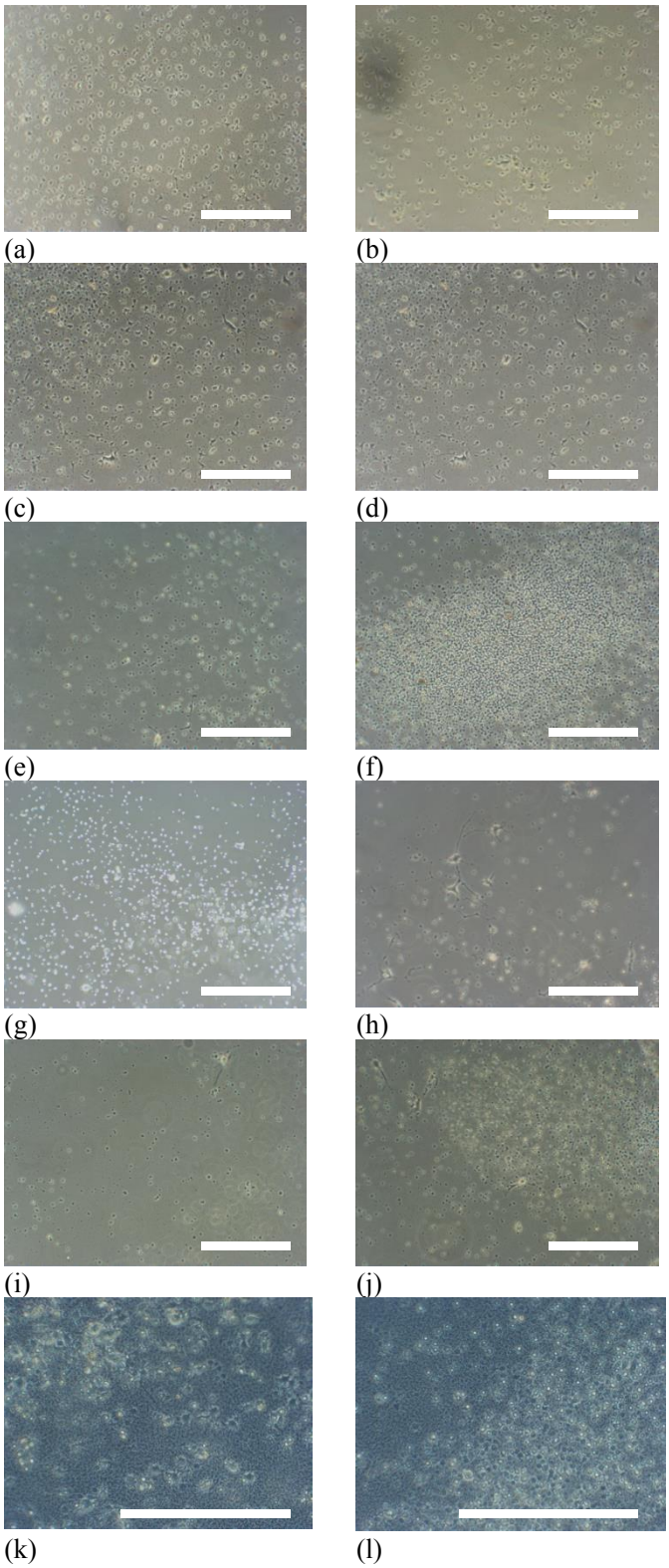

Figure A.1: Representative images from central region of all surfaces. The ROIs were selected at random, to avoid bias in analysis. Images acquired by phase contrast microscopy, after 4 DIV. (a)-(b) is 0 nm (glass control), (c)-(d) is 0 nm (SU-8 planar control), (e)-(f) $S_a = 25$ nm, (g)-(h) $S_a = 50$ nm, (i)-(j) $S_a = 75$ nm and (k)-(l) $S_a = 150$ nm. All images have a scale bar of 150 μm.

In Figure A.4, 4 images of each surface is included, where the first row is images of the glass control, the second chip is of SU-8 planar control, third row is of surface with S_a 1.3 nm, fourth row is of surface with S_a of 6.8 nm and last row is of surface with S_a of 10.3 nm. These images serve to further validate the observations presented in Section 4.2.2.

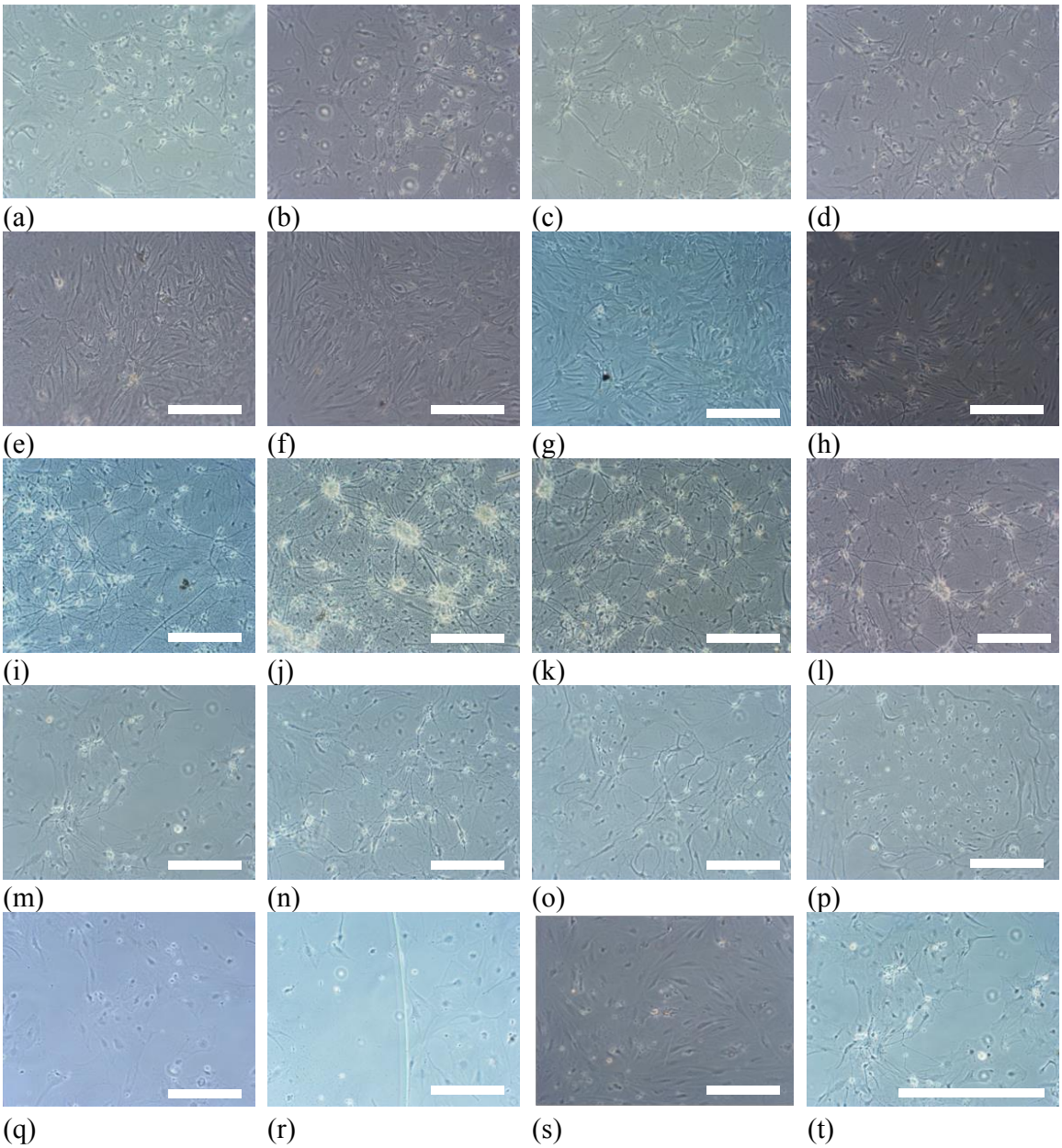

Figure A.2: Representative images from central region of all surfaces. The ROIs were selected at random, to avoid bias in analysis. Images acquired by phase contrast microscopy, generally after 14 DIV, but for the last row of images were taken after 7 and 9 DIV, as the surface malfunctioned and the cells were terminated after this. All images have a scale bar of 150 μm.

A.1.1 SEM Morphology Analysis

Qualitative Analysis

To underscore the qualitative analysis conducted in Section 4.3, additional images are added in Figure A.3. Figure A.3 (a)-(b) are taken of neurons on planar surfaces, while (c)-(d) is from neurons on nanotopography surfaces with $S_a = 4.7$ nm.

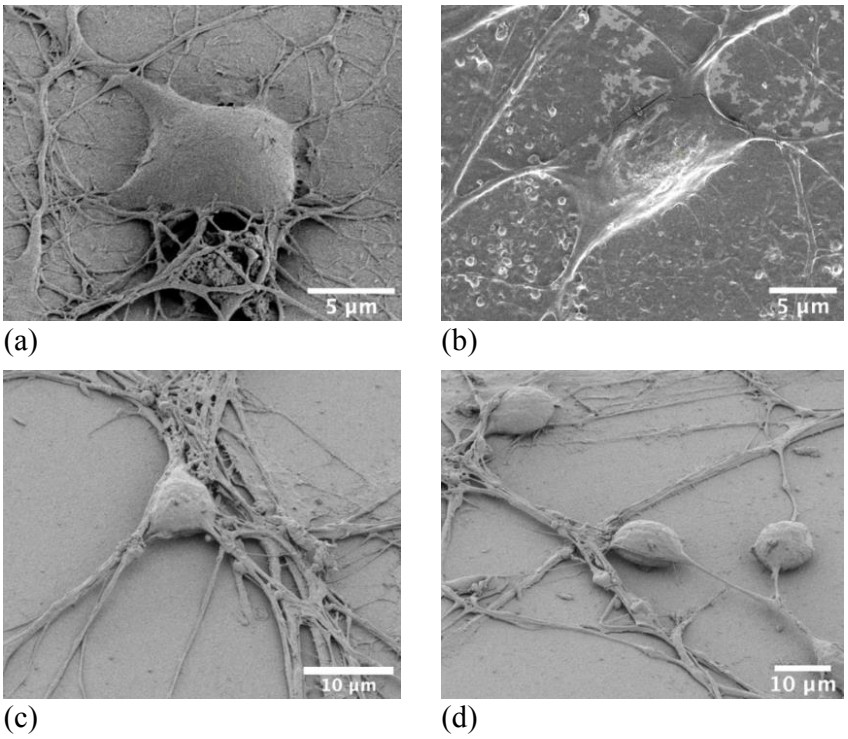

Figure A.3: Images acquired by SEM, secondary electrons were detected using optimised settings in immersion mode (low voltage (1000 V) and low current (3.1 pA). (a) shows neuron growing on glass substrate, and exhibits a flattened structure with a large contact area with the substrate. (b) shows neuron grown on a planar SU-8 surface, which shows similar characteristics as the cell in image (a). (c)-(d) shows neurons on nanotopography surface with $S_a = 4.7$ nm, which clearly exhibit a more rounded soma, with a smaller area in contact with the substrate. Scale bars are indicated on the images.

Quantitative Analysis

Overview images acquired with SEM. Cells analysed in Section 4.9 were taken from these images.

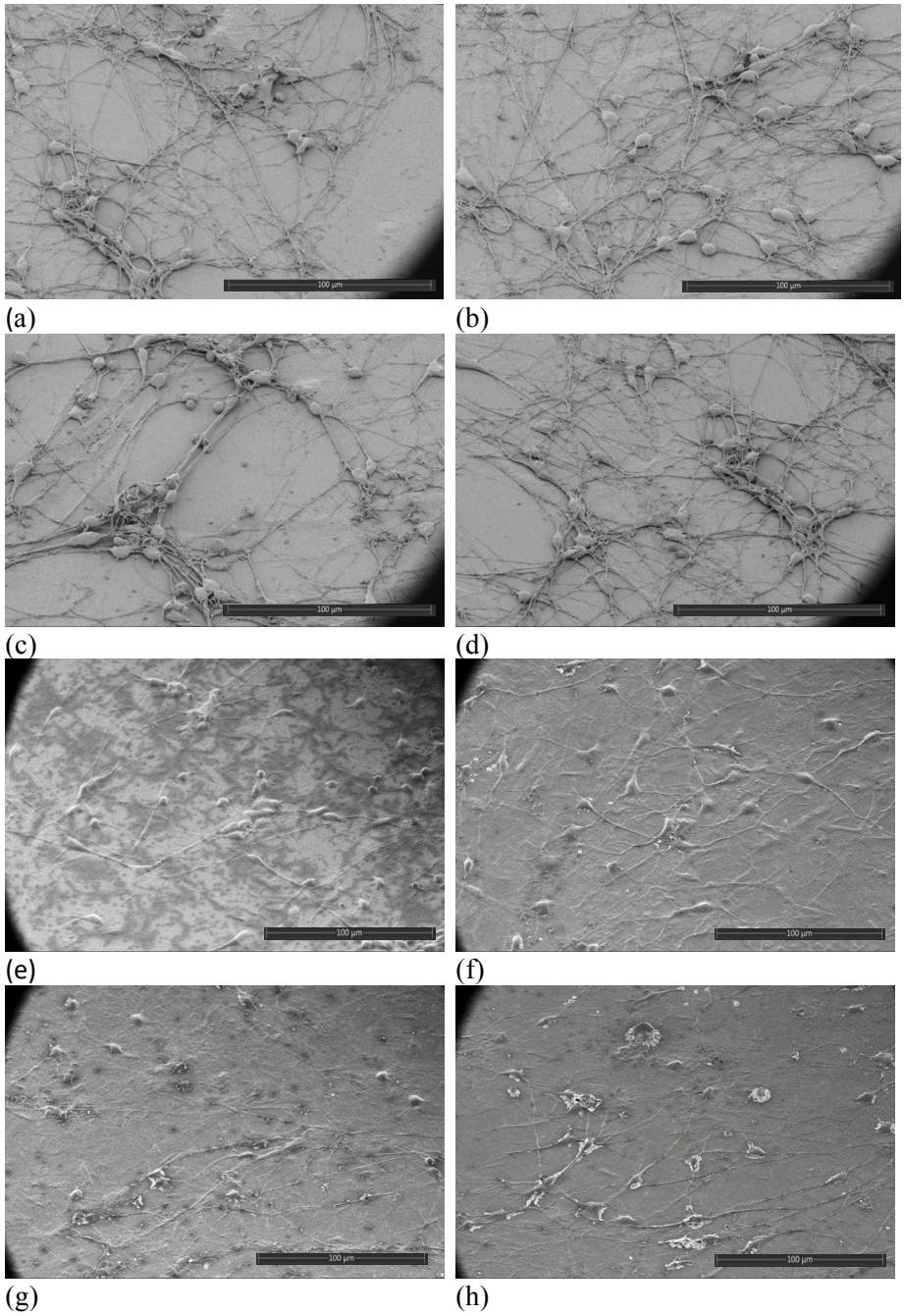

Figure A.4: Overview SEM images used in morphology analysis. The ROIs were selected at random, to avoid bias in analysis. (a) to (d) are of cells on the surface with $S_a = 4.7$ nm, and (e) to (h) are cells cultured on planar SU-8 surfaces. Scale bars are indicated on the figures.

A.1.2 Developing Computational Neural Network Analysis Script

It was set out to develop an automated computational tool to analyse the topological characteristics of the cultured neural networks. This program was based around the Waxman model, the theory behind this model was presented in Section 2.4.7. The program used NeuN images acquired from ICC as input, and outputted a quantification of the network topological features. The pipeline of the program included three main steps: Processing of raw ICC images and extraction of neuron coordinates, simulation of network using the Waxman algorithm, characterisation of network predeveloped algorithms from Networkx [105]. Code for FIJI script and simulation can be found at Github [1].

In order to develop a biologically relevant model, it was necessary to select appropriate values for the two model parameters, α and β. α was firstly set to be 1, to ensure that the maximum probability of connection between two nodes was 1. The value of β was then selected so that the resulting network would have a density of connections that reflected the networks visualized by beta-III-tubulin. This was done by investigating the effect of β on the density of the network. Therefore, simulation of a selection of images from surfaces of $S_a = 0$ nm, 1.3 nm and 6.8 nm, with an array of β-values in the interval 0.02 to 0.1 was done. An overview of the constructed networks is shown in Figure A.5. For large and small vaues of β, the networks were qualitatively deemed as improbable and not relevant. From a quantitative comparison with neural netoworks visualized by beta-III-tubulin staining, β was set to 0.065. For this value, the average degree (number of edges per node) was 18, as can be seen from Figure A.6.

[1] https://github.com/edehvide/Waxman-model

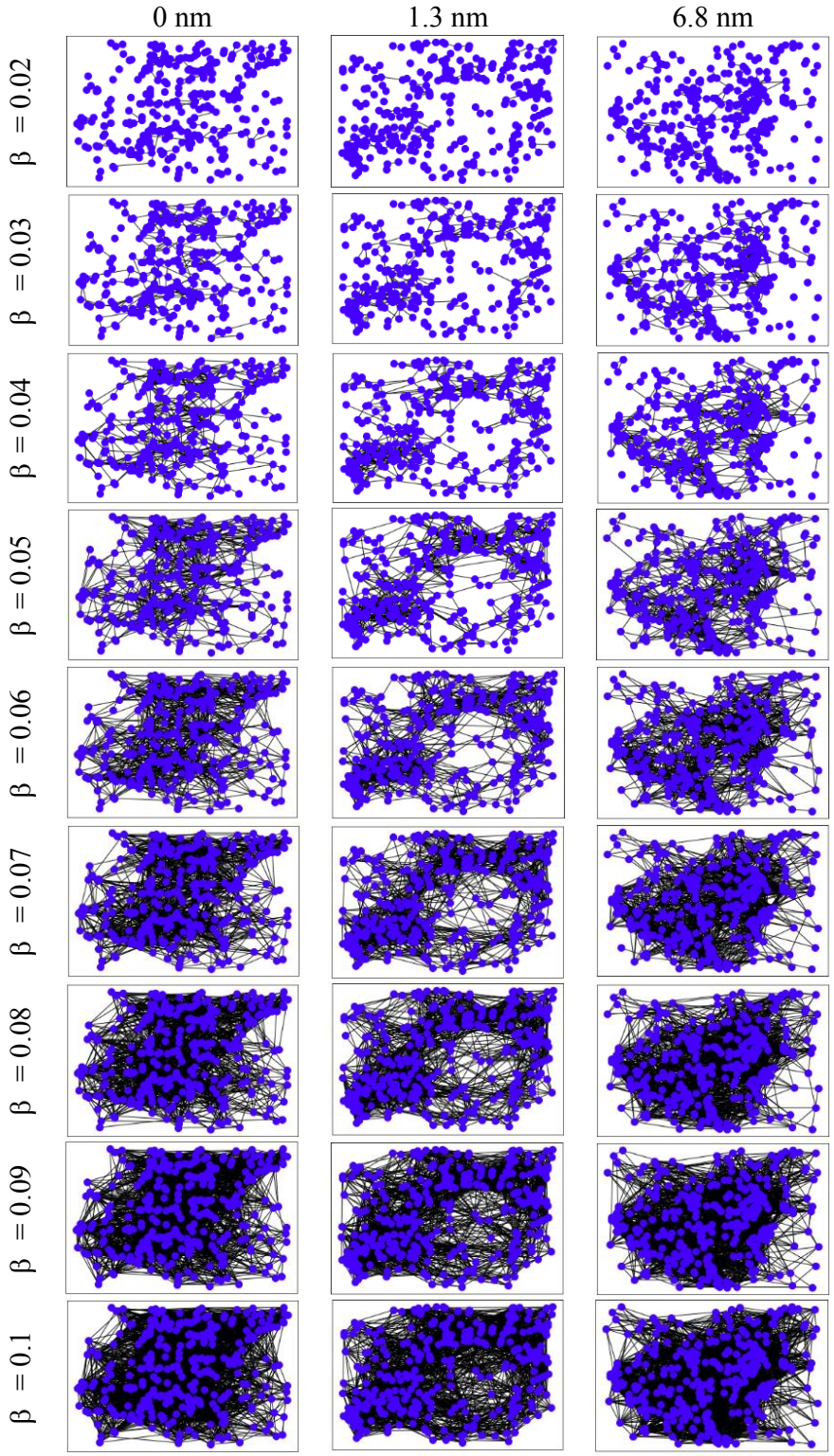

Figure A.5: Simulations of networks to determine optimal beta parameter value

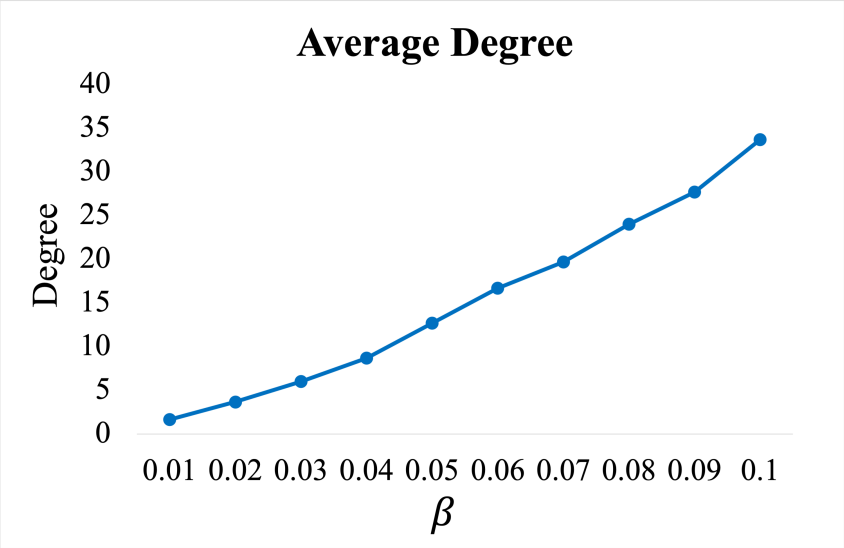

Figure A.6: Average degree graph

A.2 Protocols for Cell Handling

A.2.1 Biosafety in Cell Laboratory

The majority of work described in this project was carried out in a biosafety hood. Several safety measures were imperative to follow to avoid contamination and futile experimental results. All surfaces were sterilized with ethanol both before and after use, and a sufficient air flow in the fume hood was attained before start. All solution containers and equipment were thoroughly sterilized with ethanol before they were brought into the fume hood. During activity, all tubes and vials were open for as short a time as possible and lids were closed when containers were not being used. Furthermore, all work was done at least 10 centimeters within the fume hood sash, and working with hands directly above the microfluidic devices was avoided. All waste was placed in a separate container, which was sterilized and thrown away after use. If any spills occurred, it was cleaned up and sterilized immediately, taking especial care of if spills occurred in the petri-dishes that contain the chips. Furthermore, when the petri-dishes containing the chips were taken out of the fume hood, they had at all times the lid on and covered with airtight parafilm around the edges.

Coating of Microfluidic Chips

1. Sterilize microfluidic chip by placing it under UV light in a fume hood for at least one hour, preferentially over night

2. Place a smaller petri dish with DI water filled 50% up in the bigger petri dish

3. Remove DI water from the wells and replace with Poly-L-ornithine (PLO) solution (make sure to have one chamber more filled than the other, so that hydrostatic pressure flushes out any remaining liquid from the channels) and leave for 30 minutes

4. Remove solution from the wells and replace with new PLO solution and incubate at 37°C for 60 minutes

5. Remove PLO solution and wash the chip with DI water 3 times with 10 minutes in between each round

6. Remove the water from the chambers and replace with laminin solution consisting of 3mL L15, 75μL sodium bicarbonate and 50μL laminin, or equivalent proportions. Leave for 30 minutes

7. Remove the water from the chambers and replace with laminin solution consisting of Laminin Mouse Protein (Thermofischer Scientific) diluted in Gibco PBS (Thermofischer Scientific) at a concentration of20g per mL, then incubate at 37 °C for 2 hours.

Seeding of Rat Primary Cortical Astrocytes

1. Remove the laminin solution and replace with pre-warmed astrocyte cell media consisting of:
   - 83% D-MEM, high glucose (Thermofischer Scientific)
   - 400μL 15% Gibco Fetal Bovine Serum (FBS) (Thermofischer Scien-tific)
   - 2% Penicillin-Streptomycin (Thermofischer Scientific)

2. Remove the rat primary cortical astrocytes from liquid nitrogen storage, and immediately transfer the cells to a 37 °C water bath to prevent crystal formation. This is crucial, as the storage medium is toxic to the cells.

3. Thaw the vial of cells by gently swirling it in the 37 °C water bath, and remove it immediately when all the ice has melted (approximately 2 minutes)

4. Gently transfer the cells into a pre-rinsed 15-mL centrifuge tube with 10 mL astrocyte cell media (one drop/second). Rinse the vial with 1 mL of astrocyte cell media and transfer to the centrifuge tube to make sure all astrocytes have been transferred and resuspend slowly.

5. Centrifuge the cells at 250g for 5 minutes.

6. Aspirate the supernatant and resuspend cells in 1 mL of astrocyte growth medium

7. Conduct cell count, as shown below

8. Transfer approximately 2 000 cells to each cell chamber of the chip (containing roughly 50L medium in total

9. Incubate at 37°C, 5% CO2, and 90% humidity

10. Allow the astrocytes to attach and start proliferation for 2 days before seeding rat cortical neurons

Cell Count

1. Conduct a cell count by first mixing $10\mu L$ of cell solution with $10\mu L$ of cell count medium (trypan blue) ((Thermofischer Scientific)), and then use a pipette to inject $10\mu L$ of the mixed solution into both sides of the cell count chip, take the average of these two sides

Seeding of Rat Cortical Neurons

1. Prepare the neural cell media consisting of
   - 95% Neurobasal plus Medium (Thermofischer Scientific)
   - 2% B-27 Plus Supplement (50X) (Thermofischer Scientific)
   - 1% Gibco GlutaMAX Supplement (Thermofischer Scientific)
   - 2% Penicillin-Streptomycin (Thermofischer Scientific)

2. Remove the rat cortical neurons from liquid nitrogen storage, and

immediately transfer the cells to a 37 °C water bath to prevent crystal formation. This is crucial, as the storage medium is toxic to the cells.

3. Thaw the vial of cells by gently swirling it in the 37 °C water bath, and remove it immediately when all the ice has melted (approximately 2 minutes)

4. Gently transfer the cells into a pre-rinsed 15 mL centrifuge tube with 500 μL neural cell media (one drop/second). Add Rock Inhibitor to increase the survival rate of the neurons during seeding. Resuspend slowly.

5. Replace the astrocyte media in the cell chambers with neural cell media, and transfer approximately 20 000 rat cortical neurons to each cell chamber of the chip (containing roughly 500 μL medium in total). Rat cortical neurons are difficult to count during seeding. There is supposed to 1M cells in one vial. Thus, 20 000 cells equals approximately 30 μL per well.

6. Change 50% of the neural cell media 5 hours after seeding with fresh media

7. Change 50% of the neural cell media with fresh media the next day

8. From then on, change approximately half the cell media every second day. Be careful not to expose cells to air or damage electrodes with pipette at all times.

Edevard Brekke Hvide

NTNU
Norwegian University of
Science and Technology